UNIVERSITY OF SOUTHAMPTON

RANS-based prediction of noise from isothermal and hot subsonic jets

Victor Rosa

A thesis submitted in partial fulfilment for the
degree of Doctor of Philosophy

in the

Faculty of Engineering and the Environment
Institute of Sound and Vibration Research

January 2018

UNIVERSITY OF SOUTHAMPTON

ABSTRACT

FACULTY OF ENGINEERING AND THE ENVIRONMENT
INSTITUTE OF SOUND AND VIBRATION RESEARCH

Doctor of Philosophy

RANS-BASED PREDICTION OF NOISE FROM ISOTHERMAL AND HOT SUBSONIC JETS

by Victor ROSA

Current civil aircraft are significantly quieter than the civil aircraft of the 20^{th} century. But the overall impact of aircraft noise has not been reduced by the same token because the number of aircraft operations has been steadily increasing. So to compensate for the increase in aircraft operations and reduce the overall impact of aircraft noise, we must design quieter aircraft.

The noise generated by the jet leaving the engine exhaust is the dominant source when the aircraft is taking off, so its reduction will lead to significant reduction of the total aircraft noise. The current engine design employs decades of research on jet noise, so noise technology has reached a mature state. Thus to further reduce jet noise we must assess the impact of once secondary elements or employ disruptive designs. These assessments would have such a large design space that it is not possible to rely on experimental campaigns and scaling laws, hence the need to develop numerical methods to predict jet noise.

This thesis studies methods to predict jet noise that use an acoustic analogy and information from a steady RANS solution of the flow to compute turbulence two-point statistics. RANS-based methods rely on empirical modelling but may provide the optimum balance between computational cost and generality needed by the industry to design the next generation of jet engines.

The goal of the thesis is to reduce the empiricism of RANS-based prediction whilst keeping the low computational cost. The contributions of the thesis are summarised in three aspects: (1) introduce a model for the additional sound source in hot jets, (2) formulate the empirical model of turbulence statistics in frequency domain, and (3) compute the effect of turbulence anisotropy on jet noise directivity.

The contributions of the thesis update an existing prediction method (C. R. S. Ilário et al. Prediction of jet mixing noise with Lighthill's acoustic analogy and geometrical acoustics. *J. Acoust. Soc. Am.*, 141 (2), 2017.) which can be applied by industry, and provide background for further research in academia.

To mom and dad,

for the life they gave me;

to my wife and my son,

for giving my life a purpose.

"*Never hurry and never worry!"*

Charlotte.

Contents

List of Figures

List of Tables

Declaration of Authorship

I, Victor ROSA, declare that this thesis titled, "RANS-based prediction of noise from isothermal and hot subsonic jets" and the work presented in it are my own. I confirm that:

- This work was done wholly or mainly while in candidature for a research degree at this University;
- Where any part of this thesis has previously been submitted for a degree or any other qualification at this University or any other institution, this has been clearly stated;
- Where I have consulted the published work of others, this is always clearly attributed;
- Where I have quoted from the work of others, the source is always given. With the exception of such quotations, this thesis is entirely my own work;
- I have acknowledged all main sources of help;
- Where the thesis is based on work done by myself jointly with others, I have made clear exactly what was done by others and what I have contributed myself;
- Parts of this work have been published as:
  - V. Rosa, R. Self, and C. Ilário. Scaling of noise from heated subsonic jets with properties from RANS CFD. In *23rd ABCM International Congress of Mechanical Engineering, Rio de Janeiro, 2015*;
  - V. Rosa, R. Self, C. Ilário, I. Naqavi, and P. Tucker. Modelling velocity correlations with LES and RANS for prediction of noise from isothermal or hot jets. In *22nd AIAA/CEAS Aeroacoustics Conference*, Lyon, 2016;
  - V. Rosa, R. Self, C. Ilário, I. Naqavi, and P. Tucker. Turbulent correlations in hot jets from LES for RANS-based jet noise prediction. In *23rd International Congress on Sound & Vibration*, Athens, 2016.
  - V. Rosa, A. Proença, R. Self, C. Ilário, Z.-N. Wang, I. Naqavi, and P. Tucker. Sound of transverse momentum fluxes in circular subsonic jets. In *23nd AIAA/CEAS Aeroacoustics Conference*, Denver, 2017.

Signed:

_____

Date:

_____

Acknowledgements

This PhD project was sponsored by the CAPES Foundation of the Brazilian Ministry of Education. Additional support was granted via the Rolls-Royce University Technology Centre of the University of Southampton, where the research has been carried out.

I am grateful for the recommendations given by Prof. P. F. Joseph, Dr. B. J. Tester, and Prof. C. L. Morfey during the examination of the thesis.

I would like to thank Dr. C. Paruchuri and Mr. A. Proença for the discussions about turbulence which lead to some of the ideas developed in this thesis.

Experimental data from the SYMPHONY and SILOET projects, both partly funded by the UK Technology Strategy Board and Rolls-Royce Plc., were used in this thesis. The help from Dr. J. L. T. Lawrence to analyse the data is acknowledged.

Prof. P. G. Tucker, Dr. I. Z. Naqavi, and Dr. Z.-N. Wang are responsible for the large eddy simulations used in this thesis. I am grateful for their willingness to share the data and to help analysing it.

Dr. C. R. S. Ilário introduced me to jet noise and has supported me with technical discussions and motivation during my MSc and PhD degrees. I am thankful for the help throughout these years.

Prof. R. H. Self supervised this thesis. Our discussions about theoretical and practical aspects of jet noise were invaluable for this PhD project. I am grateful for his guidance as a supervisor and for much else I learned from him that goes beyond the scope of a PhD degree.

List of Abbreviations

LES Large eddy simulation

RANS Reynolds-averaged Navier–Stokes

List of Symbols

Roman

a	Sound speed
C_{ii}	Cross-spectral density of u_i
C_{iiii}	Cross-spectral density of u_i^2
c_p	Specific heat at constant pressure
D_J	Nozzle diameter
D^h	Directivity of enthalpy source
D^m	Directivity of momentum source
F^h	Flow factor for enthalpy source and observer at $\theta = 90^\circ$
F^m	Flow factor for momentum source and observer at $\theta = 90^\circ$
h	Enthalpy
k	Mean turbulent kinetic energy, $k = \overline{u_i u_i}/2$
L_{ii}	Integral length scale of u_i
L_{iiii}	Integral length scale of u_i^2
ℓ	Length scale
$\ell_{ii,k}$	Coherence length scale of u_i in the k direction
$\ell_{iiii,k}$	Coherence length scale of u_i^2 in the k direction
M	Acoustic Mach number, $M = U_J/a_0$
M_1	Mean axial Mach number, $M_1 = \overline{U}_1/a_0$
N_{ii}	Non-compactness factor for u_i
N_{iiii}	Non-compactness factor for u_i^2
P	Length of the potential core
p	Pressure
$\overline{p^2}_{\mathrm{RANS}}$	Scaling law for mean square pressure with RANS input
$\overline{p^2}_{\mathrm{NE}}$	Scaling law for mean square pressure with nozzle-exit input
$\overline{p^2}_{\mathrm{NE,FF}}$	Scaling law for mean square pressure with nozzle-exit input and flow factor
q_r^m	Momentum source term in the direction of an observer at $\mathbf{r}$
q_r^h	Enthalpy source term in the direction of an observer at $\mathbf{r}$
R	Gas constant
R_r^m	Space–time correlation of q_r^m

R_r^h	Space–time correlation of q_r^h
R_{ii}	Space–time correlation of u_i
R_{iiii}	Space–time correlation of u_i^2
$\mathbf{r}$, r_i	Coordinate of the farfield observer
S_{ii}	Autospectral density of u_i
S_{iiii}	Autospectral density of u_i^2
S_{pp}	Autospectral density of pressure in the farfield
S_{pp^m}	Contribution from momentum source to S_{pp}
S_{pp^h}	Contribution from enthalpy source to S_{pp}
St	Strouhal number, $St = U_J/D_J$
$\mathbf{s}$, s_i	Space separation vector
T_0	Temperature of hypothetical quiescent and homogeneous medium
T_J	Temperature at nozzle exit
T_R	Temperature ratio, $T_R = T_J/T_0$
U_i	Instantaneous velocity vector
U_J	Velocity at nozzle exit
u_i	Fluctuating velocity vector, $u_i = U_i - \overline{U}_i$
V_{ii}	Volume of the region where u_i is correlated
V_{iiii}	Volume of the region where u_i^2 is correlated
$\mathbf{x}$, x_i	Coordinate of the source

Greek

α	Empirical coefficient
ε	Mean rate of dissipation of turbulent kinetic energy
Γ	Gamma function
γ_{ii}	Coherence function of u_i
γ_{iiii}	Coherence function of u_i^2
κ	Ratio of specific heats
ω	Angular frequency
ϕ_{ii}	Phase of C_{ii}
ϕ_{iiii}	Phase of C_{iiii}
σ_{ii}	Mean square value of u_i, $\sigma_{ii} = \overline{u_i^2}$
σ_{iiii}	Mean square value of u_i^2, $\sigma_{iiii} = \overline{(u_i^2)^2}$
τ_0	Time scale
θ	Polar angle of farfield observer

Subscripts

0	Value for the hypothetical quiescent and homogeneous medium

r	Component of vector or tensor in the direction of the farfield observer

Superscript

m	Related to the momentum source term
h	Related to the enthalpy source term

Chapter 1

Introduction

The noise generated by turbulent air jets became a significant engineering problem in mid 20^{th} century when jet engines started replacing propeller engines as power plants in civil aircraft. The jet engine was superior to propeller engines in many aspects—e.g., higher efficiency at high speed—but it was noisier than the propeller engines. The excessive noise levels of the early jet engines put its widespread application at risk.

Research efforts in academia and industry increased the understanding of jet noise and enabled changes in the engine to reduce jet noise. These design changes make current civil aircraft approximately 20dB quieter than the early jet-powered aircraft [1]. Adding a secondary stream to the jet engine—i.e. changing the design from a turbojet to a turbofan engine—achieved most of the noise reduction. The turbofan engine is quieter because it issues a jet at lower speed than the turbojet engine for the same thrust. The thrust is kept by adding a secondary gas stream with lower velocity but larger area. The lower-speed jet is quieter because it generates less turbulence when it mixes with the ambient air.

Reducing jet noise with the turbofan design increased the relative contribution of other noise sources. The sources of aircraft noise may be split between engine sources and airframe sources. The engine sources are further split into fan, compressor, combustor, turbine, and jet sources. Table 1.1 shows typical levels of acoustic power emitted by these noise sources from a modern wide-bodied aircraft. *Fan* and *jet* are the most significant noise sources at takeoff and approach. The fan is significant at both takeoff and approach; it is secondary at takeoff and dominates at approach condition.

The jet has a minor impact at approach condition, but dominates at takeoff condition, being 2 dB above fan noise. So despite the reductions of jet noise since the first jet engines, jet noise dominates noise emission at takeoff condition.

TABLE 1.1: Breakdown of noise sources of typical wide-bodied civil aircraft (adapted from Astley et al. [2]). Measured power level in dB with arbitrary reference level.

	Takeoff	Approach
Fan	21.2	23.0
Compressor	0.0	14.2
Combustor	9.9	10.8
Turbine	10.8	17.5
Jet	23.0	9.3
Engine total	**24.5**	**24.8**
Airframe	10.8	18.9
Aircraft total	**24.7**	**25.8**

Despite modern civil aircraft being considerably quieter than their predecessors, the overall effect of noise continues to grow because of the increasing number of aircraft operations. Given the current trends of increase in air traffic [3], quieter aircraft are needed to keep the overall impact of aircraft noise at the same level.

International regulating bodies enforce the need of reducing aircraft noise via the certification process for aircraft models entering the market. The certification process considers the aircraft noise that affects people outside the aircraft, not the passengers and crew. So the aircraft is certified for operating conditions when it is closer to the airport: during takeoff and approach. Jet noise is significant at takeoff condition, so it is imperative that it is reduced to comply with future noise certification levels.

Given the advanced status of the technology, the noise reductions needed to comply with these regulations will rely on more subtle design modifications than applied so far. Design changes such as chevron nozzles or non-concentric dual-stream designs could achieve the desired noise reductions. Additionally, it is necessary to assess the

impact on jet noise of other elements of the aircraft such as pylons, the bullet in the core stream, close-coupled wing, and flap. So to reduce jet noise it is necessary to predict the effect of design changes on jet noise, whether the changes are intended to reduce noise or are related to other aspects of aircraft design.

Purely empirical analysis cannot be used to predict the effect these changes because of the large parametric space, and scaling laws based on previous design cannot be used either because of changes in the mechanisms of noise generation. So it is necessary to reduce the empiricism of jet noise prediction used by industry whilst keeping a low computational cost.

1.1 Jet noise prediction

Ongoing research efforts since the first jet engines entered into service increased our understanding of the jet noise problem and enabled technological solutions to mitigate jet noise. Jet noise, once a single dominant noise source in aircraft, is now one among many sources of aircraft noise. Yet, predicting jet noise is still a challenge.

It is possible to predict jet noise from first principles by solving the complete set of equations of fluid motion via direct numerical simulation (e.g. Freund [4]). But this approach is limited to simplified geometries and to low Reynolds numbers due to the high computational cost. Large eddy simulation is a cheaper alternative than direct numerical simulation that computes all necessary features of the flow to predict jet noise.

Large eddy simulations are practical for realistic geometries and Reynolds numbers, but are still too computationally expensive for day-to-day industrial applications. Large eddy simulations are therefore restricted to applications in the research environment—e.g., Wang, Naqavi and Tucker [5] and Tyacke, Wang and Tucker [6]. The challenge that remains is to compute jet noise from first principles and with low computational cost.

Lighthill [7] presented a theory that enables prediction of jet noise based on first

principles. Lighthill's formulation is based on a rearrangement of the equations of fluid motion that enables the prediction of the acoustic farfield of a turbulent flow if information about the turbulence in the jet is available—an approach referred to as an acoustic analogy. Lighthill [7] applied his theory to show that the total sound power emitted by a jet scales with the eighth power of the jet-exit speed.

The scaling of noise power level with the eighth power of jet-velocity predicts the overall noise reduction of turbofan engines when compared to turbojets. The scaling, however, does not predict the effect of complex geometries, e.g., chevron nozzles or dual-stream jets with a hot core. To analyse these effects spectral information about the acoustic farfield is necessary, which in turn requires information about turbulence statistics in the jet plume.

A numerical solution of the Reynolds-averaged Navier–Stokes (RANS) equations may be used to compute information about turbulence in the jet plume. Numerical RANS solutions are implemented in commercial solvers with different turbulence models, but most often used model for jet noise modelling the k–ε model, where k is the turbulent kinetic energy and ε the turbulent dissipation rate. Standard RANS k–ε solvers can deal with arbitrary geometries and operating conditions, giving a description of the mean flow and turbulence in the jet plume. The information about turbulence statistics provided by a RANS k–ε solution, however, is not enough to predict the acoustic farfield spectrum using an acoustic analogy.

The limited information from RANS k–ε must be supplemented with models for turbulence two-point statistics and empirical coefficients to predict jet noise. An early example of this approach was presented by Khavaran, Krejsa and Kim [8] to predict noise from isothermal jets. They used the acoustic analogy by Lighthill [7] to model the sources of sound and supplemented the formulation with the theory by Lilley [9] to account for the propagation of sound through the jet mean flow. The accuracy of the predictions with this so-called RANS-based scheme was remarkable, given the non-linearity of the problem and the limited information from the RANS solution.

Khavaran, Krejsa and Kim [8] modelled the turbulence two-point statistics using an empirical model of space-time velocity correlation (also referred to as velocity

cross-correlation). The space–time correlation model assumes locally homogeneous and isotropic turbulence and a Gaussian function is used to compute the decay with time and with space separation. The scaling parameters of the space–time correlation model—of magnitude, time, and length—are related to the scales provided by the RANS k–ε solution.

In the remaining of this section the review focuses on the research group where this thesis has been developed. Previous work are briefly described to give an overview of the current method presented by Ilário et al. [10]—the starting point of this thesis. A wider review of the literature on jet noise prediction is presented in Chapter 3.

Self [11] presented a model based on Lighthill's acoustic analogy that accounts for frequency-dependent scales of turbulence as measured by Harper-Bourne [12]. Self [11] modelled the turbulence two-point statistics in frequency domain to explicitly account for frequency-dependent scales. This formulation explicitly models the dependence with frequency of the turbulence length scale.

Self and Azarpeyvand [13] also considered frequency-dependent scales, but instead of an explicit frequency-dependence, they redefined the time scale based on an analysis of the turbulence wavenumber spectrum. The new time scale needs less empirical parameters than the time scale used by Self [11]. Self and Azarpeyvand used the model by Khavaran et al. as the basic framework—i.e. using Lighthil's acoustic analogy for sources and Lilley's equation for propagation—, but changing the definition of the time scale.

Ilário et al. [10] used the time scale by Self and Azarpeyvand [13] to model the momentum source of Lighthill's acoustic analogy. The resulting prediction scheme was validated for hot and isothermal jets, but the empirical coefficient must vary with jet temperature.

1.2 Contributions of the thesis

This thesis improves a RANS-based prediction method by presenting the following extensions to the method by Ilário et al. [10]:

1. A new source term, related to enthalpy fluxes, is introduced in the method to predict noise from hot jets.

2. Reformulate the source model to use a frequency-domain model of turbulence statistics and introduce models for the turbulence autospectral density and for the spectrum of coherence length scale.

3. Analyse the effect of turbulence anisotropy on the farfield directivity.

The first contribution has been implemented in the prediction method and validated with farfield predictions. Contributions 2 and 3 are presented as a first step towards a reformulation of the prediction method to use a frequency-domain model of turbulence statistics.

1.3 Thesis outline

The rest of the thesis may be split into four parts. First, Chapters 2 and 3 present the background. Second, Chapters 4 and 5 introduce the models developed in the thesis. Third, Chapters 6, 7, and 8 present numerical results to assess and apply the new models. And fourth, the numerical data used in this thesis are presented in Appendix A and B.

Chapter 2 derives an acoustic analogy using the continuity, momentum, and energy equations. The base, or ambient, flow is assumed at rest and homogeneous, so the formulation is referred to as no-flow acoustic analogy. Chapter 3 reviews RANS-based prediction methods and gives more details about the contributions of the thesis.

New models developed during this work are presented in Chapters 4 and 5. Chapter 4 extends the source model of Ilário et al. [10] by including a model for the enthalpy

source. In Chapter 5 the source model is reformulated using a model for the cross-spectral density instead of the cross-correlation. An existing empirical model for the cross-spectral density is extended by proposing new models for the turbulence autospectral density and for the spectrum of coherence length scale.

The numerical results in Chapter 6 validate the new model for the enthalpy source. A scaling law for the farfield mean square pressure and predictions of farfield autospectral density are compared with farfield measurements. Chapter 7 validates the extensions of the empirical model for the cross-power spectral density. Unsteady data from large eddy simulations of isothermal and hot jets are used to validate the model. In Chapter 8 the unsteady turbulence data is used to compute the effect of source non-compactness and source anisotropy.

Chapter 9 discusses the achievements and limitations of the thesis. Suggestions to overcome the limitations and extend the scope of the thesis are presented.

Appendix A presents information about the large eddy simulation [14] used in this thesis to analyse turbulence statistics in the jet plume. Appendix B describes the RANS simulations [15] used to predict the farfield noise with the scheme presented in Chapter 4.

Chapter 2

Background theory

Turbulent flows have a wide wavenumber-frequency spectrum, of which acoustic fluctuations are one component. Acoustic fluctuations are distinct because they are non-dissipative and non-dispersive, and propagate to large distances from the region of turbulence. This possibility to propagate is due to a relationship between a physical property of the fluid and the specific wavenumber-frequency component of sound. It is as if for the particular wavenumber–frequency of sound the fluctuations hit a resonance of the fluid, so the fluctuations can propagate to large distances.

With this view of aerodynamic sound there is no specific mechanism of sound generation in turbulent flows. Sound is but one component of the wavenumber-frequency spectrum of turbulence, so it is "generated" as any other component of the spectrum—i.e. via non-linear interactions of the turbulent fluctuations in the flow. Thus the goal of this thesis is to model the acoustic component of the turbulence spectrum in order to predict jet mixing noise.

Section 2.1 presents an acoustic analogy that relates mathematically the farfield acoustic spectrum to the wavenumber-frequency spectrum of turbulence. This is the fundamental theory of aerodynamic sound used in the remaining of the thesis.

2.1 No-flow acoustic analogy

An acoustic analogy is a rearrangement of the equations of fluid motion that distinguishes turbulent and acoustic fluctuations in the flow. The acoustic analogy presented in this section results in a non-homogeneous wave equation for a homogeneous fluid a rest. The resulting acoustic analogy is referred to as a no-flow acoustic analogy because the fluid is considered quiescent for the acoustic operator. The formulation differs from the one presented by Lighthill [7] by using energy equation—Lighthill used only the continuity and momentum equations.

The non-homogeneous terms of the wave equation are equivalent sources of sound. There remains, however, ambiguity in the definition of these equivalent sources. Other acoustic analogies—e.g., those by Lilley [9] and Goldstein [16]—result in different equivalent sources. Despite the ambiguity, the acoustic analogy has been validated to predict aerodynamic sound hence its application as the fundamental theory in this thesis.

In the acoustic analogy by Lighthill the continuity and momentum equations are rewritten as the non-homogeneous wave equation for a hypothetical homogeneous medium at rest. The resulting forcing term is a field of equivalent sources related to non-linear fluctuations in the flow. Another ambiguity in the definition of these equivalent sources arises: the turbulent and acoustic field are present in the field of equivalent sources.

An important difference between turbulent and acoustic fields enable practical application of the acoustic analogy: the turbulent field is in general confined to a smaller region of space than the acoustic field. Therefore, the acoustic analogy can be applied to compute the acoustic field in a region where turbulence has already decayed. That region coincides with the acoustic farfield of traditional acoustics, thus enabling further simplifications of the acoustic formulation. Moreover, for aircraft applications we are often interested in computing the noise in the farfield, where the noise affects a large number of people outside the aircraft and where certification measurements are taken.

It should be noted that to apply an acoustic analogy it is considered that the acoustic field does not affect the non-linear source field, so that the equivalent sources can be computed independently of the solution of the acoustic field.

2.1.1 Derivation of the wave equation

The derivation starts with the equations of fluid motion. These equations are derived from the assumption of the fluid as a continuum, followed by the application of the conservation of mass for a portion of fluid, the application of Newton's second law, and the application of the conservation of energy. As molecular diffusive effects are small in high-Reynolds-number flows, the fluid is herein assumed inviscid and with zero thermal conductivity. So the continuity, momentum, and energy equations reduce to the Euler equations. They can be written in the so-called conservative form as

$$\frac{\partial \rho}{\partial t} + \frac{\partial \rho U_i}{\partial x_i} = 0. \tag{2.1}$$

$$\frac{\partial \rho U_i}{\partial t} + \frac{\partial \rho U_i U_j}{\partial x_j} = -\frac{\partial p}{\partial x_i}, \tag{2.2}$$

and

$$\frac{\partial \rho h}{\partial t} + \frac{\partial \rho U_i h}{\partial x_i} = \frac{\partial p}{\partial t} + U_i \frac{\partial p}{\partial x_i}, \tag{2.3}$$

in which ρ is the density, U_i is the instantaneous velocity vector, h is the enthalpy, and p is the pressure.

The acoustic field can be computed by solving Eqs. (2.1), (2.2), and (2.3). A general analytical solution for these equations has not been found, and numerical solutions are expensive. Therefore, another way to predict the acoustic field without solving the equations of fluid motion is sought. This can be done by manipulating the equations of fluid motion in the form of an acoustic equation.

In the derivation of the no-flow acoustic analogy the equations of fluid motion are rearranged as a single scalar equation that describes the development of acoustic field. The manipulation is split in two steps. First, the momentum and continuity equations are combined into a non-homogeneous equation, resulting in a forcing term related to

fluctuating momentum fluxes and a non-barotropic forcing term related to thermodynamic fluctuations. Second, the energy equation is used to rewrite the non-barotropic term in terms of enthalpy.

The equations of continuity and momentum (Eqs. (2.1) and (2.2)) can be combined because the term ρU_i appears in both equations. However, it is the divergence of ρU_i that appears in the continuity equation, whereas it is the time derivative of ρU_i that appears in the momentum equation. Assuming that the order of derivation is interchangeable, the equations can be combined by taking the time derivative of the continuity equation and the divergence of the momentum equations. This is also considered in the traditional derivation of acoustics, but the equations are linearised first; in the acoustic analogy, the non-linear terms are kept and considered as equivalent sources of sound.

Taking the time derivative of the continuity equation ($\partial/\partial t$ (2.1)) and the divergence of the momentum equation ($\partial/\partial x_i$ (2.2)) yields, respectively,

$$\frac{\partial^2 \rho}{\partial t^2} + \frac{\partial^2 \rho U_i}{\partial t \partial x_i} = 0, \tag{2.4}$$

and

$$\frac{\partial^2 \rho U_i}{\partial x_i \partial t} + \frac{\partial^2 \rho U_i U_j}{\partial x_i \partial x_j} = -\nabla^2 p, \tag{2.5}$$

in which $\nabla^2 \equiv \partial^2/\partial x_i \partial x_i$ is the Laplacian operator. The divergence of the momentum equation is a scalar equation, so it can be now combined with the time derivative of the continuity equation.

Combining Eqs. (2.4) and (2.5) and rearranging the terms yields

$$-\nabla^2 p = \frac{\partial^2 \rho U_i U_j}{\partial x_i \partial x_j} - \frac{\partial^2 \rho}{\partial t^2}. \tag{2.6}$$

The left hand side of Eq. (2.6) differs from the wave operator only by $a_0^{-2}\partial^2 p/\partial t^2$. Therefore it is a matter of adding this term to both sides of the equation to make the left hand side the wave operator for an homogeneous medium at rest. Such additional term is ad hoc, arbitrary, but nevertheless exact. The non-homogeneous wave equation

in the form of a no-flow acoustic analogy is

$$\frac{1}{a_0^2}\frac{\partial^2 p}{\partial t^2} - \nabla^2 p = \frac{\partial^2 \rho U_i U_j}{\partial x_i \partial x_j} + \frac{\partial^2}{\partial t^2}\left(\frac{p}{a_0^2} - \rho\right). \tag{2.7}$$

Equation (2.7) is the wave equation for a homogeneous medium at rest with two source terms. The first source term is related to non-linearities in the flow, and the second one to departures from a barotropic state of the flow; they are assumed the sources of aerodynamic sound. The two independent source terms are related to fluctuations of momentum fluxes and non-barotropic fluctuations of the thermodynamic state of the fluid.

The dimensional analysis of the momentum term presented by Lighthill [7] predicts that the total noise power emitted by a turbulent jet scales with the eighth power of the jet-exit velocity. That agrees with measurements of jets with the same density as the ambient medium. The non-barotropic term, however, is not in a convenient form for analysis, as it is due to a difference of two small quantities.

Morfey [17] rewrote the non-barotropic term in a more convenient form and showed that its power output scales with the sixth power of the jet-exit velocity. The combination of the eighth-power momentum term with the sixth-power non-barotropic term predicted the observed trends of noise output from jets with density different from the ambient medium—i.e. cold or hot jets, and jets of a different gas.

In the derivation of this thesis the energy equation is used to rewrite the non-barotropic source term of Eq. (2.7). Lilley [18, 19] showed that using the energy equation enables writing the non-barotropic term in terms of fluctuating fluxes of enthalpy.

The following steps of the derivation use the energy equation (Eq. (2.3)) and an equation of state for the fluid to rewrite the non-barotropic term. The term $U_i \partial p/\partial x_i$ in the energy equation is rewritten using the momentum equation. This can be done by multiplying the momentum equation (Eq. (2.2)) by U_i. So the energy equation (Eq. (2.3)) may be written as

$$\frac{\partial \rho h}{\partial t} + \frac{\partial \rho U_i h}{\partial x_i} = \frac{\partial p}{\partial t} - \rho \frac{D U_i U_i/2}{Dt}. \tag{2.8}$$

Assuming an ideal gas, the equation of state is given by

$$\rho h = p\frac{\kappa_0}{\kappa_0 - 1}, \tag{2.9}$$

in which κ is the ratio of specific heats of the gas, which is assumed the same for the jet and the homogeneous medium, and the subscript 0 denotes the value for the hypothetical homogeneous medium. Using the equation of state to rewrite ρh in terms of p in Eq. (2.8) and combining the terms on $\partial p/\partial t$ yields

$$\frac{1}{\kappa_0 - 1}\frac{\partial p}{\partial t} + \frac{\partial \rho U_i h}{\partial x_i} = -\rho\frac{DU_iU_i/2}{Dt}. \tag{2.10}$$

Also for an ideal gas, it follows that

$$\kappa_0 - 1 = a_0^2/h_0.$$

Using this relation for $\kappa_0 - 1$ in Eq. (2.10) and dividing by h_0 yields

$$\frac{1}{a_0^2}\frac{\partial p}{\partial t} = -\frac{1}{h_0}\left(\frac{\partial \rho U_i h}{\partial x_i} + \rho\frac{DU_iU_i/2}{Dt}\right). \tag{2.11}$$

Taking the time derivative of Eq. (2.11) and combining with the time derivative of the continuity equation (2.4) yields

$$\frac{\partial^2}{\partial t^2}\left(\frac{p}{a_0^2} - \rho\right) = -\frac{\partial}{\partial t}\left[\frac{\partial}{\partial x_i}\rho U_i(h/h_0 - 1)\right] - \frac{1}{h_0}\frac{\partial}{\partial t}\left(\rho\frac{D}{Dt}U_iU_i/2\right). \tag{2.12}$$

By using the energy equation to the derive an acoustic analogy it is possible to rewrite the non-barotropic term, $\partial^2 p/a_0^2 - \rho\partial t^2$, as the contribution from an enthalpy and a kinetic energy term. The form is more convenient because the non-barotropic term is rewritten as fluctuating fluxes of enthalpy, which have a similar form of the momentum source term, and a material derivative of fluctuating kinetic energy.

Considering that the sound generation is due to local imbalances of fluxes of enthalpy or kinetic energy, it follows that the contribution from the kinetic energy term is smaller because it is related to a material derivative. Therefore, the the kinetic energy

term is discarded (a simplification also considered by Lilley [18, 19]).

Using the result of Eq. (2.12) after neglecting the kinetic energy term, the no-flow acoustic analogy used in this thesis takes the final form:

$$\frac{1}{a_0^2}\frac{\partial^2 p}{\partial t^2} - \nabla^2 p = \frac{\partial^2 \rho U_i U_j}{\partial x_i \partial x_j} - \frac{\partial^2}{\partial t \partial x_i}\rho U_i (h - h_0)/h_0. \tag{2.13}$$

This equation was derived from a rearrangement of the equations of fluid motion and an equation of state for an ideal gas, and identifies two sources. Both sources are related to fluxes of fluid properties, one related to fluctuating momentum fluxes which has a quadrupole order, and another related to fluctuating enthalpy fluxes which has a dipole order.

The acoustic problem of Eq. (2.13) is stated for an ideal homogeneous acoustic medium at rest with an imposed source field. Such source field results from an exact manipulation of the equations of fluid motion, but it is still taken as an arbitrary imposed field. The arbitrariness is evident in that the source field accounts for non-homogeneities of density, whereas the acoustic medium is homogeneous. Such arbitrariness was highlighted in the step when $a_0^{-2}\partial^2 p/\partial t^2$ was added to Eq. (2.6) to write Eq. (2.7). Such duality (homogeneous acoustic medium with non-homogeneous source field) highlights the underlying assumption of the acoustic analogy presented in this Chapter that the source field and acoustic medium are treated independently.

Regarding the acoustic field as homogeneous allows the use of the free-field Green's function to solve the acoustic problem stated in Eq. (2.13). In the next section the farfield solution of the wave equation for these two sources is used to compute the acoustic farfield generated by turbulent flows.

2.1.2 Solution for farfield pressure

The wave equation is now used to compute the pressure generated by a finite region of turbulence. Figure 2.1 depicts a jet flow which represents such finite region of turbulence. The coordinates in the figure represent the source location by **x** and the location

of the farfield observer by **r**.

The linearity of the wave equation (Eq. 2.13) allows the farfield pressure to be written as a sum of the contributions from the different source terms. Writing p^m for the farfield pressure generated by the momentum term, and p^h for the farfield pressure generated by the enthalpy term, the farfield pressure may be written as

$$p(\mathbf{r},t) = p^m(\mathbf{r},t) + p^h(\mathbf{r},t). \tag{2.14}$$

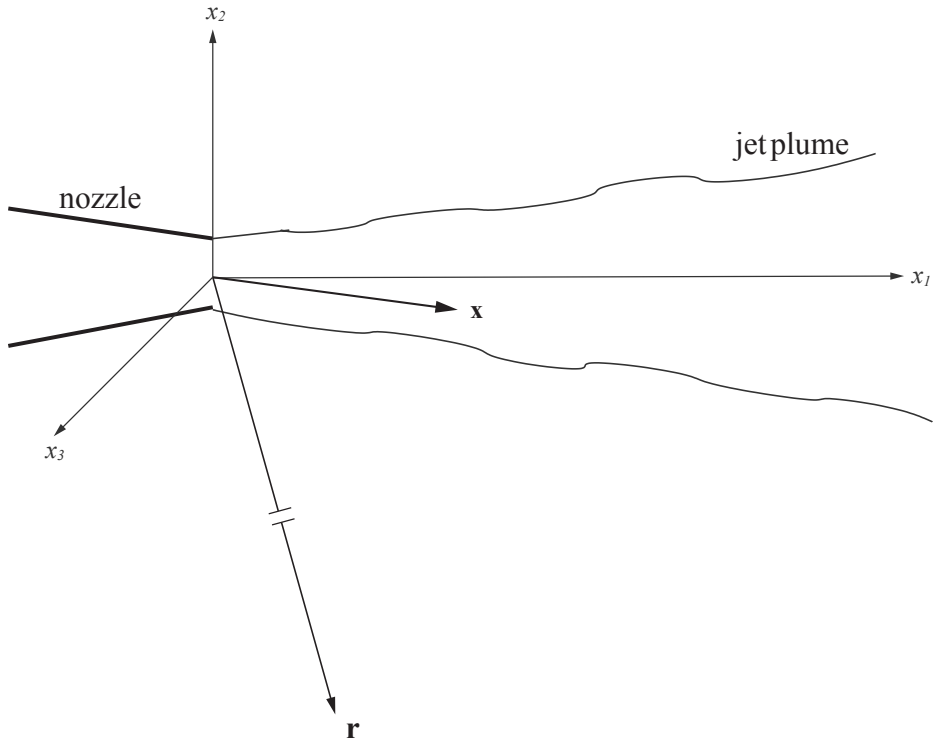

FIGURE 2.1: Coordinate system showing locations in the source region, **x**, and in the farfield, **r**.

The solution of the wave equation of the no-flow acoustic analogy (Eq. (2.13)) can be written in integral form with the free-field Green's function. So the solution for the acoustic field generated by the momentum and the enthalpy terms are, respectively:

$$p^m(\mathbf{r},t) = \int \frac{1}{4\pi\,|\mathbf{r}-\mathbf{x}|} \left\{ \frac{\partial^2}{\partial x_i \partial x_j} \rho U_i U_j \right\} \mathrm{d}^3\mathbf{x}, \tag{2.15}$$

and

$$p^h(\mathbf{r},t) = -\int \frac{1}{4\pi|\mathbf{r}-\mathbf{x}|}\left\{\frac{\partial^2}{\partial t\partial x_i}\rho U_i\left(h/h_0-1\right)\right\}\mathrm{d}^3\mathbf{x}, \tag{2.16}$$

in which $|\mathbf{r}-\mathbf{x}|$ is the separation between source and observer, and the terms inside the curly brackets are evaluated at the source location $\mathbf{x}$ and retarded time $t-|\mathbf{r}-\mathbf{x}|/a_0$. These solutions are simplified by application of farfield approximations.

The usual farfield approximations are presented in three steps. First, because the source terms are non-zero only in a limited region of space and after integrating by parts, the space derivatives can be moved out of the volume integral. So Eqs. (2.15) and (2.16) are written:

$$p^m(\mathbf{r},t) = \frac{\partial^2}{\partial x_i\partial x_j}\int \frac{1}{4\pi|\mathbf{r}-\mathbf{x}|}\left\{\rho U_i U_j\right\}\mathrm{d}^3\mathbf{x}, \tag{2.17}$$

and

$$p^h(\mathbf{r},t) = -\frac{\partial^2}{\partial t\partial x_i}\int \frac{1}{4\pi|\mathbf{r}-\mathbf{x}|}\left\{\rho U_i\left(h/h_0-1\right)\right\}\mathrm{d}^3\mathbf{x}. \tag{2.18}$$

This approximation is valid when r is taken in a sufficiently large distance where the source terms, effectively the turbulent kinetic energy, have decayed to low enough levels.

Second, the distance between source and observer is simplified. For the term defining the decay of pressure amplitude with distance, $|\mathbf{r}-\mathbf{x}|^{-1}$, the distance between source and observer is simplified to $r \equiv |\mathbf{r}|$ on account that $r \gg |\mathbf{x}|$. For the retarded time, however, it is necessary to keep differences within the source region to account for phase differences between the sources. Therefore, the approximation is less restrictive and amounts to

$$|\mathbf{r}-\mathbf{x}| \approx r - \hat{r}_i x_i,$$

in which $\hat{r}_i = r_i/r$ is the unity vector in the direction of the observer.

The two simplifications of $|\mathbf{r}-\mathbf{x}|$ are used to rewrite Eqs. (2.17) and (2.18)

$$p^m(\mathbf{r},t) = \frac{1}{4\pi r}\frac{\partial^2}{\partial x_i\partial x_j}\int \left\{\rho U_i U_j\right\}\mathrm{d}^3\mathbf{x}, \tag{2.19}$$

and

$$p^h(\mathbf{r},t) = -\frac{1}{4\pi r}\frac{\partial^2}{\partial t \partial x_i}\int \{\rho U_i (h/h_0 - 1)\}\,\mathrm{d}^3\mathbf{x}, \tag{2.20}$$

in which the retarded time for the terms inside the curly brackets is $t - (r - \hat{r}_i x_i)/a_0$.

With the third simplification, the space derivatives in the source coordinate are written in terms of time derivatives—this is possible on account of the approximations made to the retarded time, see Howe [20]. So the equations for the acoustic field due to the momentum and enthalpy terms are written as:

$$p^m(\mathbf{r},t) = \frac{\hat{r}_i \hat{r}_j}{4\pi a_0^2 r}\frac{\partial^2}{\partial t^2}\int \left\{\rho U_i U_j\right\}\mathrm{d}^3\mathbf{x}, \tag{2.21}$$

and

$$p^h(\mathbf{r},t) = \frac{\hat{r}_i}{4\pi a_0 r}\frac{\partial^2}{\partial t^2}\int \{\rho U_i (h/h_0 - 1)\}\,\mathrm{d}^3\mathbf{x}. \tag{2.22}$$

This third step changes the signal only of the equation for p^h. For the momentum term the result is positive because the signal is changed twice. For the enthalpy term the signal change is performed only once so the equation changes from negative to its final positive form.

Introducing the velocity component in the direction of the observer $U_r = \hat{r}_i U_i$, the tensor operations in Eqs. (2.21) and (2.22) show that the source terms must be computed in the direction of the observer (as written by Proudman [21]). That is,

$$\hat{r}_i \hat{r}_j U_i U_j = U_r^2 \tag{2.23}$$

and, by definition,

$$\hat{r}_i U_i = U_r. \tag{2.24}$$

Despite resembling an index notation, U_r is a scalar. The following definitions of the source terms and the resulting equations that contain U_r, therefore, are also scalars.

Using the notation for U_r, the momentum and enthalpy source terms for an observer at $\mathbf{r}$ can be written as

$$q_r^m = \rho U_r^2, \tag{2.25}$$

$$q_r^h = \rho U_r (h/h_0 - 1). \tag{2.26}$$

The definition of the source terms in Eq. (2.21) and (2.22) yields

$$p^m(\mathbf{r},t) = \frac{1}{4\pi a_0^2 r} \frac{\partial^2}{\partial t^2} \int \{q_r^m\} \mathrm{d}^3\mathbf{x}, \tag{2.27}$$

$$p^h(\mathbf{r},t) = \frac{1}{4\pi a_0 r} \frac{\partial^2}{\partial t^2} \int \{q_r^h\} \mathrm{d}^3\mathbf{x}. \tag{2.28}$$

In which the terms in the curly brackets are computed at location $\mathbf{x}$ and retarded time $t - (r - \hat{r}_i x_i)/a_0$.

Equations (2.27) and (2.28) show that the solution for the momentum and enthalpy sources are similar. The main difference is the efficiency of the source terms, with the term $1/a_0^2$ for the momentum quadrupole and $1/a_0$ for the enthalpy dipole.

2.1.3 Equation for farfield autospectral density

The time evolution of the farfield pressure can be computed by the solution of the non-homogeneous wave equations (Eqs. (2.27) and (2.28)) if the evolution in time of the sources is known. Sarkar and Hussaini [22] presented a numerical solution of these equation for isotropic turbulence, and Freund [4] did so for a jet of Reynolds number 3600. These numerical solutions have deterministic information about the sound sources and the acoustic field; however, they must be treated statistically for comparison with experimental data. Hence the application of the no-flow acoustic analogy to describe the acoustic farfield in statistical terms.

The pressure in the acoustic farfield can be described by its autospectral density. The pressure autospectral density forms a Fourier pair with the pressure autocorrelation, so it can be computed by

$$S_{pp}(\mathbf{r},\omega) = \int_{-\infty}^{\infty} \overline{p(\mathbf{r},t)p(\mathbf{r},t+\tau)} \exp(-i\omega\tau) \mathrm{d}\tau, \tag{2.29}$$

in which the overline indicates time average.

Decomposing the pressure field in contributions from the momentum and enthalpy terms, the pressure autospectral density is the sum of the contribution from the momentum source term, form the enthalpy source term, and from the cross-term between the momentum and enthalpy sources. The momentum and enthalpy sources are assumed statistically independent, so the cross-term is neglected and the farfield spectrum is written as

$$S_{pp}(\mathbf{r},\omega) = S^m_{pp}(\mathbf{r},\omega) + S^h_{pp}(\mathbf{r},\omega), \tag{2.30}$$

in which S^m_{pp} is the farfield spectrum due to the contribution from the momentum source and S^h_{pp} is due to the enthalpy source. The contribution from the momentum and enthalpy terms to the farfield spectrum can be analysed independently. This is done by using the farfield solutions for p^m and p^h given by Eqs. (2.27) and (2.28) to compute the pressure autocorrelation as:

$$S^m_{pp}(\mathbf{r},\omega) = \int_{-\infty}^{\infty} \overline{p^m(\mathbf{r},t)p^m(\mathbf{r},t+\tau)}\exp(-i\omega\tau)\mathrm{d}\tau, \tag{2.31}$$

$$S^h_{pp}(\mathbf{r},\omega) = \int_{-\infty}^{\infty} \overline{p^h(\mathbf{r},t)p^h(\mathbf{r},t+\tau)}\exp(-i\omega\tau)\mathrm{d}\tau. \tag{2.32}$$

The following derivation is analogous for the momentum and enthalpy terms, so only the derivation for the momentum term is presented.

The pressure autocorrelation in the farfield is computed using the farfield solution for p^m (Eq. (2.27)):

$$\overline{p^m(\mathbf{r},t)p^m(\mathbf{r},t+\tau)} = \frac{1}{16\pi^2 a_0^4 r^2}\frac{\partial^4}{\partial t^4}\iint \overline{q^m_r(\mathbf{x}^A,t^A)q^m_r(\mathbf{x}^B,t^B)}\mathrm{d}^3\mathbf{x}^A\mathrm{d}^3\mathbf{x}^B \tag{2.33}$$

in which $t^A = t-(r-\hat{r}_i x^A_i)/a_0$ and $t^B = t-(r-\hat{r}_i x^B_i)/a_0+\tau$. (See Ffowcs-Williams [23] for a similar formulation.)

Assuming stationary turbulence, the time average on the right hand side of Eq. (2.33) is independent of time translations. Introducing the separation vector, $\mathbf{s} = \mathbf{x}^B - \mathbf{x}^A$, and

adding $(r-\hat{r}_i x_i^A)/a_0$ to both t^A and t^B yields

$$\overline{p^m(\mathbf{r},t)p^m(\mathbf{r},t+\tau)} = \frac{1}{16\pi^2 a_0^4 r^2}\frac{\partial^4}{\partial t^4}\iint \overline{q_r^m(\mathbf{x},t)q_r^m(\mathbf{x}+\mathbf{s},t+\tau+\hat{\mathbf{r}}\cdot\mathbf{s}/a_0)}\mathrm{d}^3\mathbf{s}\mathrm{d}^3\mathbf{x}, \tag{2.34}$$

in which the superscript A is now dropped, and $\mathrm{d}^3\mathbf{s} = \mathrm{d}^3\mathbf{x}^B$.

The space–time correlation of the momentum source term is introduced,

$$R_r^m(\mathbf{x};\mathbf{s};\tau+\hat{\mathbf{r}}\cdot\mathbf{s}/a_0) = \overline{q_r^m(\mathbf{x},t)q_r^m(\mathbf{x}+\mathbf{s},t+\tau+\hat{\mathbf{r}}\cdot\mathbf{s}/a_0)}, \tag{2.35}$$

so Eq. (2.34) is rewritten as

$$\overline{p^m(\mathbf{r},t)p^m(\mathbf{r},t+\tau)} = \frac{1}{16\pi^2 a_0^4 r^2}\frac{\partial^4}{\partial t^4}\iint R_r^m(\mathbf{x};\mathbf{s};\hat{\mathbf{r}}\cdot\mathbf{s}/a_0+\tau)\mathrm{d}^3\mathbf{s}\mathrm{d}^3\mathbf{x}. \tag{2.36}$$

The autospectral density of the contribution from the momentum term, S_{pp}^m, is computed by taking the Fourier transform of the pressure autocorrelation (Eq. (2.36)):

$$S_{pp}^m(\mathbf{r},\omega) = \frac{\omega^4}{16\pi^2 a_0^4 r^2}\iiint R_r^m(\mathbf{x};\mathbf{s};\tau+\hat{\mathbf{r}}\cdot\mathbf{s}/a_0)\exp(-i\omega\tau)\mathrm{d}\tau\mathrm{d}^3\mathbf{s}\mathrm{d}^3\mathbf{x}, \tag{2.37}$$

in which ω^4 results from taking the Fourier transform of a fourth-order time derivative.

The change of variable $\tau^* = \tau+\hat{\mathbf{r}}\cdot\mathbf{s}/a_0$ is introduced, which results in $\mathrm{d}\tau^* = \mathrm{d}\tau$, so the integral on the right hand side of Eq. (2.37) may be written as

$$S_{pp}^m(\mathbf{r},\omega) = \frac{\omega^4}{16\pi^2 a_0^4 r^2}\iiint R_r^m(\mathbf{x};\mathbf{s};\tau^*)\exp\left[-i\omega\left(\tau^*-\hat{\mathbf{r}}\cdot\mathbf{s}/a_0\right)\right]\mathrm{d}\tau^*\mathrm{d}^3\mathbf{s}\mathrm{d}^3\mathbf{x}. \tag{2.38}$$

The change in variable changed the argument of the exponential: now the term $\hat{\mathbf{r}}\cdot\mathbf{s}/a_0$, related to differences in retarded time, appears explicitly. In this form the effect of retarded time differences, which leads to source interference, appears more explicitly.

The integral with space separation in Eq. (2.38) can be written as a Fourier transform. The Fourier of the space–time correlation is

$$\mathscr{F}\left[R_r^m(\mathbf{x};\mathbf{s};\tau^*)\right] = \int_{-\infty}^{+\infty} R_r^m(\mathbf{x};\mathbf{s};\tau^*)\exp\left(-i\omega\tau^*\right)\mathrm{d}\tau^*, \tag{2.39}$$

so Eq. (2.38) is

$$S_{pp}^{m}(\mathbf{r};\omega) = \frac{\omega^4}{16\pi^2 a_0^4 r^2} \iint \mathscr{F}\left[R_r^m(\mathbf{x};\mathbf{s};\tau^*)\right] \exp\left(i\frac{\omega}{a_0}\hat{\mathbf{r}}\cdot\mathbf{s}\right) \mathrm{d}^3\mathbf{s}\mathrm{d}^3\mathbf{x}. \tag{2.40}$$

The derivation for the enthalpy source is analogous to the one for the momentum term. The resulting equation for the contribution from the enthalpy source to the farfield autospectral density is

$$S_{pp}^{h}(\mathbf{r};\omega) = \frac{\omega^4}{16\pi^2 a_0^2 r^2} \iint \mathscr{F}\left[R_r^h(\mathbf{x};\mathbf{s};\tau^*)\right] \exp\left(i\frac{\omega}{a_0}\hat{\mathbf{r}}\cdot\mathbf{s}\right) \mathrm{d}^3\mathbf{s}\mathrm{d}^3\mathbf{x}, \tag{2.41}$$

in which R_r^h is the space–time correlation of the enthalpy source.

The application of the no-flow acoustic analogy shows the relationship between the farfield acoustic spectrum and turbulence two-point statistics (the Fourier transform of space–time correlations). This thesis presents methods that use empirical models to compute turbulence two-point statistics. The background theory of turbulence statistics needed to apply such empirical modelling is presented in the next section.

2.2 Statistical description of turbulence

Describing turbulence in statistical terms was a major breakthrough in our understanding of turbulence in the early 20$^{\text{th}}$ century. A statistical description of turbulence is applied to study fundamental aspects of turbulence and to develop low-order models of turbulence. In this thesis such statistical tools are used to model turbulence two-point turbulence statistics.

Statistical quantities are defined in Sections 2.2.1–2.2.3 and are used to analyse numerical data and to propose empirical models of turbulence statistics.

2.2.1 Correlation function

The correlation function measures the degree of relationship between two signals. The signals can be of two different variables or the same variables computed at different locations. The latter case is considered in this thesis, and so the correlation function is referred to as the space–time correlation.

The space–time correlation of the velocity fluctuation u_i computed at $\mathbf{x}$, with space separation $\mathbf{s}$, and time separation τ is

$$R_{ii}(\mathbf{x};\mathbf{s};\tau) = \overline{u_i(\mathbf{x},t)u_i(\mathbf{x}+\mathbf{s},t+\tau)}, \tag{2.42}$$

in which the overline indicates time average. In the definition of the correlation and in the remaining of the thesis index repetition does not indicate summation.

The space–time correlation of the squared velocity fluctuation is necessary to model jet noise; it is defined as

$$R_{iiii}(\mathbf{x};\mathbf{s};\tau) = \overline{u_i^2(\mathbf{x};t)u_i^2(\mathbf{x}+\mathbf{s};t+\tau)}. \tag{2.43}$$

2.2.2 Integral length scale

The turbulence integral length scale represents and average size of the turbulent eddies with different wavenumbers. The integral length scale does not represent the size of the largest due to the randomizing nature of the smaller eddies. (It is shown in Chapter 7 that the largest coherence length is scale is almost an order of magnitude larger than the integral length scale.) Batchelor [24] gives the definition of the integral length scale for velocity fluctuations in isotropic turbulence as

$$L_{ii}(\mathbf{x}) = \int_0^{+\infty} R_{ii}(\mathbf{x};s_1;\tau=0)\mathrm{d}s, \tag{2.44}$$

in which $s = |\mathbf{s}|$.

The definition is herein generalised for the anisotropic turbulence in jets by considering the separation in the direction of the mean flow whilst accounting for different velocity components. Assuming that the main direction of the mean flow is aligned with the axis x_1, the integral length scale in jets is defined as

$$L_{ii}(\mathbf{x}) = \int_0^{+\infty} R_{ii}(\mathbf{x}; s_1; \tau = 0) \mathrm{d}s_1. \tag{2.45}$$

The integral length scale depends on the location in the jet and the velocity component. For instance, the integral length scale for u_1 is L_{11} and the integral length scale for u_2 is L_{22}.

The integral length scale of u_i^2 is

$$L_{iiii}(\mathbf{x}) = \int_0^{+\infty} R_{iiii}(\mathbf{x}; s_1; \tau = 0) \mathrm{d}s_1. \tag{2.46}$$

Taylor's hypothesis

The integral length scale requires an integral with space separation. High space resolution is difficult to achieve either numerically or experimentally. So it is more convenient to rewrite the definition in terms of an integral with time separation. This can be done by assuming that a space separation in the direction of the mean flow is equivalent to a time separation multiplied by the mean flow velocity, i.e. $s_1 = \tau \overline{U}_1$. Such assumption is referred to as "Taylor's hypothesis".

Assuming Taylor's hypothesis is valid, the integral length scale u_i may be computed by

$$L_{ii}(\mathbf{x}) = \overline{U}_1(\mathbf{x}) \int_0^{+\infty} R_{ii}(\mathbf{x}; s_1 = 0; \tau) \, \mathrm{d}\tau. \tag{2.47}$$

and the integral length scale of u_i^2 is

$$L_{iiii}(\mathbf{x}) = \overline{U}_1(\mathbf{x}) \int_0^{+\infty} R_{iiii}(\mathbf{x}; s_1 = 0; \tau) \, \mathrm{d}\tau. \tag{2.48}$$

2.2.3 Cross-spectral density

The cross-spectral density gives the level of correlation between two signals at a given frequency. For the application in this thesis, the cross-spectral density is computed between the signal of the same variable shifted in space; so, for instance, the cross-spectral density of u_i is the cross-spectral density between the values of u_i at different locations in space. The cross-spectral density of u_i is thus the Fourier transform of its space–time correlation:

$$C_{ii}(\mathbf{x};\mathbf{s};\omega) = \mathscr{F}\left[R_{ii}(\mathbf{x};\mathbf{s};\tau)\right]. \tag{2.49}$$

And the same definition is applied for the cross-spectral density of u_i^2:

$$C_{iiii}(\mathbf{x};\mathbf{s};\omega) = \mathscr{F}\left[R_{iiii}(\mathbf{x};\mathbf{s};\tau)\right]. \tag{2.50}$$

The cross-spectral density is a complex-valued variable, so it may be decomposed into magnitude and phase. The cross-power spectral density of u_i may thus be written as:

$$C_{ii}(\mathbf{x};\mathbf{s};\omega) = |C_{ii}(\mathbf{x};\mathbf{s};\omega)| \exp\left[-i\phi_{ii}(\mathbf{x};\mathbf{s};\omega)\right], \tag{2.51}$$

in which $\phi_{ii}(\mathbf{x};\mathbf{s};\omega)$ is the phase delay at ω between the signals at $\mathbf{x}$ and $\mathbf{x}+\mathbf{s}$.

The phase is computed from the imaginary and real parts of the cross-spectral density as:

$$\phi_{ii} = \arctan\left[\frac{\mathscr{I}[C_{ii}]}{\mathscr{R}[C_{ii}]}\right], \tag{2.52}$$

in which $\mathscr{I}[C_{ii}]$ is the imaginary part of C_{ii} and $\mathscr{R}[C_{ii}]$ is the real part of C_{ii}.

The magnitude of the cross-spectral density can be decomposed in the autospectral density of the signals and the coherence between them. For that, the coherence function of u_i is introduced:

$$\gamma_{ii}(\mathbf{x};\mathbf{s};\omega) = \frac{|C_{ii}(\mathbf{x};\mathbf{s};\omega)|}{\sqrt{S_{ii}(\mathbf{x};\omega)S_{ii}(\mathbf{x}+\mathbf{s};\omega)}}. \tag{2.53}$$

Using the definition of the coherence function, the cross-spectral density of u_i may be written as

$$C_{ii}(\mathbf{x};\mathbf{s};\omega) = \sqrt{S_{ii}(\mathbf{x};\omega)S_{ii}(\mathbf{x}+\mathbf{s};\omega)}\gamma_{ii}(\mathbf{x};\mathbf{s};\omega)\exp\left[-i\phi_{ii}(\mathbf{x};\mathbf{s};\omega)\right]. \tag{2.54}$$

And analogously for u_i^2:

$$C_{iiii}(\mathbf{x};\mathbf{s};\omega) = \sqrt{S_{iiii}(\mathbf{x};\omega)S_{iiii}(\mathbf{x}+\mathbf{s};\omega)}\gamma_{iiii}(\mathbf{x};\mathbf{s};\omega)\exp\left[-i\phi_{iiii}(\mathbf{x};\mathbf{s};\omega)\right]. \tag{2.55}$$

Decomposing the cross-spectral density into autospectral density, coherence, and phase enables an independent analysis of these three components. Developing an empirical term for each term is easier than for the complete cross-power spectral density directly, so the decomposition aids modelling jet noise.

Chapter 3

Review of RANS-based prediction methods

The first RANS-based methods to predict jet noise were presented in the early 1990s. Since then much progress has been made in the theory of aerodynamic sound and in the empirical description of turbulence statistics. This chapter highlights some of this progress by describing different jet noise prediction methods.

3.1 Prediction methods in the literature

The review of the methods aims to highlight the following aspects: (1) choice of acoustic analogy and resulting model for the sound sources, (2) empirical model for turbulence two-point statistics, and (3) scaling relations between the empirical models and the RANS k–ε solution of the mean flow. These three aspects focus only on the modelling of the sources of sound, because aspects of flow–acoustic interaction are out of the scope of the thesis. All methods are applied to predict the noise of subsonic jets; some methods for isothermal and hot jets, others only for isothermal jets. The methods reviewed in Sections 3.1.1–3.1.5 are grouped by research groups.

3.1.1 Khavaran et al.

Khavaran, Krejsa and Kim [8] presented one of the earliest RANS-based prediction method of the kind studied in this thesis. The sources of sound were described using the acoustic analogy by Lighthill [7] and modelled using an empirical model of velocity space–time correlation. The correlation model is based on an assumption of locally-homogeneous and isotropic turbulence, so that a Gaussian function is used to model the decay of correlation with space and with time separation. The correlation model takes the form:

$$R_{ii}(\mathbf{x};\mathbf{s};\tau) = R_{ii}(\mathbf{x};0;0)\exp\left(-\frac{\tau^2}{\tau_0^2(\mathbf{x})}\right)\exp\left(-\frac{|\mathbf{s}|}{\ell(\mathbf{x})}\right), \tag{3.1}$$

in which τ_0 is a time scale and ℓ is a length scale. The model assumes isotropic turbulence, so it does not change with component of velocity nor direction of separation.

Khavaran, Krejsa and Kim used the solution of the mean flow with a RANS k–ε model to compute the scaling parameters of the empirical space–time correlation model. The space–time correlation model needs a scale of magnitude, one of time, and one of length. These parameters are related to the turbulent kinetic energy, k, and turbulent dissipation rate, ε, both computed from the RANS k–ε solution of the flow.

The scales of magnitude, time and length are related to the RANS solution, respectively, by:

$$R_{ii}(\mathbf{x};0;0) = \alpha_k k(\mathbf{x}), \tag{3.2}$$

$$\tau_0(\mathbf{x}) = \alpha_\tau \frac{k(\mathbf{x})}{\varepsilon(\mathbf{x})}, \tag{3.3}$$

and

$$\ell(\mathbf{x}) = \alpha_\ell \frac{k^{3/2}(\mathbf{x})}{\varepsilon(\mathbf{x})}, \tag{3.4}$$

in which α_k, α_τ, and α_ℓ are empirical coefficients. The scales given by Eqs. (3.2)–(3.4) are hereafter referred to as the "traditional RANS scales".

Khavaran [25] studied the effect of turbulence anisotropy on the jet noise. He assumed turbulence axisymmetric and accounted for differences in the intensity and

length scale in the axial and transverse directions. Considering anisotropy improved the predictions for low polar angles by accounting for the larger intensity and length scale in the axial direction.

Khavaran et al. [8, 25] modelled only the momentum source of Lighthill's acoustic analogy, so the model was limited to isothermal jets. Khavaran, Kenzakowski and Mielke-Fagan [26] extended the model for hot jets by modelling the enthalpy source of the acoustic analogy by Goldstein [27]. Khavaran, Kenzakowski and Mielke-Fagan assumed that the momentum and enthalpy sources are statistically independent.

The model for two-point statistics of the enthalpy source is the same used for the momentum source, with only changes in the scaling parameters of magnitude, length, and time. But the empirical model was updated from the Gaussian decay used by Khavaran, Krejsa and Kim [8] to an exponential decay to match the measurements by Bridges and Wernet [28].

Khavaran, Kenzakowski and Mielke-Fagan [26] related the magnitude of the enthalpy source to the mean square value of temperature. Their model needs a specialised RANS solver because the temperature mean square is not computed by standard RANS solvers. The specialised solver needs further empirical calibration, thus increasing the empiricism of the prediction method for hot jets.

3.1.2 Tam et al.

Tam and Auriault [29] used the linearised Euler equations as an acoustic propagator with a forcing term. The forcing term is derived after an analogy with the kinetic theory of gas and is related to the turbulent kinetic energy. The linearised equations are written in an adjoint form [30] and the solution is given in terms of the two-point statistics of the source term.

The two-point statistics is computed using an empirical model for the space–time correlation of the source term. The model considers a Gaussian decay with space separation and an exponential decay with time—written as space separation via an implicit assumption of Taylor's hypothesis. The Gaussian decay is written in a moving

frame, thus accounting for effects of turbulence convection. The empirical model has been validated with the measurements of velocity space–time correlation by Davies, Fisher and Barrat [31], but there is no confirmation that the same behaviour is observed for space–time correlation of the source term by Tam and Auriault.

The correlation model used by Tam and Auriault can be written as

$$R_{qq}(\mathbf{x};\mathbf{s};\tau) = R_{qq}(\mathbf{x};0;0)\exp\left(-\frac{|\mathbf{s}|}{\overline{U}_1\tau_0}\right)\exp\left[-\frac{\ln 2}{\ell^2}\left[\left(s_1-\overline{U}_1\tau\right)^2+s_2^2+s_3^2\right]\right], \quad (3.5)$$

in which R_{qq} is the space–time correlation of the source term, and $\overline{U}_1$ is phase velocity of the turbulent fluctuations in the axial direction. The phase velocity, length scale (ℓ), and time scale (τ_0), vary with location in the jet.

The limitation for cold to moderate temperature jets in the formulation by Tam and Auriault was removed by Tam, Pastouchenko and Viswanathan [32]. The extended formulation changed the correlation model to match the experimental data of Doty and McLaughlin [33]. The modified model for the space–time correlation needs additional empirical coefficients, but improved farfield noise predictions for hot jets.

3.1.3 Morris et al.

Morris and Farassat [34] compared the model of Tam and Auriault [29] with a model derived from Lighthill's acoustic analogy which is similar to the model by Khavaran, Krejsa and Kim [8]. Morris and Farassat showed that the differences between the approach by Tam and Auriault and the model based Lighthill's acoustic analogy are mainly due to differences in the statistical description of turbulence. Morris and Farassat presented an acoustic analogy derived from the Euler equations which is similar to the formulation used by Tam and Auriault [29].

Morris and Boluriaan [35] extended the model based on the Euler equation presented by Morris and Farassat [34]. In the main body of the paper the source two-point statistics are computed by a model for the turbulence space–time correlation.

The correlation model is similar to the one used by Tam and Auriault [29]—convected-Gaussian decay with space separation and exponential decay with time separation and. In the appendix of the paper, Morris and Boluriaan [35] applied the model of two-point statistics in frequency domain presented by Harper-Bourne [12].

Raizada and Morris [36] applied from the outset the frequency domain model sketched by Morris and Boluriaan. The model extends the one by Harper-Bourne [12] by computing the autospectral density from the Fourier transform of a model for the autocorrelation—Harper-Bourne computed the autospectral density indirectly by matching the source distribution to measured data.

The autospectral density in Raizada and Morris [36] is modelled by a Lorentzian function, which is the Fourier transform of an exponential decay of the autocorrelation. The coherence decay is assumed to take a Gaussian form in the transverse direction and an exponential form in the axial direction, as proposed by Harper-Bourne [12]. The effect of phase is modelled by relating the phase velocity with the mean flow velocity and accounting for frequency-dependence as in Harper-Bourne [12].

Raizada and Morris corroborates the suggestions by Harper-Bourne [12] and Self [11] that modelling the two-point statistics in frequency domain makes it straightforward to model the observed frequency-dependence of the coherence length scale and convective velocity. The scaling parameters are related to the RANS solution via traditional RANS scales and empirical coefficients are calibrated with farfield data.

3.1.4 Self et al.

Self [11] modelled the momentum source term from Lighthill's acoustic analogy in frequency domain. The frequency-dependence of the turbulence length scale and of convective velocity observed by Harper-Bourne [12] were explicitly modelled. In Self [11] the jet is modelled as a line source, taking into account the growth of the shear layer width with axial coordinate. Self [37] extended the model by using information from a RANS k–ε solution of the jet, thus computing the three-dimensional source distribution in the jet.

Self and Azarpeyvand [13] applied the formulation by Khavaran, Krejsa and Kim [8], but considered the frequency-dependency of the time scale. They analysed the model by Self [11, 37] that explicitly considered frequency-dependence of the time scale and proposed a new time scale to model the frequency-dependence implicitly. The new time scale reduced the empiricism of the model when compared to Self [11, 37] whilst showing improvements in predictions.

The new time scale was analysed by Azarpeyvand and Self [38] within the formulation by Khavaran, Krejsa and Kim [8]. Azarpeyvand and Self simplified the time scale whilst keeping the same improvements in the predictions shown by Self and Azarpeyvand [13]. The simplified time scale implicitly accounts for the frequency-dependence by relating the process of sound generation to a different range of the turbulence wavenumber spectrum. The local wavenumber is related to the traditional RANS length scale, so that effectively the time scale is reduced for regions of smaller length scale.

The so-called "turbulent energy transfer" time scale can be written as

$$\tau_{0,TET} = \tau_0 \left(\frac{\ell}{D_J} \right)^{2/3}, \tag{3.6}$$

in which τ_0 and ℓ are the traditional RANS time and length scales.

Ilário et al. [10] applied the time scale by Azarpeyvand and Self to model the momentum source of Lightihll's acoustic analogy. Two-point turbulence statistics is computed using an empirical model for space–time correlation that assumes a Gaussian decay with space and time separation. The scales of magnitude and length are the traditional RANS scales, whereas the time scale is the one presented by Azarpeyvand and Self [38].

Rosa et al. [39] presented a comparison of the formulation by Ilário et al. [40, 10] with other methods [29, 34, 35] that use the traditional RANS time scale. It was shown that the formulation by Ilário et al. results in improvements without increasing the empiricism by using the time scale of Azarpeyvand and Self [41].

3.1.5 Karabasov et al.

Karabasov et al. [42] applied the acoustic analogy by Goldstein [27] to predict jet noise. The two-point statistics of the source term was computed with an empirical model of space–time correlation. The correlation model considers a convected-Gaussian decay with space separation and an exponential decay with time separation (in which time separation is written in terms of space separation divided by the mean velocity)—the same model used by Tam and Auriault [29]. The formulation by Karabasov et al. does not greatly differ from the one by Tam and Auriault [29] or Morris and Boluriaan [35]; but a major breakthrough was to use unsteady turbulent data in the entire jet plume to calibrate the scaling parameters of the correlation model.

The full source tensor was computed by relating the correlation model to different velocity components and length scales in different directions. With three-dimensional data available for the three velocity components from a large eddy simulation, Karabasov et al. computed the effect of turbulence anisotropy in the entire jet plume. Predictions at the sideline and low polar angle agreed well with farfield data without the need of an additional source—thus contradicting, e.g., Tam, Golebiowski and Seiner [43] and Jordan and Colonius [44].

Depuru-Mohan et al. [45] applied the formulation by Karabasov et al. to predict the noise from isothermal jets issued from a chevron nozzle. They showed that the calibration linking the large eddy simulation to the RANS solution for the baseline circular jet can be used for chevron nozzles. Thus, it was shown that the RANS k–ε solution accounts for the most important changes caused by the chevrons.

Semiletov and Karabasov [46] proposed an improvement of the correlation model used by Karabasov et al. [42]. The model was improved by modifying the exponent of the exponential argument—1 being an exponential decay, 2 being a Gaussian decay. The improved model uses a non-integer exponent for the space-separation decay and better fits turbulence data from large eddy simulation. However, the improved correlation model could not be used in the source model because an analytical Fourier transform was not found.

3.1.6 Summary

To summarise the review presented in the previous sections, five aspects of the methods are compared:

1. Choice of acoustic analogy and resulting source terms.
2. Empirical model of two-point statistics.
3. Scaling parameters of the empirical models (scales of magnitude, time, and length).
4. Calibration of the empirical models.
5. Operating conditions.

In the following paragraphs these five aspects are listed for each method reviewed in this chapter.

Khavaran et al.

1. Model momentum and enthalpy sources from Goldstein's acoustic analogy [27].
2. Compute two-point statistics with empirical model for space–time correlation. The empirical models assumes exponential decay with time separation and exponential decay with space separation. The space separation is written in a moving frame, thus accounting for effects of phase due to turbulence convection.
3. Use traditional RANS scales of time and length. The magnitude of the momentum term is related to the turbulent kinetic energy (the traditional RANS scale), and the magnitude of the enthalpy source is related to the mean square value of temperature.
4. Calibration with farfield data.
5. Validated for isothermal and hot jets.

Tam et al.

1. Model source term of formulation derived by the manipulation of the Euler equations [29].

2. Compute two-point statistics with empirical model for space–time correlation. The model assumes an exponential decay with time separation (written as space separation via implicit Taylor's hypothesis) and convected-Gaussian decay with space separation. For hot jets the correlation model is modified with local data from the mean density gradient.

3. Use traditional RANS scales.

4. Calibration with farfield data.

5. Validated for isothermal and hot jets.

Morris et al.

1. Model momentum term of acoustic analogy derived by the manipulation of the Euler equations [35].

2. Use empirical model of cross-spectral density by Harper-Bourne [12]. Extends Harper-Bourne's model by using a Lorentzian function to compute the autospectral density.

3. Use traditional RANS scales.

4. Calibration with farfield data.

5. Validated for isothermal jets.

Self et al.

1. Model the momentum term from Lighthill's acoustic analogy.

2. Model two-point statistics with empirical model of space–time correlation. The model assumes Gaussian decay with time and space separation.

3. Scales of magnitude and length are the traditional RANS scales. The time scale is the one by Azarpeyvand and Self [38].

4. Calibration with farfield data.

5. Validated for isothermal and hot jets.

Karabasov et al.:

1. Models the momentum term of the acoustic analogy by Goldstein [27].

2. Two-point statistics computed by empirical model of space–time correlation. Same model as Tam and Auriault [29].

3. Traditional RANS scales.

4. Calibration with unsteady data of turbulence in the jet plume.

5. Validated for isothermal jets.

3.2 Specific contributions of the thesis

The contributions of the thesis were presented in overall terms in Section 1.2. In this section the contributions are compared in more details to the methods reviewed in this chapter. The contributions are grouped in three: sound sources in hot jets, model for two-point statistics, and effect of turbulence anisotropy.

3.2.1 Source in hot jets

Previous work:

1. Ilário et al. [10] modelled only the momentum source term of Lighthill's acoustic analogy; so predictions for hot jets need temperature-dependent calibration.

2. Tam, Pastouchenko and Viswanathan [32] ignored an additional source in hot jets. They used the same source validated for isothermal jets with a different model for the space–time correlation.

3. Khavaran, Kenzakowski and Mielke–Fagan [26] modelled an additional source related to enthalpy fluxes. Their model requires a specialised RANS solver to compute the mean square value of temperature fluctuations.

Contributions of the thesis:

1. Show that the enthalpy source in a no-flow acoustic analogy that uses the energy equation is equivalent to the enthalpy source in the acoustic analogy by Lilley–Goldstein [9, 16].

2. Show that a standard RANS k–ε solver can be used to compute the contribution from the enthalpy source because the fluctuations of the enthalpy fluxes is dominated by the fluctuations of velocity.

3.2.2 Model for two-point statistics

Previous work:

1. Ilário et al. [10] assumed compact source in axial and transverse directions. The decay of space-time correlation with time and space separations was modelled with a Gaussian function.

2. Harper-Bourne [12] introduced a model for the cross-spectral density, splitting it into autospectral density, coherence function, and phase. However, he did not provide a model for the autospectral density; instead, farfield data was used to calibrate the source autospectral density.

3. Raizada and Morris [36] supplemented the model by Harper-Bourne with a Lorentzian function for the autospectral density. The Lorentzian function results from the Fourier transform of a correlation model that assumes exponential decay with time separation.

Contribution of the thesis:

1. Introduce the use of the von Kármán spectrum [47] to model the autospectral density of turbulence for jet noise modelling.

2. Use a modified von Kármán spectrum to model the spectrum of the coherence length scale.

3. Show that the effect of frequency-dependence of phase speed may be neglected for jet noise prediction.

3.2.3 Effect of turbulence anisotropy on jet noise directivity

Previous work:

1. Khavaran [25] modelled anisotropy due to the differences between transverse and axial length scales, and differences between mean square value of transverse and axial velocity fluctuations.

2. Karabasov et al. [42] used large eddy simulation data to adjust anisotropic scales of length and magnitude for the space–time correlation model. However, they did not present an explicit assessment of the effect of anisotropy.

Contributions of the thesis:

1. Show that the most significant effect of turbulence anisotropy on jet noise directivity is due to the anisotropy of integral length scale.

2. Use data from large eddy simulation to compute the effect of turbulence anisotropy on jet noise directivity and compare with farfield measured data.

In summary, the thesis updates the method by Ilário et al. [10] by (1) modelling the enthalpy source, (2) proposing the use of a frequency-domain model of turbulence statistics, and (3) using large eddy simulation to assess turbulence two-point statistics in the jet plume. Additionally, the thesis extends the current knowledge in jet noise modelling by (1) showing that a standard RANS k–ε solver can be used to model the

contribution from the enthalpy source, (2) introducing the application of von Kármán spectrum for jet noise modelling, and (3) using unsteady turbulence data to compute the effect of turbulence anisotropy on jet noise directivity.

Chapter 4

Prediction method with model for enthalpy source

The formulation presented in this chapter extends the source model of Ilário et al. [10] by adding a model for the enthalpy source of the no-flow acoustic analogy. The new method is presented in two forms. First, a scaling law is presented in Section 4.1 from a dimensional analysis of the no-flow acoustic analogy. The scaling law agrees with previous work in which the momentum source scales with U_J^8 and the enthalpy source scales with U_J^6.

Second, in Section 4.2, the no-flow acoustic analogy is applied to predict the farfield spectrum. The formulation is restricted to an observer at 90° degrees because of the neglect of flow–acoustic interaction and the assumptions of compact source and of isotropic turbulence.

4.1 Scaling laws

A dimensional analysis of the no-flow acoustic analogy is applied to derive a scaling law for the mean square value of the farfield pressure. The dimensional analysis starts with the equation for the autocorrelation of the acoustic pressure from the no-flow acoustic analogy (Eq. (2.36)). The acoustic pressure is split into contributions from the momentum source (p^m) and from the enthalpy source (p^h). The sources are assumed uncorrelated so the mean square pressure in the farfield is the sum of both

contributions:

$$\overline{p^2}(\mathbf{r}) = \overline{(p^m)^2}(\mathbf{r}) + \overline{(p^h)^2}(\mathbf{r}). \tag{4.1}$$

The contribution from the momentum term is given by the autocorrelation of p^m with zero separation ($\tau = 0$ in Eq. (2.36)):

$$\overline{(p^m)^2}(\mathbf{r}) = \frac{1}{16\pi^2 a_0^4 r^2} \frac{\partial^4}{\partial t^4} \iint R_r^m(\mathbf{x};\mathbf{s};\hat{\mathbf{r}}\cdot\mathbf{s}/a_0)\mathrm{d}^3\mathbf{s}\mathrm{d}^3\mathbf{x}. \tag{4.2}$$

The contribution from the enthalpy term is computed analogously:

$$\overline{(p^h)^2}(\mathbf{r}) = \frac{1}{16\pi^2 a_0^2 r^2} \frac{\partial^4}{\partial t^4} \iint R_r^h(\mathbf{x};\mathbf{s};\hat{\mathbf{r}}\cdot\mathbf{s}/a_0)\mathrm{d}^3\mathbf{s}\,\mathrm{d}^3\mathbf{x}. \tag{4.3}$$

Effects of space separation and differences in retarded time on the space–time correlations are neglected from Eqs. (4.2) and (4.3). So the contribution from the momentum and enthalpy terms are:

$$\overline{(p^m)^2}(\mathbf{r}) \sim \frac{1}{16\pi^2 a_0^4 r^2} \frac{\partial^4}{\partial t^4} \int R_r^m(\mathbf{x};0;0) \int \mathrm{d}^3\mathbf{s}\mathrm{d}^3\mathbf{x}, \tag{4.4}$$

and

$$\overline{(p^h)^2}(\mathbf{r}) \sim \frac{1}{16\pi^2 a_0^2 r^2} \frac{\partial^4}{\partial t^4} \int R_r^h(\mathbf{x};0;0) \int \mathrm{d}^3\mathbf{s}\,\mathrm{d}^3\mathbf{x}. \tag{4.5}$$

A dimension for the fourth-order time derivative and volume integral with space separation must be introduced. The time derivative and volume integral are related to the scales of time (τ_0) and of length (ℓ) by:

$$\frac{\partial^4}{\partial t^4} \sim \tau_0^{-4}, \tag{4.6}$$

and

$$\int \mathrm{d}^3\mathbf{s} \sim \ell^3. \tag{4.7}$$

With these scales for time and length, Eqs. (4.4) and (4.5) are written as

$$\overline{(p^m)^2}(r) \sim \frac{1}{a_0^4 r^2} \int R_r^m(\mathbf{x};0;0)\,\tau_0^{-4}(\mathbf{x})\ell^3(\mathbf{x})\mathrm{d}^3\mathbf{x}, \tag{4.8}$$

$$\overline{(p^h)^2}(r) \sim \frac{1}{a_0^2 r^2} \int R_r^h(\mathbf{x};0;0)\,\tau_0^{-4}(\mathbf{x})\,\ell^3(\mathbf{x})\,\mathrm{d}^3\mathbf{x}, \tag{4.9}$$

in which the time and length scales may vary with location in the jet. The directivity of the farfield is ignored, so the location of the observer is written in terms of the distance to the nozzle exit only, $r \equiv |\mathbf{r}|$, instead of $\mathbf{r}$.

The space-time correlation of the source terms with zero separation gives the strength of the source terms. Assuming that the velocity, density and enthalpy fluctuations are uncorrelated (see confirmation of the assumption with LES data in Fig. 6.7, the strength of the momentum and enthalpy source terms are

$$R_r^m(\mathbf{x};0;0) \sim \overline{\rho^2}(\mathbf{x})\overline{(U_r^2)^2}(\mathbf{x}), \tag{4.10}$$

$$R_r^h(\mathbf{x};0;0) \sim \overline{\rho^2}(\mathbf{x})\overline{U_r^2}(\mathbf{x}) \left[\overline{h^2}(\mathbf{x})/h_0 - 1\right]. \tag{4.11}$$

The thermodynamic variables are now decomposed into mean and fluctuation components,

$$\rho = \overline{\rho} + \rho', \tag{4.12}$$

$$h = \overline{h} + h'. \tag{4.13}$$

The mean square of these properties give the strength of the sources (Eqs. (4.11) and (4.11). Assuming that the fluctuations are small, i.e. $\overline{(\rho')^2} \ll (\overline{\rho})^2$ and $\overline{(h')^2} \ll (\overline{h})^2$, the mean square of density and enthalpy are

$$\overline{\rho^2} = (\overline{\rho})^2 + \overline{(\rho')^2} \approx (\overline{\rho})^2, \tag{4.14}$$

$$\overline{h^2} = \left(\overline{h}\right)^2 + \overline{(h')^2} \approx \left(\overline{h}\right)^2. \tag{4.15}$$

The approximate value for the mean square of the thermodynamic variables (Eqs. (4.14) and (4.15)) are used in the equations for the source strength (Eqs. (4.10) and (4.11),) so the strength of the sources are:

$$R_r^m(\mathbf{x};0;0) \sim \overline{\rho}^2(\mathbf{x})\overline{(U_r^2)^2}(\mathbf{x}), \tag{4.16}$$

and

$$R_r^h(\mathbf{x};0;0) \sim \overline{\rho}^2(\mathbf{x})\overline{U_r^2}(\mathbf{x})\left[\overline{h}^2(\mathbf{x})/h_0 - 1\right]. \tag{4.17}$$

The strength of the source terms (Eqs. (4.16) and (4.17)) are substituted in Eqs. (4.8) and (4.9) to yield the contribution from the momentum and enthalpy sources to the farfield mean square pressure as:

$$\overline{(p^m)^2}(r) \sim \frac{1}{a_0^4 r^2}\int \overline{\rho^2}(\mathbf{x})\overline{(U_r^2)^2}(\mathbf{x})\tau_0^{-4}(\mathbf{x})\ell^3(\mathbf{x})\mathrm{d}^3\mathbf{x}, \tag{4.18}$$

and

$$\overline{(p^h)^2}(r) \sim \frac{1}{a_0^2 r^2}\int \overline{\rho}^2(\mathbf{x})\left[\overline{h}(\mathbf{x})/h_0 - 1\right]^2\overline{U_r^2}(\mathbf{x})\tau_0^{-4}(\mathbf{x})\ell^3(\mathbf{x})\,\mathrm{d}^3\mathbf{x}. \tag{4.19}$$

Equations (4.18) and (4.19) relate the strength of the farfield pressure to the turbulence in the jet plume. Two scaling laws are presented in the next two sections by providing explicit relations between the scales in Eqs. (4.18) and (4.19) and properties of the jet. Section 4.1.1 presents a formulation that uses nozzle-exit properties to provide the scales for the scaling law, whereas Section 4.1.2 presents a formulation that uses local information about the flow computed from a RANS k–ε simulation.

4.1.1 Scales based on nozzle-exit variables

The dimensions of the integrand in Eqs. (4.18) and (4.19) may be computed from the nominal nozzle-exit variables. As considered by Lighthill [7], the nozzle diameter, D_J, is used for the length scale and the nozzle-exit velocity, U_J, as a velocity scale. So the scales of length, time, and the volume integral over the jet plume are related to these scales by:

$$\ell \sim D_J, \tag{4.20}$$

$$\tau_0 \sim D_J/U_J, \tag{4.21}$$

and

$$\int \mathrm{d}^3\mathbf{x} \sim D_J^3. \tag{4.22}$$

With these scales of length, time, and velocity the volume integral over the jet plume in Eqs. (4.18) and (4.19) may be written as:

$$\overline{(p^m)^2}(r) \sim \frac{D_J^2}{a_0^4 r^2}\overline{\rho}^2\overline{(U_r^2)^2}(\mathbf{x})U_J^4, \tag{4.23}$$

$$\overline{(p^h)^2}(r) \sim \frac{D_J^2}{a_0^2 r^2}\overline{\rho}^2\left[\overline{h}/h_0 - 1\right]^2\overline{U_r^2}(\mathbf{x})U_J^4. \tag{4.24}$$

The mean square value of the squared velocity and of the velocity are related to the nozzle-exit velocity, respectively, by

$$\overline{(U_r^2)^2} \sim U_J^4, \tag{4.25}$$

and

$$\overline{U_r^2} \sim U_J^2. \tag{4.26}$$

Using these scales for the mean square of velocity in Eqs. (4.23) and (4.24) yields

$$\overline{(p^m)^2}(r) \sim \frac{D_J^2}{a_0^4 r^2}\overline{\rho}^2 U_J^8, \tag{4.27}$$

$$\overline{(p^h)^2}(r) \sim \frac{D_J^2}{a_0^2 r^2}\overline{\rho}^2\left[\overline{h}/h_0 - 1\right]^2 U_J^6. \tag{4.28}$$

Scales for the thermodynamic variables are also introduced. The density and enthalpy may be related to their nominal nozzle-exit values as

$$\overline{\rho} \sim \rho_J, \tag{4.29}$$

and

$$\overline{h}/h_0 \sim h_J/h_0. \tag{4.30}$$

It is more convenient, however, to relate both properties to the nozzle-exit temperature, T_J, using an equation of state.

Using the equation of state for an ideal gas, the nozzle-exit density may be written as

$$\rho_J = p_0/\mathrm{R}T_J, \tag{4.31}$$

for which the nozzle-exit pressure is equal to the ambient pressure, p_0, and R is the gas constant.

It is assumed that the ratio of specific heats is constant, so enthalpy differences are related to temperature differences by

$$h_J - h_0 = c_p(T_J - T_0), \tag{4.32}$$

in which c_p is the specific heat at constant pressure, and h_0 and T_0 are the ambient values of enthalpy and temperature. The ambient enthalpy is related to the ambient temperature by

$$h_0 = c_p T_0. \tag{4.33}$$

The scaling for the density and enthalpy in terms of temperature may now be written as:

$$\overline{\rho}^2 \sim (p_0/\mathrm{R}T_J)^2 \tag{4.34}$$

$$\left(\overline{h}/h_0 - 1\right)^2 \sim (T_R - 1)^2, \tag{4.35}$$

in which $T_R = T_J/T_0$ is the nozzle-exit temperature ratio.

Using the relationship between the density and enthalpy with the nozzle-exit temperature (Eqs. (4.34) and (4.35)), the contribution from the momentum and enthalpy terms to the acoustic farfield (Eqs. (4.27) and (4.28)) may be written as

$$\overline{(p^m)^2}(r) \sim \frac{D_J^2 p_0^2}{\mathrm{R}^2 a_0^4 r^2} \frac{1}{T_J^2} U_J^8, \tag{4.36}$$

and

$$\overline{(p^h)^2}(r) \sim \frac{D_J^2 p_0^2}{\mathrm{R}^2 a_0^2 r^2 T_J^2} (T_R - 1)^2 U_J^6. \tag{4.37}$$

The mean square pressure in the farfield is computed by summing the contributions from the momentum and enthalpy sources. Assuming that the contributions are uncorrelated, the scaling of the farfield mean square pressure with nozzle-exit values is given by summing Eqs. (4.36) and (4.37), which results in

$$\overline{p^2}_{\mathrm{NE}} \sim \frac{D_J^2 p_0^2}{\mathrm{R}^2 a_0^4 r^2} \frac{1}{T_J^2} \left[\alpha_M U_J^8 + \alpha_H \left(T_R - 1\right)^2 a_0^2 U_J^6 \right], \tag{4.38}$$

in which α_M and α_H adjust the relative contribution of the approximate terms.

The dimensional analysis shows that the momentum source scales with the eighth power of the jet-exit velocity, the same scaling derived by Lighthill [7], and that the enthalpy source scales with to the sixth power of velocity, which agrees with Morfey [17] and Morfey, Szewczyk, and Tester [48]. Both sources increase with a power of velocity, but have different scaling with temperature. The momentum source is inversely proportional to the temperature by T_J^{-2}, whereas the enthalpy source scales increases with $(T_R - 1)^2/T_J^2$—the scaling with temperature is different from the one by Morfey [17], as herein the effect of changes in mean density is accounted for in the momentum term.

The differences in scaling of the momentum and enthalpy sources explain why at low speed hot jets are noisier than isothermal jets, whereas at high speed hot jets are quieter than isothermal jets. For the high-speed jets the momentum term starts to dominate, so its reduction with T_J^{-2} result in an overall reduction of noise if temperature is increased. For low-speed jets, the enthalpy source dominates above certain jet temperature, so the overall noise increases with temperature.

4.1.2 Scales from RANS k–ε

In this section, the scales needed by the dimensional analysis of the farfield mean square pressure (Eqs. (4.18) and (4.9)) are computed from local information of turbulence in the jet plume. This derivation is similar to the one for the scaling with nozzle-exit values (Section 4.1.1), but the mean properties and turbulence scales are related to local information gathered from a RANS k–ε solution of the flow.

The mean square of velocity squared and velocity are related to the turbulent kinetic energy (k) via

$$\overline{(U_r^2)^2}(\mathbf{x}) \sim k^2(\mathbf{x}), \tag{4.39}$$

$$\overline{U_r^2}(\mathbf{x}) \sim k(\mathbf{x}). \tag{4.40}$$

The length and time scales are related to the traditional RANS scales by:

$$\ell(\mathbf{x}) \sim \frac{k^{3/2}(\mathbf{x})}{\varepsilon(\mathbf{x})}, \tag{4.41}$$

and

$$\tau_0(\mathbf{x}) \sim \frac{k(\mathbf{x})}{\varepsilon(\mathbf{x})}. \tag{4.42}$$

With the proposed relations for the scales of magnitude, time and length (Eqs. (4.39)–(4.42)), the contributions from the momentum and enthalpy term are given, respectively, by:

$$\overline{(p^m)^2}(r) \sim \frac{1}{a_0^4 r^2} \int \overline{\rho}^2 k^{5/2} \varepsilon \mathrm{d}^3\mathbf{x}, \tag{4.43}$$

and

$$\overline{(p^h)^2}(r) \sim \frac{1}{a_0^2 r^2} \int \overline{\rho}^2 \left(\overline{h}/h_0 - 1\right)^2 k^{3/2} \varepsilon \mathrm{d}^3\mathbf{x}, \tag{4.44}$$

in which all terms in the integrand except h_0 vary with $\mathbf{x}$. It is assumed that the thermodynamic variables have small fluctuations and are not correlated to velocity fluctuations (see Eqs. (4.14) and (4.15)), so their local mean values are used.

The contribution of the momentum and enthalpy terms are summed to yield the scaling of the farfield mean square pressure with the RANS solution as

$$\overline{p^2}_{\mathrm{RANS}}(r) \sim \frac{1}{a_0^4 r^2} \int \overline{\rho}^2 k^{3/2} \varepsilon \left[\alpha_M k + \alpha_M a_0^2 \left(\overline{h}/h_0 - 1\right)^2\right] \mathrm{d}^3\mathbf{x}, \tag{4.45}$$

in which α_M and α_H adjust the relative contribution from the momentum and from the enthalpy terms.

4.1.3 Based on the Lilley–Goldstein analogy

The scaling laws presented in Sections 4.1.1 and 4.1.2 are based on the formulation presented in Chapter 2. In this section, a scaling law based on the acoustic analogy by Lilley–Goldstein [9, 16] is presented. The Lilley–Goldstein formulation is first presented for a parallel shear flow, then the base flow is considered homogeneous and at rest to derive the scaling law that. The resulting scaling law is then compared to the one presented in Chapter 2.

Goldstein [16] introduced an acoustic analogy based on the one presented by Lilley [9]; i.e. the equations of fluid motion (continuity, momentum, and energy) are manipulated so to write a third-order inhomogeneous wave equation. The wave equation is written for a parallel shear flow as a base flow, thus having the Pridmore-Brown operator [49] acting on the choice of acoustic independent variable.

The main difference between Goldstein's formulation and the one by Lilley [9] is the choice of independent variables and the resulting form of the source terms.

Goldstein [16] defines the modified pressure as

$$\pi \equiv \left(\frac{p}{p_0}\right)^{1/\kappa} - 1. \tag{4.46}$$

With this modified pressure and assuming a parallel shear flow as the base flow, the equations of continuity, momentum, and energy can be combined in the form

$$\overline{L}_0 \pi = \frac{\mathrm{D}_0}{\mathrm{D}t}\frac{\partial f_i}{\partial x_i} - 2\frac{\partial \overline{U}_1}{\partial x_j}\frac{\partial f_j}{\partial x_1}, \tag{4.47}$$

in which $\overline{L}_0$ is the Pridmore-Brown operator [49],

$$\overline{L}_0 \equiv \frac{\mathrm{D}_0}{\mathrm{D}t}\left(\frac{\mathrm{D}_0^2}{\mathrm{D}t^2} - \frac{\partial}{\partial x_i}\overline{a^2}\frac{\partial}{\partial x_i}\right) + 2\frac{\partial \overline{U}_1}{\partial x_i}\frac{\partial}{\partial x_1}\overline{a^2}\frac{\partial}{\partial x_i}; \tag{4.48}$$

$\mathrm{D}_0/\mathrm{D}t$ is the convective derivative with the mean flow as a parallel shear flow,

$$\frac{\mathrm{D}_0}{\mathrm{D}t} \equiv \frac{\partial}{\partial t} + \overline{U}_1\frac{\partial}{\partial x_1}; \tag{4.49}$$

and f_i is the source vector that combines a quadrupole and a dipole source terms,

$$f_i = -\frac{\partial}{\partial x_j}(1+\pi)\,u_i u_j - \left(a^2\right)'\frac{\partial \pi}{\partial x_i}. \tag{4.50}$$

To make a comparison with the formulation of Section 2.1, the Lilley-Goldstein analogy (4.47) is rewritten for a homogeneous base flow at rest. For such a mean base flow, the mean axial velocity is zero, i.e. $\overline{U}_1 = 0$, so that $\partial \overline{U}_1/\partial x_i = 0$ and $\mathrm{D}_0/\mathrm{D}t = \partial/\partial t$. Additionally, the mean sound speed is the ambient sound speed, i.e. $\overline{a^2} = a_0^2$. Equation (4.47) is thus written as

$$\frac{\partial^2 \pi}{\partial t^2} - a_0^2 \nabla^2 \pi = \frac{\partial f_i}{\partial x_i}. \tag{4.51}$$

The modified Lilley–Goldstein analogy in Eq. (4.51) neglects the acoustic–mean flow effects described by the Pridmore-Brown operator in the left hand side of Eq. (4.47) and the effects of source convection in the right hand side of Eq. (4.47). The source vector f_i, however, is not changed as it contains only fluctuations of turbulent properties, not mean properties of the base flow.

For small amplitude acoustic perturbations, the modified pressure is approximated as $\pi \approx p'/p_0\kappa_0$ [16], so Eq. (4.51) may be written as

$$\frac{1}{p_0\kappa_0}\left(\frac{\partial^2 p'}{\partial t^2} - a_0^2\nabla^2 p'\right) = \frac{\partial f_i}{\partial x_i}. \tag{4.52}$$

Assuming the fluid an ideal gas with constant ratio of specific heat (so that $a_0^2 = \kappa_0 p_0/\rho_0$) and dividing by a_0^2, Eq. (4.52) is written as

$$\frac{1}{a_0^2}\frac{\partial^2 p'}{\partial t^2} - \nabla^2 p' = \rho_0 \frac{\partial f_i}{\partial x_i}. \tag{4.53}$$

Scaling laws for the contribution from the velocity-quadrupole and temperature-dipole to the far-field mean square pressure are now introduced. The effect the different multipolar nature of the sources becomes evident. By assuming D_J/U_J a typical time scale, the contribution to the mean square pressure from the quadrupole and

dipole sources are multiplied, respectively, by $(U_J/D_J a_0)^4$ and $(U_J/D_J a_0)^2$ due to the multipolar nature of the sources (see Morfey [17]).

The scaling laws for the strength of the quadrupole and dipole sources described in Eq. (4.50)—$(1+\pi)u_i u_j$ and $(a^2)'\partial\pi/\partial x_i$, respectively—are introduced. The quadrupole source combines the contribution from the term $u_i u_j$ which is second order on turtubulent fluctuations, and $\pi u_i u_j$ which is third-order on turbulent fluctuations. It is assumed that the second-order term dominates, so that the scaling law for the strength of the so-called velocity-quadrupole is given by

$$u_i u_j \sim U_J^2. \tag{4.54}$$

For the scaling law of the dipole source, the gradient is related to a typical length scale taken as the nozzle-diameter, $\partial/\partial x_i \sim D_J$. The fluctuation of sound speed is related to the difference between the jet-exit temperature and the ambient temperature, $(a^2)' \sim T_J - T_0$. The modified pressure is related to the pressure fluctuations in the source region, i.e. $\pi \sim p'/p_0\kappa_0$. And the pressure fluctuations are related to a typical density in the source region (ρ_s) and a velocity scale (here taken as the nozzle-exit velocity, U_J), i.e. $p' \sim \rho_s U_J^2$ (as in Refs. [17, 50]). Then, the scaling law for the strength of the so-called temperature-dipole is written as

$$\left(a^2\right)' \frac{\partial \pi}{\partial x_i} \sim \frac{1}{D_J}\frac{T_J - T_0}{T_J} U_J^2, \tag{4.55}$$

in which the density in the source region was assumed to scale as ρ_J (hence the $1/T_J$ factor).

Using the relations presented in the previous paragraphs, and taking $\rho_0 \sim 1/T_0$, the scaling laws for the contribution from the velocity-quadrupole and the temperature-dipole to the far-field mean square pressure are

$$\begin{aligned} \overline{(p^q)^2} &\sim \frac{D_J^2}{r^2 a_0^4 T_0^2} U_J^8, \\ \overline{(p^d)^2} &\sim \frac{D_J^2}{r^2 a_0^2 T_0^2}\left(\frac{T_J - T_0}{T_J}\right)^2 U_J^6. \end{aligned} \tag{4.56}$$

in which r is a characteristic distance to the farfield observer. Note that the integral form of Eq. (4.53), written using the free-field Green's function, results in the additional factor of D_J^6/r^2 for the scaling of the contribution from each source term to the farfield mean square pressure.

Comparison of scaling laws

The contribution from the quadrupole and dipole sources based on the acoustic analogy described in Section 2.1 and on the formulation by Lilley–Goldstein modified for a homogeneous base flow at rest are presented in the following table:

$$\begin{aligned}
\text{(Section 2.1) quadrupole} \quad & \sim \frac{1}{a_0^4 T_J^2} U_J^8 \\
\text{(Section 2.1) dipole} \quad & \sim \frac{1}{a_0^2 T_0^2} \left(\frac{T_J - T_0}{T_J} \right)^2 U_J^6 \\
\text{(Lilley–Goldstein-based) quadrupole} \quad & \sim \frac{1}{a_0^4 T_0^2} U_J^8 \\
\text{(Lilley–Goldstein-based) dipole} \quad & \sim \frac{1}{a_0^2 T_0^2} \left(\frac{T_J - T_0}{T_J} \right)^2 U_J^6
\end{aligned}$$

The quadrupole of Section 2.1 is different from the quadrupole source based on the Lilley–Goldstein analogy written for a homogeneous base flow at rest. The formulation of Section 2.1 keeps the mean density in the quadrupole source, so the scaling law results in a dependence with the nozzle-exit temperature. The scaling law based on the Lilley–Goldstein analogy moves the density from the quadrupole source to the acoustic operator; so when writing the formulation for a homogeneous flow, there is a dependence with the ambient density (hence ambient temperature).

Conversely, the scaling law for the dipole from Section 2.1 and from the one based on the Lilley–Goldstein-based formulation are the same. Both are related to $1/T_0^2$, which results from the mean density in the acoustic operator that is set to the ambient density when assuming a homogeneous base flow. There is also a dependence with $1/T_J^2$ in the scaling law, due to the density in the source region that gives the strength of the turbulent fluctuations in the dipole source.

4.2 Formulation to predict the farfield autospectral density

The formulation to predict the farfield autospectrum applies the no-flow acoustic analogy derived in Section 2.1. The derivation in this section starts with the equations for the contribution from the momentum and the enthalpy sources to the farfield autospectral density (Eqs. (2.40) and Eqs. (2.41)), and applies simplifications regarding the turbulence in the jet.

4.2.1 Neglect of shear noise term

In the no-flow acoustic analogy, the momentum and enthalpy sources are related to the instantaneous velocity. If the velocity is decomposed into mean and fluctuating components, the sources may be decomposed into a component with only the fluctuating velocity and another with the mean velocity. For the momentum term, the decomposition results in the shear and self noise source terms of Ribner [51]:

$$q_{\text{shear}}(\mathbf{x},t) = \overline{U}_r(\mathbf{x})u_r(\mathbf{x},t) \tag{4.57}$$

and

$$q_{\text{self}}(\mathbf{x},t) = u_r^2(\mathbf{x},t). \tag{4.58}$$

In the formulation by Goldstein [27] as applied by Karabasov et al. [42] the momentum source is related only to the fluctuating velocity component. The mean velocity is moved to the acoustic operator and is related only to effects of flow–acoustic interaction.

By comparison with Goldstein's acoustic analogy, the shear noise sources are ignored so the momentum and enthalpy terms are simplified to

$$q_i^m(\mathbf{x},t) = \rho(\mathbf{x},t)u_i^2(\mathbf{x},t). \tag{4.59}$$

and

$$q_i^h(\mathbf{x},t) = \rho(\mathbf{x},t)\,[h(\mathbf{x},t)/h_0 - 1]\,u_i(\mathbf{x},t). \tag{4.60}$$

4.2.2 Neglect of thermodynamic fluctuations

Some simplifications of the source term were introduced for the scaling law in Section 4.1. The simplifications discarded fluctuations of thermodynamic variables from the momentum and enthalpy source terms. In this section these simplifications are analysed in more detail, so that the errors caused by the simplification can be computed.

Momentum term

It is usual to discard the fluctuations of density from the momentum term for isothermal jets. This simplification is analysed by decomposing the density into mean and fluctuating components and writing the mean square value of the momentum source term.

After decomposing the density into a mean and fluctuating value ($\rho = \overline{\rho} + \rho'$), the mean square of the momentum term may be written as:

$$\overline{(\rho u_i^2)^2} = \overline{\rho}^2\overline{(u_i^2)^2} + \overline{(\rho' u_i^2)^2} + 2\overline{\rho}\overline{\rho'(u_i^2)^2}. \tag{4.61}$$

It is assumed that the density fluctuations and squared velocity fluctuations are uncorrelated, so the terms $\overline{(\rho' u_i^2)^2}$ and $2\overline{\rho}\overline{\rho'(u_i^2)^2}$ are neglected.

So the mean square value of the momentum source term may be written as

$$\overline{(\rho u_i^2)^2} \approx \overline{\rho}^2\overline{(u_i^2)^2}. \tag{4.62}$$

It is inferred that the analysis for the mean square value is also valid for the instantaneous source term. So the simplified momentum term is then written as

$$q_i^m(\mathbf{x},t) = \overline{\rho}(\mathbf{x})u_i^2(\mathbf{x},t). \tag{4.63}$$

This simplification can also be understood as neglecting effects of compressibility in the momentum source term. In general, these effects are significant for high Mach numbers (say, > 0.3). This is the case for the mean velocity field in the transonic jets studied in this thesis. However, the source term is related to velocity fluctuations. Velocity fluctuations in jets peak at around a fifth of the jet exit velocity, so for subsonic jets the Mach number related to velocity fluctuations is invariably smaller than 0.3.

Enthalpy term

The simplification of the enthalpy term is analogous to the simplification of the momentum term: thermodynamic fluctuations are neglected from the source term. This seems counter-intuitive, given that the source term is related to enthalpy. But the source is related to fluctuations of enthalpy fluxes, not to fluctuations of enthalpy. So neglecting thermodynamic fluctuations is equivalent to assuming that the velocity fluctuations amounts to most of the fluctuations in the enthalpy flux.

With the assumption that density and enthalpy fluctuations are negligible from the fluctuation of enthalpy flux, the enthalpy term is written as

$$q_i^h(\mathbf{x},t) = u_i(\mathbf{x},t)\overline{\rho}(\mathbf{x})\left[\overline{h}(\mathbf{x})/h_0 - 1\right], \tag{4.64}$$

in which $\overline{h}(\mathbf{x})$ is the mean local enthalpy.

Application of simplifications in the source model

With the neglect of density and enthalpy fluctuations from the momentum and enthalpy source terms, their space–time correlation are written as

$$R_r^m(\mathbf{x};\mathbf{s};\tau) = \overline{\rho}^2(\mathbf{x}) R_{rrrr}(\mathbf{x};\mathbf{s};\tau), \tag{4.65}$$

and

$$R_r^h(\mathbf{x};\mathbf{s};\tau) = \overline{\rho}^2(\mathbf{x}) \left[\overline{h}(\mathbf{x})/h_0 - 1\right]^2 R_{rr}(\mathbf{x};\mathbf{s};\tau), \tag{4.66}$$

in which R_{rrrr} is the space-time correlation of u_r^2 and R_{rr} is the space-time correlation of u_r.

The space–time correlation of the simplified source terms are used in Eqs. (2.40) and Eqs. (2.41) to rewrite the contribution from the momentum and enthalpy source to the farfield autospectral density as:

$$S_{pp}^m(\mathbf{r};\omega) = \frac{\omega^4}{16\pi^2 a_0^4 r^2} \int \overline{\rho}^2(\mathbf{x}) \int \mathscr{F}\left[R_{rrrr}(\mathbf{x};\mathbf{s};\tau)\right] \exp\left(i\frac{\omega}{a_0}\hat{\mathbf{r}}\cdot\mathbf{s}\right) \mathrm{d}^3\mathbf{s}\mathrm{d}^3\mathbf{x}. \tag{4.67}$$

and

$$\begin{aligned} S_{pp}^h(\mathbf{r};\omega) = \frac{\omega^4}{16\pi^2 a_0^2 r^2} &\int \overline{\rho}^2(\mathbf{x}) \left[\overline{h}(\mathbf{x})/h_0 - 1\right]^2 \\ &\times \int \mathscr{F}\left[R_{rr}(\mathbf{x};\mathbf{s};\tau)\right] \exp\left(i\frac{\omega}{a_0}\hat{\mathbf{r}}\cdot\mathbf{s}\right) \mathrm{d}^3\mathbf{s}\mathrm{d}^3\mathbf{x}. \end{aligned} \tag{4.68}$$

4.2.3 Assumption of compact and isotropic sources

The no-flow acoustic analogy accounts for the differences of time emission within the jet plume. After integration with space separation, these differences lead to interference between locations that are within a coherent volume of turbulence. Albeit implicitly, Ilário et al. [10] neglected these effects of interference, which is the same as assuming the sources compact.

On the assumption of compact sources, the factor related to retarded time differences, $\exp(i\omega\hat{\mathbf{r}}\cdot\mathbf{s}/a_0)$, is neglected. So the equations for the farfield autospectral density (Eqs. (4.67) and (4.68)) are rewritten as

$$S_{pp}^{m}(\mathbf{r};\omega) = \frac{\omega^4}{16\pi^2 a_0^4 r^2}\int \overline{\rho}^2(\mathbf{x})\int \mathscr{F}\left[R_{rrrr}(\mathbf{x};\mathbf{s};\tau)\right]\mathrm{d}^3\mathbf{s}\mathrm{d}^3\mathbf{x}. \tag{4.69}$$

and

$$S_{pp}^{h}(\mathbf{r};\omega) = \frac{\omega^4}{16\pi^2 a_0^2 r^2}\int \overline{\rho}^2(\mathbf{x})\left[\overline{h}(\mathbf{x})/h_0 - 1\right]^2\int \mathscr{F}\left[R_{rr}(\mathbf{x};\mathbf{s};\tau)\right]\mathrm{d}^3\mathbf{s}\mathrm{d}^3\mathbf{x}. \tag{4.70}$$

The sources of noise are also considered isotropic. The assumption of isotropic turbulence restricts the application of the formulation to an observer at the angle with which the method is calibrated. As in this thesis the method is calibrated with farfield measurements at $\theta = 90^\circ$, the correlations are related to the radial component of velocity. The dependence with $\mathbf{r}$ is thus simplified to a dependence only with the distance to the observer, $r \equiv |\mathbf{r}|$. So the equations for the farfield spectrum are written explicitly in terms of the correlation of the squared radial velocity, R_{2222} and R_{22}, instead of more general R_{rrrr} and R_{rr}.

The contribution from the momentum and enthalpy sources to the farfield autospectral density are:

$$S_{pp}^{m}(r;\omega) = \frac{\omega^4}{16\pi^2 a_0^4 r^2}\int \overline{\rho}^2(\mathbf{x})\int \mathscr{F}\left[R_{2222}(\mathbf{x};\mathbf{s};\tau)\right]\mathrm{d}^3\mathbf{s}\mathrm{d}^3\mathbf{x}. \tag{4.71}$$

and

$$S_{pp}^{h}(r;\omega) = \frac{\omega^4}{16\pi^2 a_0^2 r^2}\int \overline{\rho}^2(\mathbf{x})\left[\overline{h}(\mathbf{x})/h_0 - 1\right]^2\int \mathscr{F}\left[R_{22}(\mathbf{x};\mathbf{s};\tau)\right]\mathrm{d}^3\mathbf{s}\mathrm{d}^3\mathbf{x}. \tag{4.72}$$

4.2.4 Empirical model for space–time correlation

An empirical model for the space–time correlation of u_2^2 and u_2 (R_{2222} and R_{22}) is introduced to compute the farfield spectrum. The model assumes locally-homogeneous and isotropic turbulence, so that the theoretical analysis of correlation by Batchelor

[24] is applied. The space–time correlation is assumed separable in time and space, and a Gaussian decay is considered for space and time separations.

Considering a Gaussian decay for both time and separation, the space–time correlation of u_2 is

$$R_{22}(\mathbf{x};\mathbf{s};\tau) = \sigma_{22}(\mathbf{x}) \exp\left(-\frac{|\mathbf{s}|^2}{\ell_h^2(\mathbf{x})}\right) \exp\left(-\frac{\tau^2}{\tau_{0,h}^2(\mathbf{x})}\right), \tag{4.73}$$

in which $\sigma_{22}(\mathbf{x}) = R_{22}(\mathbf{x};0;0)$, ℓ_h is the length scale for the enthalpy source term, and $\tau_{0,h}$ is the time scale for the enthalpy source term. The dependence of the correlation with location in the jet is via $R_{22}(\mathbf{x};0;0)$ (the mean square value of u_2), and the scales of length and time.

The correlation for u_2^2 is related to the correlation for u_2 via the theory of homogeneous turbulence as done by Khavaran, Krejsa and Kim [8] (see the theory in Batchelor [24]):

$$R_{2222}(\mathbf{x};\mathbf{s};\tau) = \sigma_{22}(\mathbf{x})\sigma_{22}(\mathbf{x}+\mathbf{s}) + 2R_{22}(\mathbf{x},\mathbf{s},\tau)^2. \tag{4.74}$$

In the source model a time derivative is taken of the correlation. Since the term on σ_{22} is constant with time for stationary turbulence, it can be neglected. The correlation of u_r^2 is then written as:

$$R_{2222}(\mathbf{x},\mathbf{s},\tau) = 2\sigma_{22}^2(\mathbf{x}) \exp\left(-2\frac{|\mathbf{s}|^2}{\ell_m^2(\mathbf{x})}\right) \exp\left(-2\frac{\tau^2}{\tau_{0,m}^2(\mathbf{x})}\right), \tag{4.75}$$

in which ℓ_m and $\tau_{0,m}$ are the length and time scales for the momentum source term.

The models for the space–time correlation are used in Eqs. (4.71) and (4.72) to write the contribution from the momentum and enthalpy sources to the farfield autospectral density as:

$$S_{pp}^m(r;\omega) = \frac{\omega^4}{8\pi^2 a_0^4 r^2} \int \overline{\rho}^2 \sigma_{22}^2 \mathscr{F}\left[\exp\left(-2\frac{\tau^2}{\tau_{0,m}^2}\right)\right] \int \exp\left(-2\frac{|\mathbf{s}|^2}{\ell_m^2}\right) \mathrm{d}^3\mathbf{s}\mathrm{d}^3\mathbf{x}, \tag{4.76}$$

and

$$S_{pp}^{h}(r;\omega) = \frac{\omega^4}{16\pi^2 a_0^2 r^2} \int \overline{\rho}^2 \left(\overline{h}/h_0 - 1\right)^2 \sigma_{22} \mathscr{F}\left[\exp\left(-\frac{\tau^2}{\tau_{0,h}^2}\right)\right] \times \int \exp\left(-\frac{|\mathbf{s}|^2}{\ell_h^2}\right) \mathrm{d}^3\mathbf{s}\mathrm{d}^3\mathbf{x}, \tag{4.77}$$

in which the variables in the integrand—except h_0, τ, and $|\mathbf{s}|$—vary with $\mathbf{x}$.

The Gaussian function used in the correlation model is convenient because analytical integrals are available. So the Fourier transform and volume integral with space separation can be computed analytically.

The Fourier transforms of the temporal part of R_{2222} and R_{22} are, respectively,

$$\mathscr{F}\left[\exp\left(-2\frac{\tau^2}{\tau_{0,m}^2(\mathbf{x})}\right)\right] = \frac{\sqrt{\pi}}{2}\tau_{0,m}(\mathbf{x}) \exp\left(-\frac{\omega^2\tau_{0,m}^2}{8}\right), \tag{4.78}$$

and

$$\mathscr{F}\left[\exp\left(-\frac{\tau^2}{\tau_{0,h}^2(\mathbf{x})}\right)\right] = \sqrt{\pi}\tau_{0,h}(\mathbf{x}) \exp\left(-\frac{\omega^2\tau_{0,h}^2}{4}\right). \tag{4.79}$$

The volume integral with space separation in Eqs. (4.76) and (4.77) are, respectively,

$$\int_{-\infty}^{+\infty} \exp\left(-2\frac{|\mathbf{s}|^2}{\ell_m^2(\mathbf{x})}\right) \mathrm{d}^3\mathbf{s} = \frac{\pi^{3/2}}{8\sqrt{2}}\ell_m^3(\mathbf{x}), \tag{4.80}$$

$$\int_{-\infty}^{+\infty} \exp\left(-\frac{|\mathbf{s}|^2}{\ell_h^2(\mathbf{x})}\right) \mathrm{d}^3\mathbf{s} = \frac{\pi^{3/2}}{4}\ell_h^3(\mathbf{x}). \tag{4.81}$$

The results of the Fourier transforms and volume integral in space separation are used in the equations for the farfield spectrum to yield

$$S_{pp}^{m}(r;\omega) = \frac{\omega^4}{128 a_0^4 r^2} \int \overline{\rho}^2 \sigma_{22}^2 \ell_m^3 \tau_{0,m} \exp\left(-\frac{\omega^2\tau_{0,m}^2}{8}\right) \mathrm{d}^3\mathbf{x}. \tag{4.82}$$

and

$$S_{pp}^{h}(r;\omega) = \frac{\omega^4}{64 a_0^2 r^2} \int \overline{\rho}^2 \left[\overline{h}/h_0 - 1\right]^2 \sigma_{22} \ell_h^3 \tau_{0,h} \exp\left(-\frac{\omega^2 \tau_{0,h}^2}{4}\right) \mathrm{d}^3\mathbf{x}, \tag{4.83}$$

in which the variables in the integrand—except h_0 and ω—vary with $\mathbf{x}$.

To derive Eqs. (4.82) and (4.83) the no-flow acoustic analogy was applied, the turbulence was assumed isotropic and the sources were assumed compact, and a model for space–time correlations of velocity was introduced. In Section 4.2.5 the formulation is related to the solution of the mean flow in order to present the last step of the derivation.

4.2.5 Relationship with RANS k–ε data

The RANS solution is used to gather information about the mean flow and about turbulence scales in the jet plume. The mean flow properties are given directly by the RANS solution. The turbulence scales are computed by combining turbulent kinetic energy and the turbulence dissipation rate.

Three turbulence scales are needed by the source model. A scale of magnitude, which gives the overall strength of the sources. A time scale, which gives the lifespan of the turbulent eddies and is related to the characteristic frequency of the emitted sound. And a scale of length, which gives the size of the elementary source region.

The magnitude of the enthalpy source is related to the the mean values of density and enthalpy, and the mean square value of velocity fluctuations. Via dimensional arguments, the mean square value of velocity fluctuations is related to turbulent kinetic energy, k. The relation is written

$$\sigma_{22}(\mathbf{x}) = \alpha_{k,h} k, \tag{4.84}$$

in which $\alpha_{k,h}$ is an empirical coefficient for the magnitude of the enthalpy source.

The mean square value of squared velocity fluctuations, σ_{2222}, gives the strength

of the momentum source. Via dimensional arguments, σ_{2222} is related to the kinetic energy via

$$\sigma_{2222}(\mathbf{x}) = 2\alpha_{k,m}k^2, \tag{4.85}$$

in which $\alpha_{k,m}$ is an empirical coefficient for the magnitude of the momentum term.

The length scale for the momentum and enthalpy sources are related to their time scales and turbulent kinetic energy via:

$$\ell_m = \alpha_{\ell,m}\tau_{0,m}k^{1/2}, \tag{4.86}$$

and

$$\ell_h = \alpha_{\ell,h}\tau_{0,h}k^{1/2}, \tag{4.87}$$

in which $\tau_{0,m}$ and $\tau_{0,h}$ are the time scales for the momentum and enthalpy sources, and $\alpha_{\ell,m}$ and $\alpha_{\ell,h}$ are empirical coefficients.

The momentum time scale is the turbulent-energy-transfer time scale proposed by Self and Azarpeyvand [13]:

$$\tau_{0,m} = \alpha_{\tau,m}\frac{k^2}{\varepsilon^{5/3}D_J^{2/3}}, \tag{4.88}$$

in which $\alpha_{\tau,m}$ is an empirical coefficient.

The enthalpy time scale is the traditional RANS scale,

$$\tau_{0,h} = \alpha_{\tau,h}\frac{k}{\varepsilon}, \tag{4.89}$$

in which $\alpha_{\tau,h}$ is an empirical coefficient.

The scales of turbulence given by Eqs. (4.84)–(4.89) are used in Eqs. (4.82) and (4.83) to present an equation for the farfield autospectral density using RANS data. The final equations for the momentum and enthalpy sources are

$$S_{pp}^m(r;\omega) = \frac{\alpha_{k,m}\alpha_{\ell,m}^3}{128a_0^4r^2}\int \overline{\rho}^2 k^{7/2}\tau_{0,m}^4\omega^4\exp\left(-\frac{\omega^2\tau_{0,m}^2}{8}\right)\mathrm{d}^3\mathbf{x}, \tag{4.90}$$

and

$$S_{pp}^{h}(r;\omega) = \frac{\alpha_{k,h}\alpha_{\ell,h}^{3}}{64a_0^2 r^2}\int \overline{\rho}^2 \left[\overline{h}/h_0 - 1\right]^2 k^{5/2}\tau_{0,h}^4\omega^4 \exp\left(-\frac{\omega^2\tau_{0,h}^2}{4}\right)\mathrm{d}^3\mathbf{x}, \qquad (4.91)$$

in which the time scales for the momentum and enthalpy contributions, $\tau_{0,m}$ and $\tau_{0,h}$, are computed from Eqs. (4.88) and (4.89). It is implicit that the variables in the integrand—except h_0 and ω—vary with $\mathbf{x}$.

The model for the enthalpy source adds three empirical coefficients to the method by Ilário et al. [10]. The new parameters, however, must be calibrated only for a single operating condition and are valid, for a given nozzle, in the entire subsonic range and for different temperature ratios. Therefore, the new model for the enthalpy source reduces the empiricism of the method for hot jets.

Chapter 5

Formulation with the frequency-domain model of turbulence statistics

This chapter proposes a new formulation for the source model presented in Chapter 4 is proposed in this chapter. The model of turbulence two-point statistics is modified and a new formulation to predict the far-field spectrum is presented. The new formulation uses a frequency-domain model of turbulence statistics instead of a time-domain model, and the assumptions about source compactness and isotropic turbulence are removed.

The frequency-domain model of turbulence statistics used in this thesis is based on the formulation by Harper-Bourne [12]. Harper-Bourne's formulation is reviewed and extended in Section 5.1. Two modifications are presented: (1) application of the spectrum function by von Kármán [47] to model the autospectral density, and (2) application of a modified von Kármán spectrum do model the spectrum of coherence length scales. In Section 5.2 the formulation to predict the farfield autospectral density is presented with the updated model for turbulence statistics.

5.1 Empirical model for cross-spectral density

The farfield spectrum was written in terms of the Fourier transform of the space–time correlation in Section 2.1.3. In Chapter 4 an empirical model of the space–time correlation was presented; its Fourier transform was taken so the farfield spectrum could be predicted. In this section, the Fourier transform of the space–time correlation, i.e. the cross-spectral density, is modelled directly.

The contribution from the momentum and enthalpy source terms may be written in terms of the cross-spectral density by using the cross-spectral density for the Fourier transform of the space–time correlation in Eqs (2.40) and (2.41). By neglecting the shear noise term and the fluctuations of thermodynamic variables from the source terms, the contribution to the farfield spectrum from the momentum and enthalpy sources in terms of the cross-spectral density are given by:

$$S_{pp}^{m}(\mathbf{r};\omega) = \frac{\omega^4}{16\pi^2 a_0^4 r^2} \int \overline{\rho}^2(\mathbf{x}) \int C_{rrrr}(\mathbf{x};\mathbf{s};\omega) \exp\left(i\frac{\omega}{a_0}\hat{\mathbf{r}}\cdot\mathbf{s}\right) \mathrm{d}^3\mathbf{s}\mathrm{d}^3\mathbf{x}, \tag{5.1}$$

and

$$\begin{aligned} S_{pp}^{h}(\mathbf{r};\omega) = \frac{\omega^4}{16\pi^2 a_0^2 r^2} \int \overline{\rho}^2(\mathbf{x}) \left[\overline{h}(\mathbf{x})/h_0 - 1\right]^2 \\ \times \int C_{rr}(\mathbf{x};\mathbf{s};\omega) \exp\left(i\frac{\omega}{a_0}\hat{\mathbf{r}}\cdot\mathbf{s}\right) \mathrm{d}^3\mathbf{s}\mathrm{d}^3\mathbf{x}. \end{aligned} \tag{5.2}$$

As discussed in Section 2.2.3, the cross-spectral density of a stationary function of time may be decomposed into autospectral density, coherence, and phase. Assuming that turbulence is stationary, the cross-spectral density of u_i and u_i^2 may thus be written as

$$C_{ii}(\mathbf{x};\mathbf{s};\omega) = \sqrt{S_{ii}(\mathbf{x};\omega) S_{ii}(\mathbf{x}+\mathbf{s};\omega)}\,\gamma_{ii}(\mathbf{x};\mathbf{s};\omega) \exp\left[-i\phi_{ii}(\mathbf{x};\mathbf{s};\omega)\right], \tag{5.3}$$

and

$$C_{iiii}(\mathbf{x};\mathbf{s};\omega) = \sqrt{S_{iiii}(\mathbf{x};\omega) S_{iiii}(\mathbf{x}+\mathbf{s};\omega)}\,\gamma_{iiii}(\mathbf{x};\mathbf{s};\omega) \exp\left[-i\phi_{iiii}(\mathbf{x};\mathbf{s};\omega)\right], \tag{5.4}$$

in which C_{iiii} is the cross-spectral density of u_i^2 and C_{ii} is the cross-spectral density of u_i.

The autospectral density varies more slowly with space separation than the coherence and phase. So it is assumed that the cross-spectral density varies with space separation only by the changes in coherence and phase. The cross-spectral density of u_i and u_i^2 may thus be written as

$$C_{ii}(\mathbf{x};\mathbf{s};\omega) = S_{ii}(\mathbf{x};\omega)\gamma_{ii}(\mathbf{x};\mathbf{s};\omega)\exp\left[-i\phi_{ii}(\mathbf{x};\mathbf{s};\omega)\right], \tag{5.5}$$

and

$$C_{iiii}(\mathbf{x};\mathbf{s};\omega) = S_{iiii}(\mathbf{x};\omega)\gamma_{iiii}(\mathbf{x};\mathbf{s};\omega)\exp\left[-i\phi_{iiii}(\mathbf{x};\mathbf{s};\omega)\right]. \tag{5.6}$$

The three components of the cross-spectral density affect the generation of sound in different ways. The autospectral density yields the overall strength and spectrum of the sources; the coherence yields the size of the elementary source region; and the phase affects the source efficiency and along with the coherence may result in source non-compactness. These three effects can be identified and modelled explicitly when considering a frequency-domain model of two-point statistics. The same is not true if the model is proposed in the time domain; in that case, the three components result from the Fourier transform of the empirical model.

5.1.1 Phase

The convection of the turbulent fluctuations results in a phase delay between the signal at two different locations if there is enough coherence between the signals. Harper-Bourne [12] showed that the phase speed of the turbulent fluctuations varies with frequency. The phase speed is minimum at low frequencies and grows monotonically with frequency.

The overall phase velocity, which accounts for an average of all frequencies, was shown by Davies, Fisher and Barrat [31] to be approximately the mean flow velocity on the lipline of the jet. The overall phase speed is lower than the mean flow velocity

in the potential core and higher than the mean flow velocity in the outer shear layer. The results by Harper-Bourne and Davies et al. have been corroborated by Kerhervé, Fitzpatrick and Jordan [52] and Morris and Zaman [53].

The largest variation of phase speed with frequency is at the low frequency. At low frequency the sound sources approach a compact behaviour, so the frequency dependence of the phase speed have a small effect on jet noise. So it is assumed that the phase speed is independent of frequency. Additionally, as the strongest sources are on the lipline, it is assumed that the phase velocity is equal to the mean flow velocity.

In axisymmetric jets the mean azimuthal velocity is zero and the mean radial velocity is negligible in comparison with the mean axial velocity. So the phase delay of turbulent fluctuations is related only to the mean axial velocity and axial separations. The phase of u_i and u_i^2 may thus be written as

$$\phi_{ii}(\mathbf{x};s_1;\omega) = \frac{\omega s_1}{\overline{U}_1(\mathbf{x})}, \tag{5.7}$$

and

$$\phi_{iiii}(\mathbf{x};s_1;\omega) = \frac{\omega s_1}{\overline{U}_1(\mathbf{x})}. \tag{5.8}$$

So far in the derivation of the model for the cross-spectral density it was assumed that (1) turbulence is time stationary so that the cross-spectral density may be decomposed in autospectral density, coherence, and phase; (2) the autospectral density is a weaker function of space separation than the coherence and phase; and (3) the turbulent fluctuations convect with the mean axial velocity. With these three assumptions, the cross-spectral density of u_i^2 and of u_i may be written as:

$$C_{iiii}(\mathbf{x};\mathbf{s};\omega) = S_{iiii}(\mathbf{x};\omega)\gamma_{iiii}(\mathbf{x};\mathbf{s};\omega)\exp\left(-i\frac{\omega s_1}{\overline{U}_1(\mathbf{x})}\right), \tag{5.9}$$

and

$$C_{ii}(\mathbf{x};\mathbf{s};\omega) = S_{ii}(\mathbf{x};\omega)\gamma_{ii}(\mathbf{x};\mathbf{s};\omega)\exp\left(-i\frac{\omega s_1}{\overline{U}_1(\mathbf{x})}\right). \tag{5.10}$$

The cross-spectral density given by Eqs. (5.9) and (5.10) is used to write the contribution from the momentum and enthalpy terms to the far-field as:

$$S^m_{pp}(\mathbf{x};\omega) = \frac{\omega^4}{16\pi^2 a_0^4 r^2} \int \overline{\rho}^2(\mathbf{x}) \times \int S_{iiii}(\mathbf{x};\omega)\gamma_{iiii}(\mathbf{x};\mathbf{s};\omega) \exp\left[-i\frac{\omega s_1}{\overline{U}_1(\mathbf{x})}\right] \mathrm{d}^3\mathbf{s}\mathrm{d}^3\mathbf{x}, \tag{5.11}$$

and

$$S^h_{pp}(\mathbf{x};\omega) = \frac{\omega^4}{16\pi^2 a_0^2 r^2} \int \overline{\rho}^2(\mathbf{x}) \left[\overline{h}(\mathbf{x})/h_0 - 1\right]^2 \times \int S_{ii}(\mathbf{x};\omega)\gamma_{ii}(\mathbf{x};\mathbf{s};\omega) \exp\left[-i\frac{\omega s_1}{\overline{U}_1(\mathbf{x})}\right] \mathrm{d}^3\mathbf{s}\mathrm{d}^3\mathbf{x}. \tag{5.12}$$

Now to enable the computation of S^m_{pp} and S^h_{pp} models for the autospectral density and coherence are introduced in Sections 5.1.2 and 5.1.3.

5.1.2 Autospectral density

The autospectral density of the turbulent fluctuations in the source terms gives the energy distribution of the turbulent signal with frequency. The autospectral density of the source terms are, therefore, the autospectral density of the sound sources. There is a vast literature on the autospectral density of turbulence, yet the analysis of turbulence autospectral density for modelling jet noise has been mostly ignored.

Von Kármán [47] proposed a model for the energy spectrum of turbulence that can be used to compute the turbulence autospectral density for homogeneous turbulence (see Batchelor [24]). Amiet [54] applied the model by von Kármán for aeroacoustics applications in which the turbulence is homogeneous. Glegg and Devenport [55] discussed the application of von Kármán spectrum to model the turbulence in a near-wall boundary layer. In this thesis, the application of the von Kármán spectrum for free shear layers is introduced.

The form presented by Glegg and Devenport for the autospectral density is used:

$$S_{ii}(\mathbf{x},\omega) = \frac{1}{\pi}\sigma_{ii}(\mathbf{x})\frac{L_{ii}(\mathbf{x})}{\overline{U}_1(\mathbf{x})}\left[1+\left(\frac{\omega L_{ii}(\mathbf{x})}{2\pi\overline{U}_1(\mathbf{x})}K\right)^2\right]^{-5/6}, \tag{5.13}$$

in which K is the constant

$$K = \frac{\Gamma(1/3)}{\sqrt{\pi}\Gamma(5/6)}, \tag{5.14}$$

and $\Gamma()$ is the gamma function.

Contrary to the derivation by Glegg and Devenport [55], the same functional form is used independent of velocity direction—Glegg and Devenport presented different formulations for the longitudinal and transverse velocities.

The equation for the autospectral of squared velocity fluctuations u_i^2 is a direct generalisation of the equation for S_{ii} and may be written as

$$S_{iiii}(\mathbf{x},\omega) = \frac{1}{\pi}\sigma_{iiii}(\mathbf{x})\frac{L_{iiii}(\mathbf{x})}{\overline{U}_1(\mathbf{x})}\left[1+\left(\frac{\omega L_{iiii}(\mathbf{x})}{2\pi\overline{U}_1(\mathbf{x})}K\right)^2\right]^{-5/6}. \tag{5.15}$$

5.1.3 Coherence

The coherence is a non-dimensional quantity that gives the degree of correlation at a given frequency between two locations of the turbulent flow. Harper-Bourne [12] showed that the coherence decay of axial velocity fluctuations is approximately exponential with axial separation and approximately Gaussian with radial and azimuthal separations. Harper-Bourne used hot-wire anemometry of a high-Reynolds number incompressible jet ($Re_J \approx 2\times10^5$, $M \approx 0.18$). Morris and Zaman [53] corroborated Harper-Bourne's results for an incompressible jet at higher Mach number ($M = 0.25$). Proença, Self and Lawrence [56] corroborated the results for compressible jets with $M = 0.6$.

To accommodate the exponential–Gaussian behaviour of the coherence decay, Harper-Bourne [12] proposed the following empirical function:

$$\gamma_{ii}(\mathbf{x},\mathbf{s},\omega) = \exp\left[-\sqrt{\left(\frac{s_1}{\ell_{ii,1}(\mathbf{x},\omega)}\right)^2+\left[\left(\frac{s_2}{\ell_{ii,2}(\mathbf{x},\omega)}\right)^2+\left(\frac{s_3}{\ell_{ii,3}(\mathbf{x},\omega)}\right)^2\right]^2}\right], \tag{5.16}$$

in which $\ell_{ii,k}$ is the length scale of velocity fluctuations, u_i, and related to the space separation s_k. See Fig. 5.1 for the definition of the coordinate systems with the space separation vector.

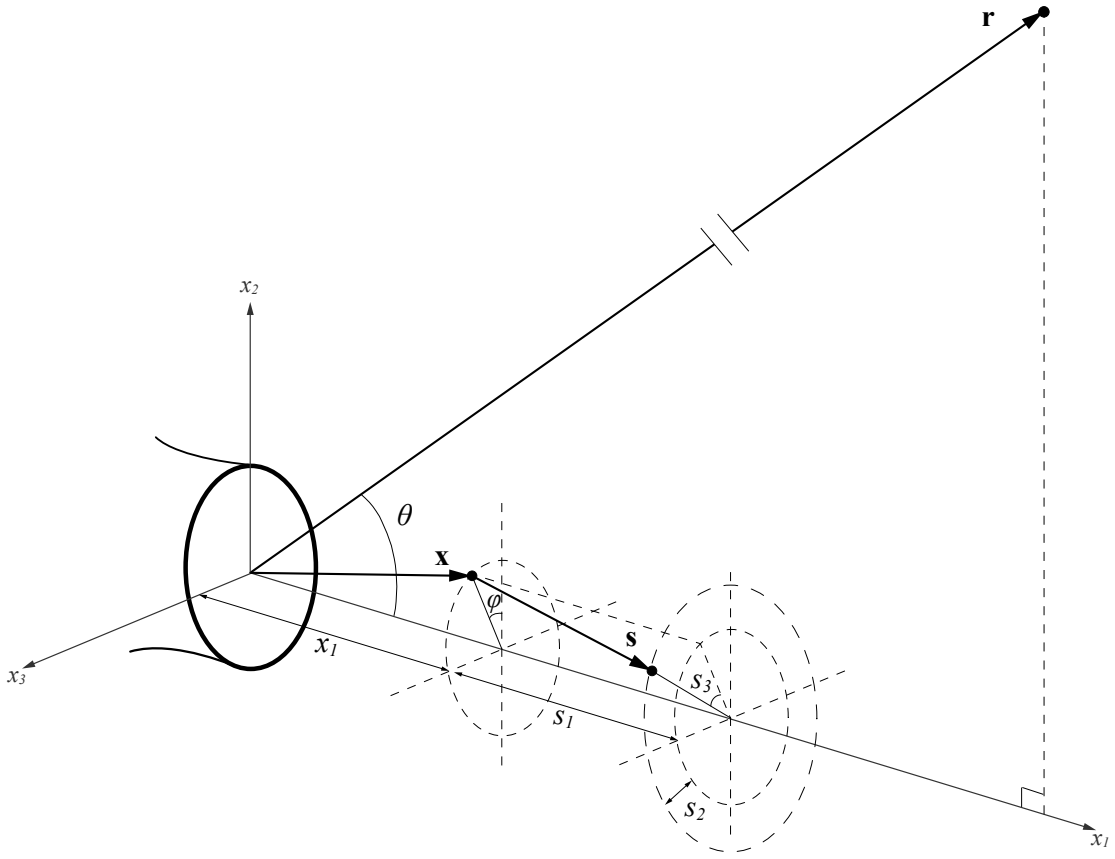

FIGURE 5.1: Coordinate systems showing farfield location (**r**), source location (**x**), and separation vector (**s**).

The same model is used for squared velocity fluctuation, u_i^2, with relevant changes of length scales:

$$\gamma_{iiii}(\mathbf{x},\mathbf{s},\omega) = \exp\left[-\sqrt{\left(\frac{s_1}{\ell_{iiii,1}(\mathbf{x},\omega)}\right)^2+\left[\left(\frac{s_2}{\ell_{iiii,2}(\mathbf{x},\omega)}\right)^2+\left(\frac{s_3}{\ell_{iiii,3}(\mathbf{x},\omega)}\right)^2\right]^2}\right], \tag{5.17}$$

in which $\ell_{iiii,k}$ is the length scale for the coherence of squared velocity fluctuations, u_i^2, related to the separation s_k.

In the models of coherence it assumed that the length scales vary within the jet plume and depend on frequency. Harper-Bourne [12] introduced a model for the spectrum of the length scales. A new model for the length scale spectrum which is related to the autospectral density model is presented in the next section.

New model for the length scale spectrum

The model for coherence decay in Eqs. (5.16) and (5.17) accounts for the frequency-dependence of the length scales. Harper-Bourne [12] and Morris and Zaman [53] showed that the spectrum of length scales is flat at low to mid frequencies and decays linearly with frequency at high frequency. The same behaviour is observed for the length scale with axial, radial and azimuthal separations; but the axial length scale is larger and its spectrum has a lower cut-off frequency, whereas the radial and azimuthal have similar levels and cut-off frequency.

Harper-Bourne [12] proposed an empirical model for the length scale spectrum that takes an exponential form. For instance, the model for the length scale of u_1 with axial separation is

$$\ell_{11,1}/D_J = \left[1-\exp\left(-St/St_0\right)\right]/(St/St_0), \tag{5.18}$$

in which St_0 is a local Strouhal number defining the cut-off frequency where the spectrum transitions to a linear decay. This model fits well hotwire data, but shows no

relationship with other empirical models of turbulence statistics.

The autospectral density and length scales spectrum have a similar behaviour. They are flat at low to mid frequencies up to a cut-off frequency when they start to decay. The decay at high frequency, however, is steeper for the autospectral density. The model for the autospectral density predicts a high-frequency decay of $\omega^{-5/3}$, whereas Harper-Bourne [12] measured a high-frequency decay of the coherence length with ω^{-1}. To use a similar model for both spectra whilst accounting for the different high-frequency decays, the exponent of the von Kármán spectrum is modified and used to model the length scale spectrum.

The empirical model for the length scale spectrum based on a modified von Kármán function is

$$\ell_{ii,k}(\omega) = L_{ii}\alpha_{\ell,k}\left[1+\left(\frac{\omega L_{ii}\alpha_{\ell,k}}{2\pi\overline{U}_1}\right)^2\right]^{-3/6}, \tag{5.19}$$

in which L_{ii} is the integral length scale of u_i and $\alpha_{\ell,k}$ is an empirical coefficient.

The model for the length scale spectrum of squared velocity fluctuations is

$$\ell_{iiii,k}(\omega) = L_{iiii}\alpha_{\ell,k}\left[1+\left(\frac{\omega L_{iiii}\alpha_{\ell,k}}{2\pi\overline{U}_1}\right)^2\right]^{-3/6}. \tag{5.20}$$

The anisotropy of the length scale with direction of separation is computed via the empirical coefficient $\alpha_{\ell,k}$. It is assumed that u_i and u_i^2 are equally anisotropic, so the same coefficient $\alpha_{\ell,k}$ is used for the length scales of u_i and u_i^2.

5.2 Formulation to predict the farfield autospectral density

The contribution from the momentum and enthalpy terms to the farfield autospectral density were given in Eqs. (5.11) and (5.12) in terms of the autospectral density, coherence, and phase of the source terms. Models for the these three components of the

cross-spectral density were introduced in Sections 5.1.1–5.1.3, and are in this section used in the formulation for the farfield autospectral density.

5.2.1 Volume integral with space separation

The inner volume integrals in the equations for the farfield spectrum (Eqs. (5.11) and (5.12)) give the effective volume of the elementary sound sources. The effective volume combines the size of the elementary source given by the coherence length scales with non-compactness effects caused by differences in retarded time and phase delay within the source volume. The effect of the length scales and non-compactness are split by computing independently the volume due to coherence decay and defining a non-compactness factor.

The volume from the coherence decay is computed by integrating the coherence functions of u_i^2 and u_i:

$$V_{iiii}(\mathbf{x},\omega) = \int \gamma_{iiii}(\mathbf{x},\mathbf{s},\omega)\mathrm{d}^3\mathbf{s}, \tag{5.21}$$

and

$$V_{ii}(\mathbf{x},\omega) = \int \gamma_{ii}(\mathbf{x},\mathbf{s},\omega)\mathrm{d}^3\mathbf{s}. \tag{5.22}$$

The volume integrals in Eqs. (5.21) and (5.22) were computed by Harper-Bourne [12], yielding the elementary volume of the momentum and enthalpy sources as:

$$V_{iiii}(\mathbf{x},\omega) = \pi^2 \ell_{iiii,1}(\mathbf{x},\omega)\ell_{iiii,2}(\mathbf{x},\omega)\ell_{iiii,3}(\mathbf{x},\omega), \tag{5.23}$$

and

$$V_{ii}(\mathbf{x},\omega) = \pi^2 \ell_{ii,1}(\mathbf{x},\omega)\ell_{ii,2}(\mathbf{x},\omega)\ell_{ii,3}(\mathbf{x},\omega), \tag{5.24}$$

in which $\ell_{iiii,k}$ and $\ell_{ii,k}$ are the frequency-dependent length scales of coherence for u_i^2 and u_i.

The non-compactness factor is the ratio between the effective source volume (considering phase delay and retarded time differences) and the source volume due only to the coherence decay. The non-compactness factors for the momentum and enthalpy

sources are

$$N_{iiii}(\mathbf{x};\omega) = V_{iiii}^{-1}(\mathbf{x},\omega)\int \gamma_{iiii}(\mathbf{x};\mathbf{s};\omega)\exp\left(-i\frac{\omega s_1}{\overline{U}_1(\mathbf{x})}\right)\exp\left(i\frac{\omega}{a_0}\hat{\mathbf{r}}\cdot\mathbf{s}\right)\mathrm{d}^3\mathbf{s}, \quad (5.25)$$

and

$$N_{ii}(\mathbf{x};\omega) = V_{ii}^{-1}(\mathbf{x},\omega)\int \gamma_{ii}(\mathbf{x};\mathbf{s};\omega)\exp\left(-i\frac{\omega s_1}{\overline{U}_1(\mathbf{x})}\right)\exp\left(i\frac{\omega}{a_0}\hat{\mathbf{r}}\cdot\mathbf{s}\right)\mathrm{d}^3\mathbf{s}. \quad (5.26)$$

Considering the coordinate system in Fig. (5.1), the cross-product related to retarded time differences in Eqs. (5.25) and (5.26) is

$$\hat{\mathbf{r}}\cdot\mathbf{s} = s_1\cos\theta + s_2\cos s_3\sin\theta, \quad (5.27)$$

in which s_2 is the radial separation in units of length and s_3 is the azimuthal separation in radians.

The results of the cross-product between farfield location and space separation (Eq.(5.27)) is used to combine the arguments of the exponentials in Eqs. (5.25) and (5.26) as

$$i\omega\left(-\frac{s_1}{\overline{U}_1(\mathbf{x})}+\frac{1}{a_0}\hat{\mathbf{r}}\cdot\mathbf{s}\right) = i\omega\left[s_1\left(-\frac{1}{\overline{U}_1(\mathbf{x})}+\frac{\cos\theta}{a_0}\right)+\frac{s_2}{a_0}\cos s_3\sin\theta\right], \quad (5.28)$$

in which the effects of non-compactness in the axial and radial directions are now distinguished.

The radial non-compactness factor is a more traditional acoustic non-compactness factor. The acoustic wavenumber in the direction of the observer $\omega\sin\theta/a_0$ is compared to the size of the source region given by the coherence decay with radial separation. Owing to the small length scale in the radial direction, the source is assumed compact in the radial direction.

Assuming compactness only in the radial direction and using Eq. (5.28) to rewrite the exponential arguments of Eqs. (5.25) and (5.26), the non-compactness factors of

the momentum and enthalpy sources are given by:

$$N_{iiii}(\mathbf{x},\omega) = V_{iiii}^{-1}(\mathbf{x},\omega)\int \gamma_{iiii}(\mathbf{x},\mathbf{s},\omega)\exp\left[-i\omega s_1\left(\frac{1}{\overline{U}_1(\mathbf{x})}-\frac{\cos\theta}{a_0}\right)\right]\mathrm{d}^3\mathbf{s}, \quad (5.29)$$

and

$$N_{ii}(\mathbf{x},\omega) = V_{ii}^{-1}(\mathbf{x},\omega)\int \gamma_{ii}(\mathbf{x},\mathbf{s},\omega)\exp\left[-i\omega s_1\left(\frac{1}{\overline{U}_1(\mathbf{x})}-\frac{\cos\theta}{a_0}\right)\right]\mathrm{d}^3\mathbf{s}. \quad (5.30)$$

The axial non-compactness consists of two effects. An effect related to turbulence convection given by $\omega s_1/\overline{U}_1$ and a more traditional acoustic non-compactness related to $\omega s_1\cos\theta/a_0$. The former depends on the direction of the mean flow, whereas the latter depends only on the location of the farfield observer. The volume integrals in Eqs. (5.29) and (5.30) combine these two effects, yielding the non-compactness of the momentum and enthalpy sources as [12]:

$$N_{iiii}(\mathbf{x},\omega) = \left[1+\left(\frac{\omega\ell_{iiii,1}(\mathbf{x},\omega)}{\overline{U}_1(\mathbf{x})}\left(1-M_1(\mathbf{x})\cos\theta\right)\right)^2\right]^{-3/2}, \quad (5.31)$$

and

$$N_{ii}(\mathbf{x},\omega) = \left[1+\left(\frac{\omega\ell_{ii,1}(\mathbf{x},\omega)}{\overline{U}_1(\mathbf{x})}\left(1-M_1(\mathbf{x})\cos\theta\right)\right)^2\right]^{-3/2}, \quad (5.32)$$

in which M_1 is the local axial acoustic Mach number, $M_1(\mathbf{x}) = \overline{U}_1(\mathbf{x})/a_0$. Note that this Mach number is not strictly the local Mach number of the flow, but is related to the phase speed of the turbulent fluctuations ($\overline{U}_1$) and the process of sound radiation from turbulence.

The factor $(1-M_1(\mathbf{x})\cos\theta)$ can be related to the traditional convective amplification effect of moving simple sources. For the sound sources related to convecting turbulence, such effect of convective amplification is mixed with the attenuation effect due to the size of the coherent region of turbulence (the factor $\omega\ell_{ii,1}/\overline{U}_1$). At $\theta = 90^\circ$ the non-compactness factor is only due to the large coherence length scale of turbulence, as the factor $(1-M_1(\mathbf{x})\cos\theta)$ is identically unity.

The large attenuation due to the non-compactness factor (see Section 8.2) makes

the the non-compactness factor N_{ii} and N_{iii} vary with $\sim (1 - M_1(\mathbf{x})\cos\theta)^{-3}$. This dependence agrees with measured farfield data by Harper-Bourne [57].

5.2.2 Equations for the farfield autospectral density

With the introduction of the elementary source volume, V_{rrrr} and V_{rr}, and non-compactness factors, N_{rrrr} and N_{rr}, the contribution to the farfield spectrum from the momentum and enthalpy terms may be written as:

$$S_{pp}^{m}(\mathbf{r},\omega) = \frac{\omega^4}{16\pi^2 a_0^4 r^2} \int \overline{\rho}^2(\mathbf{x}) S_{rrrr}(\mathbf{x},\omega) V_{rrrr}(\mathbf{x},\omega) N_{rrrr}(\mathbf{x},\omega) \mathrm{d}^3\mathbf{x}, \tag{5.33}$$

and

$$S_{pp}^{h}(\mathbf{r},\omega) = \frac{\omega^4}{16\pi^2 a_0^2 r^2} \int \overline{\rho}^2(\mathbf{x}) \left[\overline{h}(\mathbf{x})/h_0 - 1\right]^2 S_{rr}(\mathbf{x},\omega) V_{rr}(\mathbf{x},\omega) N_{rr}(\mathbf{x},\omega) \mathrm{d}^3\mathbf{x}, \tag{5.34}$$

in which the subscripts rr and $rrrr$ denote the properties are related u_r and u_r^2, respectively. The models for S_{rrrr}, V_{rrrr}, and N_{rrrr} are given by Eqs. (5.15), (5.23), and (5.31); those for S_{rr}, V_{rr}, and N_{rr} are given by Eqs. (5.13), (5.24), and (5.32).

The contribution from the source terms to the farfield spectrum in the form of Eqs. (5.33) and (5.34) is an important contribution of using a frequency-domain model for turbulence statistics. The equations in this form show clearly the effect of mean thermodynamic variables, turbulence autospectral density, coherence length scales, and source non-compactness.

Chapter 6

Results — validation of the prediction method with enthalpy source

Chapter 4 introduced a method to predict the farfield noise of hot jets. The new method adds a model for the enthalpy source to the source model used by Ilário et al. [10]. In this chapter the model for the enthalpy source is assessed by using numerical and experimental data.

In Section 6.1 the centreline decay of the mean axial velocity from large eddy simulations, from steady RANS solutions, and from measured data are compared. The goal of the section is to assess the accuracy of the numerical solutions and show the differences between isothermal and hot jets. The large eddy simulation data is also used in Section 6.2 to assess some assumptions of the source model. Farfield predictions are compared to experimental data in Sections 6.3 and 6.4.

6.1 Centreline decay of mean axial velocity

The RANS and LES solutions computed for the nozzle in Fig. 6.1 are compared with the experimental data by Bridges and Wernet [58]. The axial decay of the mean axial velocity in the centreline is compared between the numerical and experimental data. The mean axial velocity gives the overall topology of the jet by defining the potential core length, and is assumed to be the phase speed of turbulence fluctuations: so the

mean axial velocity is an important property for jet noise and can give an overview of the accuracy of the numerical solutions.

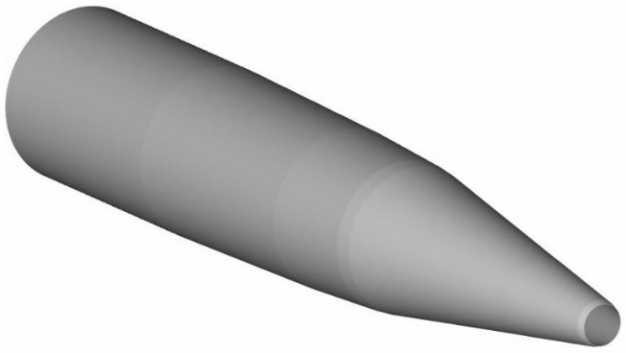

FIGURE 6.1: Nozzle geometry used for numerical solutions and for farfield measurements. Baseline circular nozzle with exit-diameter $D_J = 0.1016$m.

The mean axial velocity on the jet centreline defines the length of the potential core. Within the potential core the mean axial velocity is approximately equal to the nominal jet-exit velocity, but further downstream the mean velocity starts to decay because of the mixing of the jet with the external fluid. The distance between the location where $\overline{U}_1(x_1) \approx 0.99U_J$ and the nozzle exit may be defined as the length of the potential core.

Figure 6.2 shows the centreline decay of $\overline{U}_1$ from numerical and experimental data. The downward arrows indicate the approximate location of the end of the potential core for the hot (grey lines) and isothermal (black lines) jets from the experimental data. The experimental data show that the potential core of the hot jet is shorter.

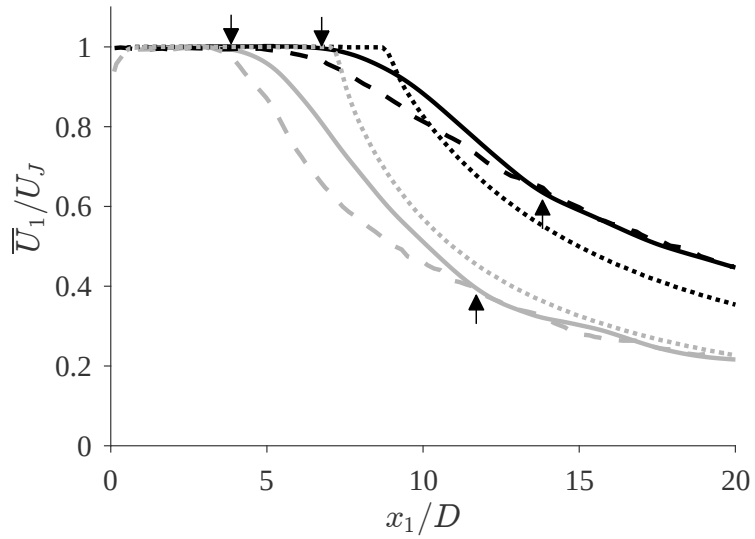

FIGURE 6.2: Centreline decay of the mean axial velocity. Continuous lines, data from Bridges and Wernet [58] (their setpoints 7 and 46); dashed lines, LES data; dotted lines, RANS data. Black lines, isothermal jets; grey lines, hot jets ($T_R \approx 2.5$). All results for $M \approx 0.9$. Arrows indicate the end of the potential core for the isothermal and hot jets.

The shorter potential core in the hot jet may be related to the lower momentum and higher mixing rate of the hot jet. The lower momentum is due to a lower density of the jet. The increase in mixing is caused by higher instabilities due to the density inhomogeneities and increases in vorticity due to the effect of baroclinicity in the jet (an additional generation term in the vorticity equation). In addition to a shorter potential core, the higher levels of instability and vorticity in the hot jet lead to a steeper decay of $\overline{U}_1$ after the end of the potential core.

The large eddy simulation underpredicts the potential core length and overpredicts the decay rate of $\overline{U}_1$ after the end of the potential core. Such underprediction may be related to the differences in the nozzle design and to the state of the boundary layer at the nozzle exit.

The large eddy simulation uses a mean profile to model the boundary layer near walls, so the flow at the nozzle lip is effectively a mean flow. Just downstream the nozzle lip the flow transitions from the mean profile to an unsteady flow, and further downstream the flow reaches a fully-turbulent state. The transition from the mean profile to the turbulent unsteady flow leads to an over-growth of instabilities when compared to the real unsteady boundary layer. The higher level of instabilities leads to

overprediction of mixing rate, hence the underprediction in potential core length and overprediction of the decay rate after the end of the potential core.

A known limitation of RANS k–ε solutions is observed in Fig. 6.2: the potential core length is overpredicted. It can also be seen that the overprediction gets worse for the hot jet, and that the transition from the profile in the potential core to the profile in the fully-developed region is too steep.

The upward arrows in Fig. 6.2 show the start of the fully-developed region of the jet. In the fully developed region the profiles from the large eddy simulation and RANS solution agree with experimental data, but the results from the RANS solution are shifted with axial coordinate.

The potential core length shown in Table 6.1 is used to scale the axial coordinate for the results in Fig. 6.3. The effect of a different decay after the end of potential core becomes more evident. It is shown that for the experimental and RANS data scaling the axial coordinate accounts for the self-similarity between hot and isothermal jets. The large eddy simulation data, however, do not fully scale with the potential core length.

TABLE 6.1: Potential core length.

	Bridges and Wernet [58]	LES [14]	RANS
isothermal	$7D_J$	$6D_J$	$8.5D_J$
hot	$4.2D_J$	$3.9D_J$	$6.8D_J$

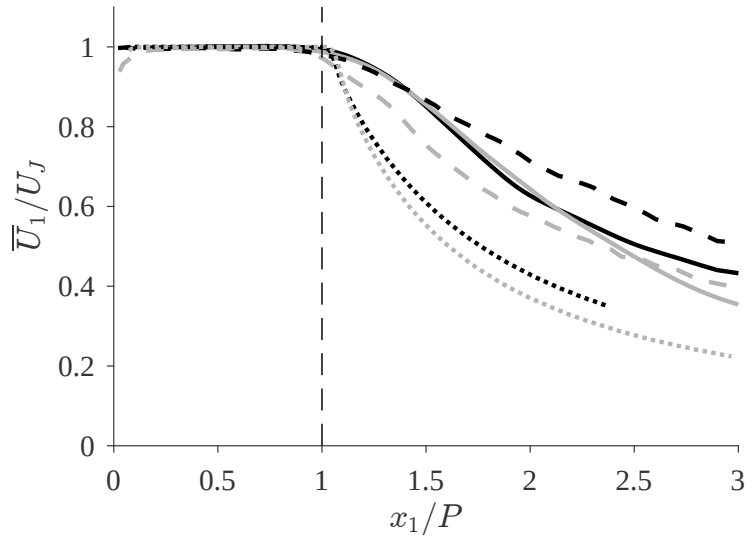

FIGURE 6.3: Centreline decay of the mean axial velocity, with axial coordinate scaled by the potential core length (P). Same results as Fig. 6.2.

6.2 Assumptions of the source model

Neglecting the thermodynamic fluctuations from the source terms and assuming the momentum and enthalpy sources are uncorrelated are common assumptions in jet noise models, but they are not so often assessed because of the difficulties in measuring fluctuations of thermodynamic variables in the jet plume. In Sections (6.2.1) and (6.2.2) the large eddy simulation data for isothermal and hot jets are used to assess these assumptions.

6.2.1 Neglect of thermodynamic fluctuations

The momentum and enthalpy sources consist of fluctuations of velocity and thermodynamic variables. In Section 4.2.2 the momentum and enthalpy terms were simplified by neglecting the contribution from density and enthalpy fluctuations. In this section large eddy simulations are used to compute the mean square value of the source terms and compute the error incurred by the simplification.

Momentum term

The exact momentum term is related to fluctuations of velocity and density. It is usual to ignore density fluctuations from the momentum term for low-Mach number isothermal jets. It is not evident, however, that the simplification is valid for transonic Mach number and hot jets. This assumption is assessed by comparing the mean square value of the exact term, $\overline{\rho(u_i^2)^2}$, with the mean square value of the approximate term, $\overline{\rho}^2\ \overline{(u_i^2)^2}$. Unsteady data from large eddy simulations for an isothermal and a hot jet with Mach number 0.88 are used.

Figure 6.4 shows the mean square value of the exact and approximated momentum term on the lipline of the isothermal jet. Results are plotted for the mean square value of velocity fluctuations in the axial, azimuthal, and radial directions. The mean square value, denoted by σ, is normalised. Using the approximation to predict the acoustic farfield would lead to a maximum error of 0.08dB in the prediction of the farfield mean square pressure.

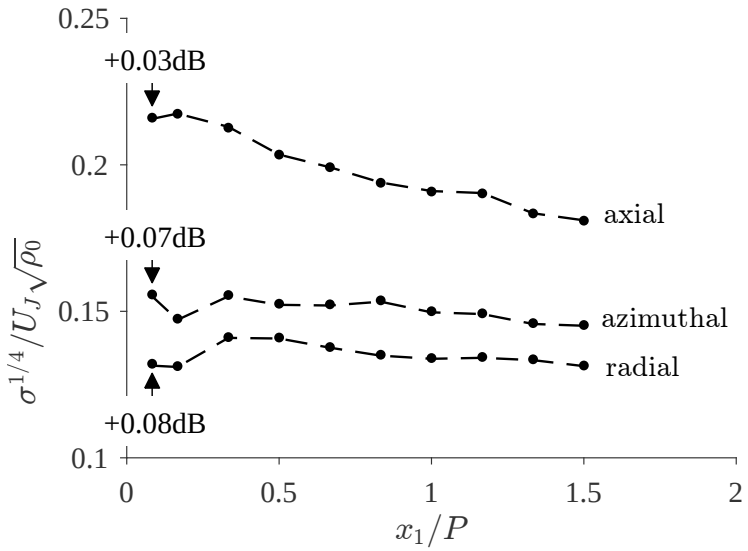

FIGURE 6.4: Dashed line, mean square value of the exact momentum term; dots, mean square value of the approximated momentum term. Results from the LES on the lipline of isothermal jet ($M = 0.88$, $T_R = 1$). Values in dB indicate the error incurred on the prediction of the farfield mean square pressure.

Mixing of fluids with different temperatures increases the error caused by the approximation, as shown in Fig. 6.5. For a hot jet with temperature ratio of 2.5 the error

incurred by neglecting density fluctuations is of underprediction of the mean square value and is as large as -1dB. The underprediction indicates that the density fluctuations increase the strength of the momentum source. The error is, however, only significant in a small region of the jet, at around a quarter of the potential core length from the nozzle exit. Overall, the approximation is still assumed valid.

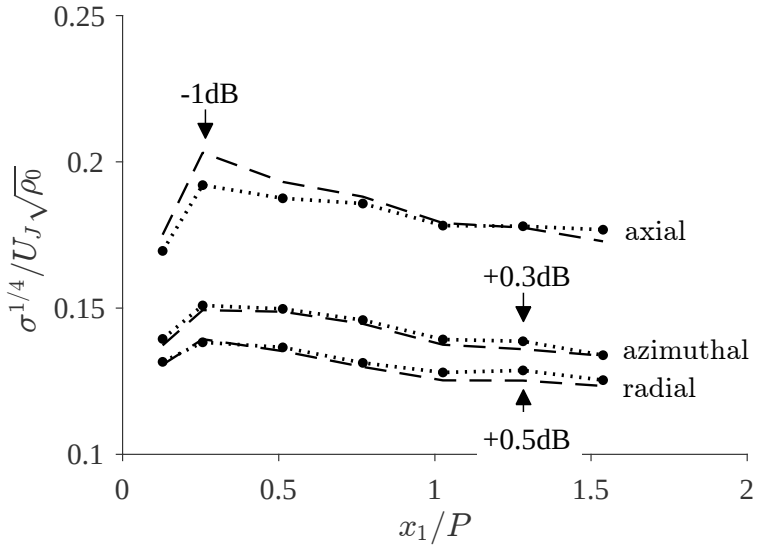

FIGURE 6.5: Dashed line, mean square value of exact momentum term; dotted lines with symbols, mean square value of approximated momentum term. Results from the LES on the lipline of hot jet ($M = 0.88$, $T_R = 2.5$). Values in dB indicate the error incurred on the prediction of the farfield mean square pressure.

Enthalpy term

The enthalpy source term is related to fluctuations of velocity, density, and enthalpy. In Section 4.2.2 the fluctuations of density and enthalpy were neglected from the enthalpy term. To assess the effect of such simplification, the mean square value of the exact enthalpy term, $\overline{[\rho(h/h_0-1)u_i]^2}$, is compared with the mean square value of the simplified enthalpy term, $\overline{\rho}^2(\overline{h}/h_0-1)^2\overline{u_i^2}$. The large eddy simulation of the hot jet ($T_R = 2.5$) and $M = 0.88$ is used for the comparison.

Figure 6.6 shows that the simplified term overpredicts the exact term. The overprediction is larger in the same region where of maximum error in the simplification of the momentum term ($x_1 \approx P/4$), but it is also significant for other axial locations, and also for the azimuthal and radial components.

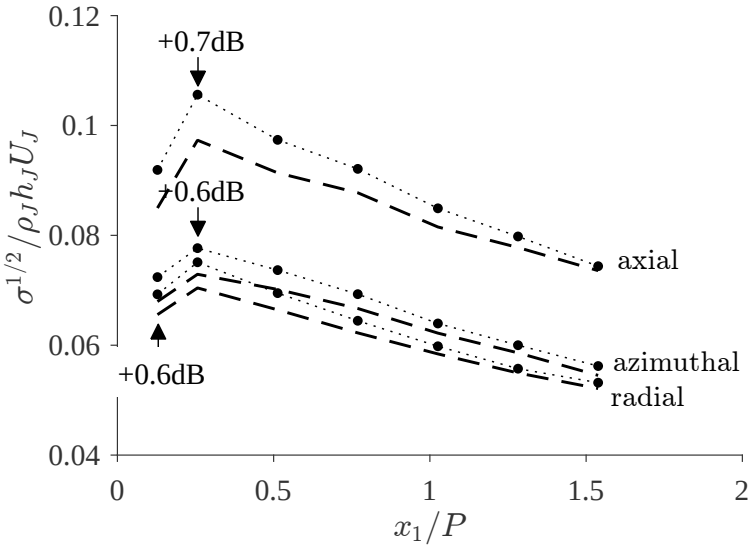

FIGURE 6.6: Dashed line, mean square value of exact enthalpy term; dotted line with symbols, mean square value of approximated term. Results from the LES on the lipline of hot jet ($M = 0.88$, $T_R = 2.5$). Values in dB indicate the error incurred on the prediction of the farfield mean square pressure.

The error in the farfield prediction is small for the isothermal jet, but gets significant in the hot jet (for both the momentum and enthalpy sources). Nevertheless, the simplification is considered because the error can be accounted for when calibrating the method with farfield data. So, effectively, it is assumed that the error scales with velocity and temperature in the subsonic range, in which the calibration is assumed valid.

6.2.2 Correlation between momentum and enthalpy sources

It is assumed in the derivation of the source model that the contribution from the momentum and enthalpy sources to the farfield autospectral density are statistically independent. To validate this assumption the correlation between the momentum and enthalpy source terms are computed in the jet plume using large eddy simulation data.

The assessment is done by computing the covariance between the momentum and enthalpy terms in the lipline of the jet. Figure 6.7 shows results of the covariance of the approximated source terms in the radial direction; i.e., the covariance between u_2^2 and u_2.

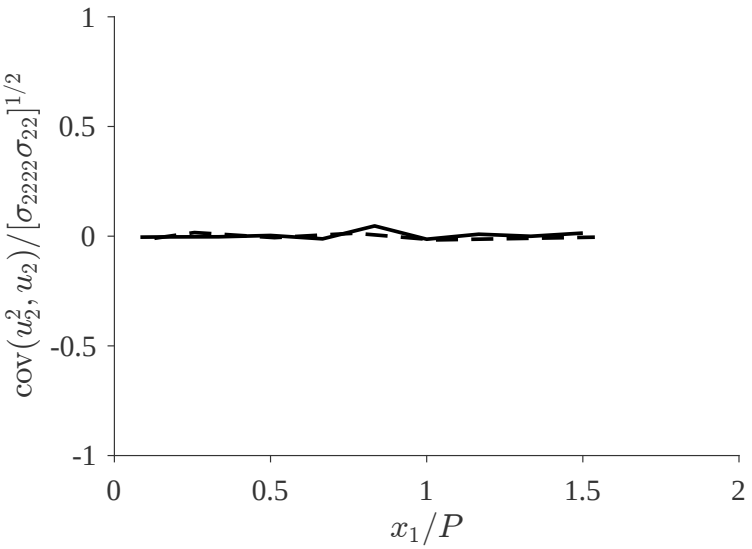

FIGURE 6.7: Covariance between u_2^2 and u_2—the approximate momentum and enthalpy terms. Continuous line, isothermal jet ($T_R = 1$); dashed line, hot jet ($T_R = 2.5$). Both for the large eddy simulation of the $M = 0.88$ jet.

A negligible covariance is also observed if the exact terms are considered. This is expected because in the exact term the fluctuations are of higher order so the covariance tends to decrease.

6.3 Scaling of farfield mean square pressure

A scaling law based on the no-flow acoustic analogy is used as a first validation of the enthalpy source model. To derive the no-flow acoustic analogy presented in Section 2.1, the non-barotropic term from Lighthill's equation is rewritten by use of the energy equation. The derivation follows the one presented by Lilley [18, 19] and the non-barotropic term is written in terms of enthalpy. A dimensional analysis has been applied to present a scaling law for the farfield mean square pressure (see Section 4.1). In this section the scaling law is applied to experimental farfield data to validate the model for the enthalpy source.

6.3.1 Experimental data

The scaling law is applied to two sets of measurements taken at the QinetiQ Noise Test Facility. The facility consists of an anechoic chamber approximately 27m long, 26m wide, and with a height of approximately 15m. The chamber is anechoic down to approximately 90Hz (see Martlew et al. [59] for more details about the facility).

The datasets are for two different nozzles, both single-stream circular. The measurements taken in 1983 [60, 61] (hereafter referred to as QinetiQ1983) are for a nozzle with diameter of 0.0861m, with the microphones located at a distance of approximately 12m from the nozzle exit. The measurements taken in 2009 [62] (hereafter referred to as QinetiQ2009) used a different nozzle, with diameter of 0.1016m, with the microphones located at the same approximate distance of 12m. Figure 6.8 shows a typical set up of the test facility for these measurements.

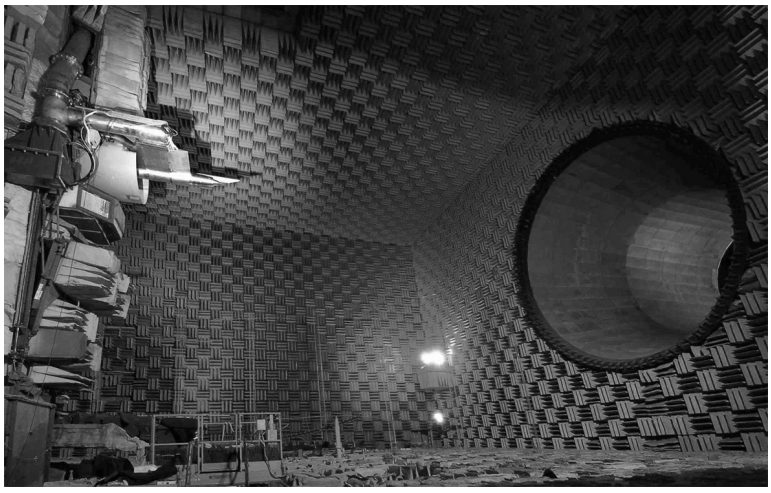

FIGURE 6.8: Noise Test Facility at QinetiQ. Photo taken for the 2009 test campaign [62].

Both datasets used microphones farther than $120D_J$ from the nozzle exit; which is more than the minimum of $\approx 50D_J$ suggested by Viswanathan [63] to guarantee that the measurements are taken in the true acoustic farfield.

Given that the engineering application of this study is to model the noise generated by the jet of aeroengines, care must be taken that effects of Reynolds number are not significant so the conclusions of the small-scale study can be applied for the real-scale problem. Karon and Ahuja [64] analysed nozzles with diameters ranging from 0.25

to 2 inches, in the velocity range related to acoustic Mach numbers from 0.4 to 0.8. Karon and Ahuja found that "the Reynolds number does not have a significant effect on jet noise, and jet noise can be scaled from even the smallest of nozzle to larger nozzles". Considering that the nozzles used in this thesis are larger than the ones studied by Karon, hence with a Reynolds number closer to the ones in actual engines, it is concluded that the effect of Reynolds number will not affect the conclusions of the study in the thesis.

The two databases in this thesis were taken at the same facility. That raises warning regarding the generality of the conclusions. For example, Viswanathan [65] discussed how measurements taken at the Low Speed Aeroacoustic Facility (LSAF) at Boeing differ from the ones taken by Ahuja and Bushell [66] and Tanna, Dean, and Fisher [50]. Viswanathan concluded that the differences were due to Reynolds number effects and to differences in the experimental facilities. The effects of Reynolds number were, as discussed in the previous paragraph, recently dismissed by Karon and Ahuja [64]. The differences due to experimental facilities were discussed by Harper-Bourne [67]. Harper-Bourne concluded that it is more likely that the differences in the measured spectra are due to the nozzle geometry and its effects on the boundary layer at the nozzle exit than differences in the experimental facilities.

Therefore, it is concluded that the experimental data used in this thesis does not restrict the conclusions in terms of Reynolds number nor experimental facility, but does limit the conclusions in terms of nozzle geometry.

Results from the QinetiQ1983 dataset

This section presents the results of mean square pressure for subsonic jets. The acoustic Mach number varies from 0.5 to 1.0 for isothermal jets, and is extended to 1.5 for hot jets. The temperature ratio ranges from 1.0 (isothermal) to 2.5. To enable a complete interpretation with the no-flow acoustic analogy, the data is analysed only for a polar angle of $\theta = 90^\circ$.

The measured mean square pressure ($\overline{p^2}_{\mathrm{EXP}}$) is shown in Fig. 6.9. The differences

between the isothermal (circles) and hottest jets (crosses) are small, with a maximum difference of approximately 3dB at $M = 0.5$ and $M = 1$, but the sign of the difference is swapped between low-speed and high-speed jets. At low speed the hot jet is noisier, but at high speed the isothermal jet is noisier. This trend can be explained by considering how the momentum and enthalpy sources are affected by temperature and velocity.

The momentum term is reduced for the hot jet due to the lower density, whereas the enthalpy term increases with temperature due to increases of enthalpy in the jet plume. The trends indicate therefore that the enthalpy term dominates sound emission at low speed, whereas the momentum term dominates at high speed. This interpretation also explains the different scaling with velocity, highlighted in Fig. 6.9; the isothermal jet scales with U_J^8 and the hottest jet with U_J^6. The effect on intermediate temperatures is not so clear for the QinetiQ1983 dataset at higher Mach numbers, but it is so for the results of QinetiQ2009 dataset analysed in the next section.

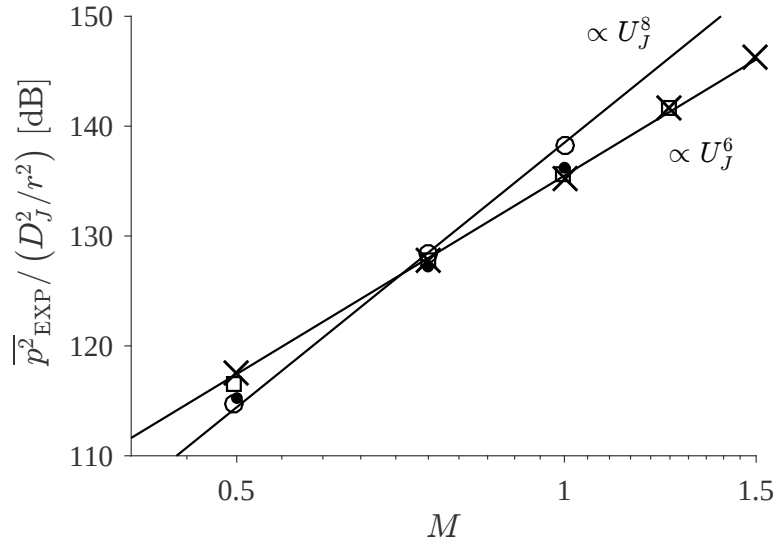

FIGURE 6.9: Measured mean square pressure at $\theta = 90^\circ$ for subsonic jets from QinetiQ1983 dataset [60]. Circles, $T_R = 1$; dots, $T_R = 1.5$; squares, $T_R = 2$; crosses, $T_R = 2.5$. Lines show that the hottest jets follow trend with U_J^6, whereas isothermal jets follow U_J^8.

Results from the QinetiQ2009 dataset

The same analysis of the QinetiQ1983 dataset is performed for more recent measurements taken in 2009. Narrowband data are also available for these measurements, which are used for the analysis of the farfield spectrum in Section 6.4. The results of the QinetiQ2009 dataset show more clearly the effect of intermediate temperature ratios than the QinetiQ1983 dataset. Figure 6.10 confirms that the hottest jet follows a trend with U_J^6, whereas the isothermal jet follows as U_J^8 trend. For intermediate temperatures, the trends is between these two extremes.

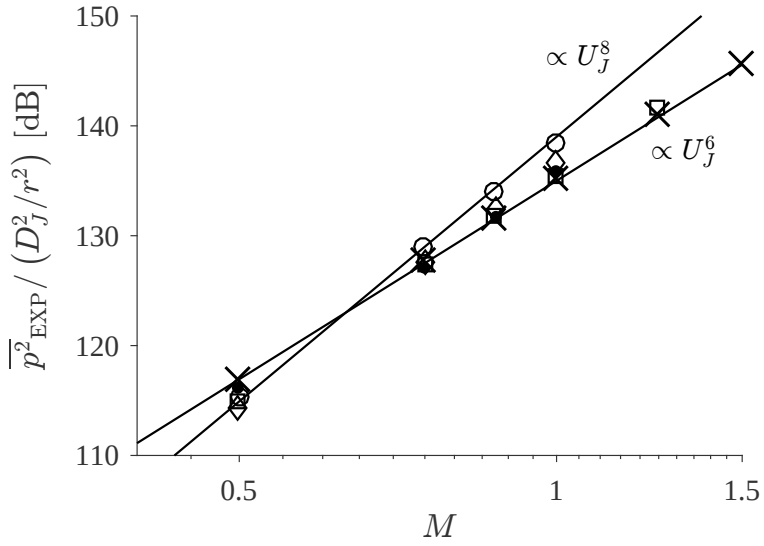

FIGURE 6.10: Measured mean square pressure at $\theta = 90^\circ$ for subsonic jets from QinetiQ2009 dataset [62]. Circles, $T_R = 1$; diamonds, $T_R = 1.25$; dots, $T_R = 1.5$; squares, $T_R = 2$; crosses, $T_R = 2.5$. Lines show that the hottest jets follow trend with U_J^6, whereas isothermal jets follow U_J^8.

6.3.2 Scaling with nozzle-exit values

The trends with velocity in Figs. 6.9 and 6.10 indicate that the theoretical dependence of the momentum and enthalpy sources with velocity agrees with experiment. A further assessment can be made by scaling the mean square pressure with the dimensional analysis derived from the theoretical model. This is done by dividing the measured data ($\overline{p^2}_{\mathrm{EXP}}$) by the mean square pressure derived in Section 4.1.1 (see Eq. (4.38)), $\overline{p^2}_{\mathrm{NE}}$.

The result of the scaling of the QinetiQ1983 dataset is shown in Fig. 6.11 (a constant factor is used for all cases to shift the dB scale to zero). The empirical coefficients of the scaling law (Eq. (4.38)) are set to $\alpha_M = \alpha_H = 1$. The reduction of density in the $T_R = 2.5$ jet reduces the contribution from the momentum source by approximately 8dB, which is then balanced by the increase in the contribution from the enthalpy source. The fact that the range of more than 30dB in the experimental data is collapsed within approximately $\pm$1.5dB for both isothermal and hot jets corroborates the need for an additional source component in hot jet as pointed by Morfey [17].

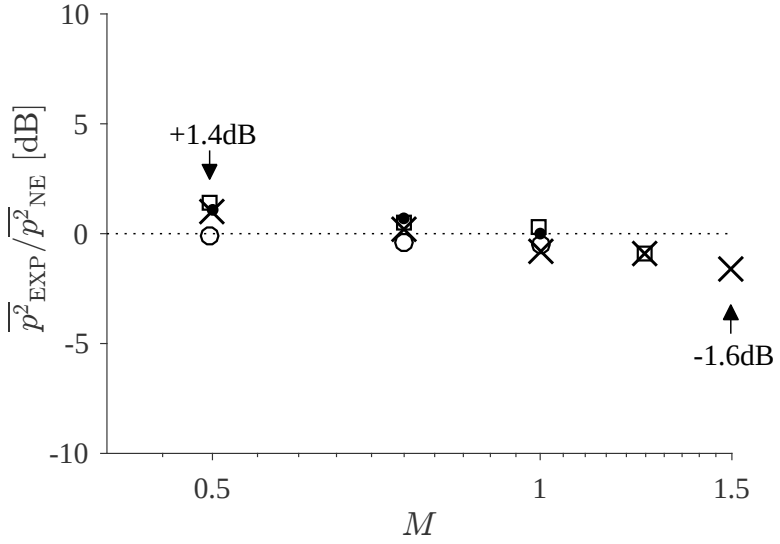

FIGURE 6.11: Measured mean square pressure at $\theta = 90^\circ$ from QinetiQ1983 dataset scaled by nozzle-exit scaling law (Eq. (4.38)). Arrows indicate location of maximum and minimum difference from the average of 35.8dB. Same symbols as Fig. 6.9.

The scaling of mean square pressure from the QinetiQ2009 dataset is shown in Fig. 6.12 (also considering $\alpha_M = \alpha_H = 1$). The results for the lowest and highest Mach numbers being somewhat worse than the results for the QinetiQ1983 data, showing a maximum deviation from the mean slightly over 2dB. However, the accuracy near the range of interest for civil aviation, $0.7 < M < 1$, is optimum.

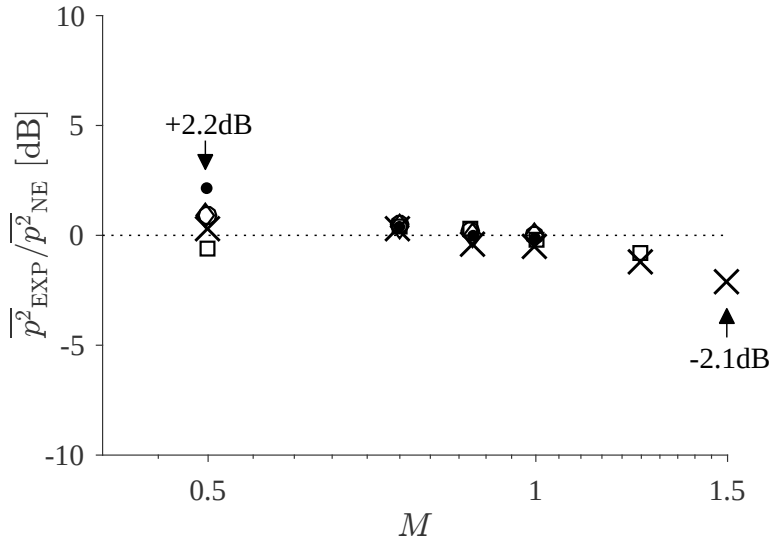

FIGURE 6.12: Measured mean square pressure at $\theta = 90^\circ$ from QinetiQ2009 dataset data scaled by nozzle-exit scaling law (Eq. (4.38)). Arrows indicate maximum and minimum difference from the average of 35.5dB. Same symbols as Fig. 6.10.

6.3.3 Effect of flow factor in hot jets

The worst results of the scaling for the QinetiQ2009 dataset (Fig. 6.12) are for hot jets. At $\theta = 90^\circ$ the effect of flow–acoustic interaction is negligible for isothermal jets, but the effect if significant for hot jets. So a flow factor is applied in this section to correct the scaling for the hot jets.

The flow factor applied in this section is derived from the high-frequency solution of the Primdore-Brown operator as presented by Tester and Morfey [68, 69]. To be consistent with the formulation used by Tester and Morfey, the source description follows the Lilley–Goldstein acoustic analogy [9, 16]. So, the quadrupole and dipole sources are the velocity-quadrupole and temperature-dipole presented in Section 4.1.3.

The flow factor is applied as a correction for the nozzle-exit scaling of the mean square pressure in the farfield. The flow factor for the quadrupole and dipole sources at $\theta = 90^\circ$ may thus be written as [69]:

$$F^q = \frac{\rho_J}{\rho_0}\left(\frac{a_J}{a_0}\right)^{-4}, \tag{6.1}$$

and

$$F^d = \frac{\rho_J}{\rho_0}\left(\frac{a_J}{a_0}\right)^{-2}. \tag{6.2}$$

The flow factors may be written as a function of temperature ratio as:

$$F^q = T_R^{-3}, \tag{6.3}$$

and

$$F^d = T_R^{-2}. \tag{6.4}$$

The scaling of the farfield mean square pressure accounting for the flow factor is written as

$$\overline{p^2}_{\mathrm{NE,FF}} = \alpha_q F^q \overline{(p^q)^2} + \alpha_d F^d \overline{(p^d)^2}. \tag{6.5}$$

in which $\overline{(p^q)^2}$ is the scaling law for the velocity-quadrupole,

$$\overline{(p^q)^2} \sim \frac{D_J^2}{r^2 a_0^4 T_0^2} U_J^8; \tag{6.6}$$

and $\overline{(p^d)^2}$ is the scaling law for temperature-dipole,

$$\overline{(p^d)^2} \sim \frac{D_J^2}{r^2 a_0^2 T_0^2}\left(\frac{T_J - T_0}{T_J}\right)^2 U_J^6; \tag{6.7}$$

and α_q and α_d are adjustable coefficients.

Figure 6.13 shows the scaling of the QinetiQ2009 dataset using the flow factor and the source terms from the Lilley–Goldstein analogy [9, 16] written for a homogeneous base flow (see Section 4.1.3). For this scaling the empirical coefficients were $\alpha_q = 1$ and $\alpha_d = 6.7$, resulting in scatter of approximately ± 1.0dB after ignoring the outlier point at $M = 0.5$. The application of the flow factor and using the quadrupole source from the Lilley–Goldstein-based formulation instead of the formulation of Section 2.1 reduced the scatter and the trend with Mach number observed in the results of Fig. 6.12.

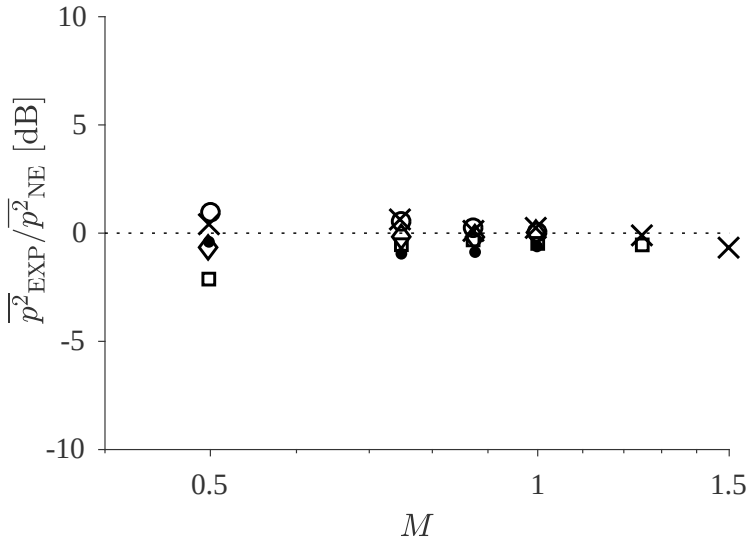

FIGURE 6.13: Measured mean square pressure at $\theta = 90^\circ$ from QinetiQ2009 dataset scaled with the scaling law that accounts for flow factor of the velocity-quadrupole and temperature-dipole sources (see Section 4.1.3). Same symbols as Fig. 6.10.

6.3.4 Scaling with RANS k–ε input

Returning to the scaling law discussed in Section 6.3.2, the scaling of the mean square pressure for the QinetiQ2009 dataset is now computed using information about the entire jet plume from a RANS k–ε simulation. The solution is obtained from a commercial RANS solver with a standard k–ε turbulence model (more information about the RANS k–ε solution is presented in Appendix B). The scaled results are the experimental mean square pressure divided by the mean square pressure scaling from Eq. (4.45). The analysis in this section is limited to the the cases with temperature ratio $T_R = 1$, $T_R = 1.5$, and $T_R = 2.5$, and acoustic Mach number $M = 0.5$, $M = 0.75$, and $M = 1$. The analysis of this section uses fewer cases than the nozzle-exit scaling of Section 6.3.2, but considers the same range of temperature ratios.

Results in Fig. 6.14 show a collapse of an experimental range of approximately 25dB to $\pm$1.5dB. Although the scatter of the collapsed data is small, there is a trend with temperature and Mach number. The trend with temperature could be corrected via adjustment of the coefficients α_M and α_H, which were considered $\alpha_M = \alpha_H = 1$ for these results, and the trend with Mach number could be corrected with the application

of a flow factor for the hot jets.

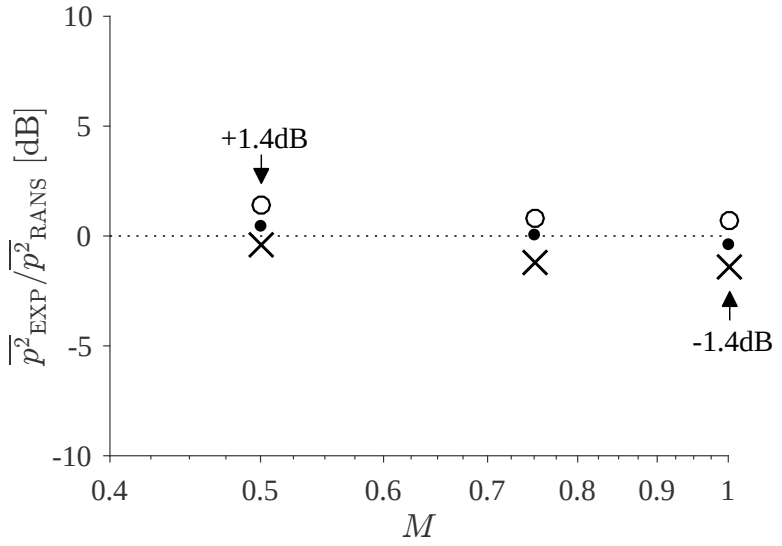

FIGURE 6.14: Measured mean square pressure at $\theta = 90^\circ$ from QINETIQ2009 dataset scaled with RANS-based scaling (Eq. (4.45)). Circles, $T = 1$; dots, $T_R = 1.5$; crosses, $T_R = 2.5$.

6.4 Prediction of the farfield autospectral density

The method presented in Chapter 4 is used to predict the farfield spectrum for cases of the QinetiQ2009 dataset. The mean flow for these jets was computed with a commercial RANS solver with standard k–ε turbulence model. The calibration coefficients of the source model were computed by matching predictions with measurements at $\theta = 90^\circ$ of two operating conditions: the highest-speed/lowest-temperature ($M = 1$, $T_R = 1$) and lowest-speed/highest-temperature ($M = 0.5$, $T_R = 2.5$) jets. The experimental data and predictions used for calibration are shown in Fig. 6.15. The empirical coefficients take the values shown in Table 6.2.

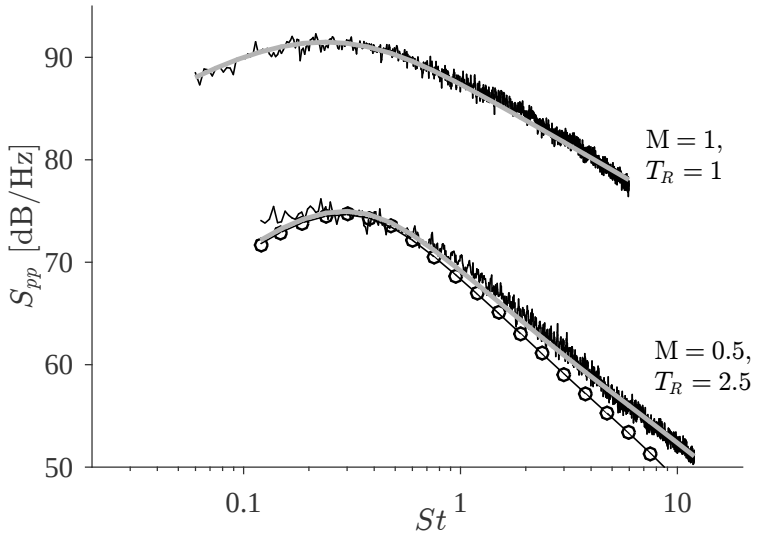

FIGURE 6.15: Farfield pressure spectra at $\theta = 90^\circ$ used for calibration of the momentum and enthalpy sources. Black lines, measured spectra; thick grey lines, total prediction; line with circles, contribution from the enthalpy component. Contribution from the momentum term not distinguishable from the total prediction for the isothermal jet, and not shown for the hot jet.

TABLE 6.2: Empirical coefficients.

$\alpha_{\tau,m}$	$\alpha_{\ell,m}$	$\alpha_{k,m}$	$\alpha_{\tau,h}$	$\alpha_{\ell,h}$	$\alpha_{k,h}$
1.03	0.40	1	0.68	0.53	9.61

The empirical coefficient of amplitude for the momentum term, $\alpha_{k,m}$, takes the value 1, which makes this coefficient redundant. Yet, the coefficient is kept in the model to emphasize that an empirical relation between the magnitude of the momentum term and the RANS k–ε solution is considered.

Figure 6.16 confirm that the momentum source is sufficient to predict the noise from isothermal subsonic jets. The predictions agree well with measured data, showing the same agreement of the results by Ilário et al. [10].

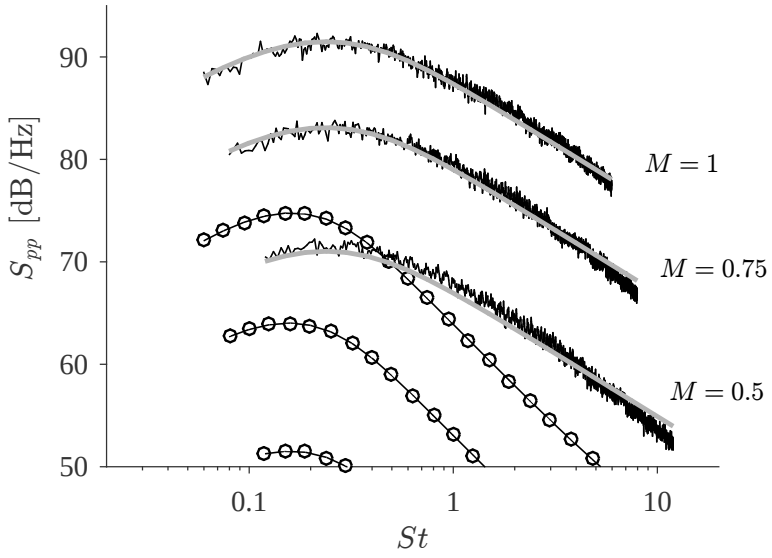

FIGURE 6.16: Predictions of the farfield pressure spectrum at $\theta = 90^\circ$ for isothermal jets. Thick grey lines, total prediction; lines–circles, enthalpy component; thin lines, measurements. Contribution from the momentum component is not distinguishable from the total prediction.

Figure 6.17 shows the results for the hot jets with $T_R = 2.5$. It is shown that the enthalpy component is dominant for all the three jet speed at this temperature ratio. The increase of the enthalpy source with jet speed follows the experimental trends, although a slight overprediction at the highest velocity is observed. The overprediction might be due to the neglect of flow–acoustic interaction effects, shown to be significant for hot jets even at $\theta = 90^\circ$ (see Section 6.3.3).

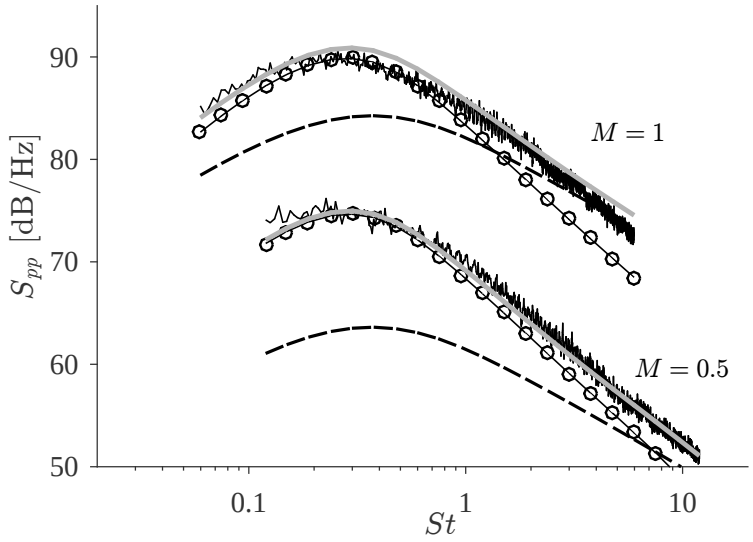

FIGURE 6.17: Predictions of the farfield pressure spectrum at $\theta = 90^\circ$ for $T_R = 2.5$ jets. Thick grey lines, total prediction; dashed lines, momentum component; lines-circles, enthalpy component; thin lines, measurements.

Figure 6.18 shows that despite the approximations of the model the error for all nine cases is within a $\pm$2dB margin. However, these results are limited for $\theta = 90^\circ$. For other polar angles, the assumptions about isotropy and source compactness play a more significant role so the predictions deteriorate significantly.

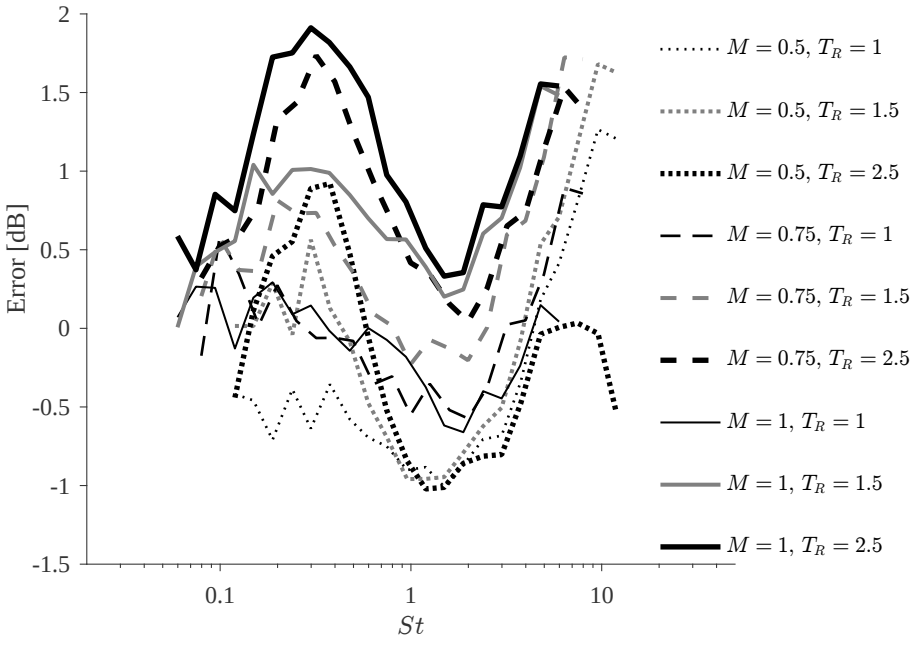

FIGURE 6.18: Difference between predictions of the farfield pressure spectrum at $\theta = 90^\circ$ and measurements for all nine cases is within $\pm$2dB.

Chapter 7

Results — validation of the cross-spectral density model

This chapter analyses turbulence statistics in the jet plume to assess the empirical model for the cross-spectral density. Large eddy simulation data for two jets with acoustic Mach number of 0.88 are considered; one for an isothermal jet and another for a hot jet with temperature ratio of 2.5.

The empirical method for the cross-spectral density described in Chapter 5 is based on the model by Harper-Bourne [12]. The results in this chapter validate Harper-Bourne's coherence model for transverse velocity fluctuations and assess the new models for the autospectral density and length scale spectrum.

Sections 7.1 and 7.2 present supporting results for the assessment of the method. Some assumptions used by the empirical model are assessed in Section 7.1 and In Section 7.2 the integral length scale—needed by the empirical model of cross-spectral density—is computed on the lipline of the isothermal and hot jets.

7.1 Assumptions of the model

The formulation using the cross-spectral density removes the assumption of isotropic turbulence and of compact sources used for the formulation in Chapter 4, but the neglect of the shear source and of thermodynamic fluctuations are still considered. Two

additional assumptions related to turbulence statistics were introduced: that the autospectral density is constant within a volume of coherent turbulence, and that Taylor's hypothesis is valid in the jet lipline. These assumptions are assessed in the following two sections using unsteady data in the jet lipline from large eddy simulations.

7.1.1 Constant autospectral density within volume of coherent turbulence

The autospectral density is assumed independent of space separation in the model of cross-spectral density. The simplification may be written as

$$\sqrt{S(\mathbf{x},\omega)S(\mathbf{x}+\mathbf{s},\omega)} \approx S(\mathbf{x},\omega). \tag{7.1}$$

In this section the results from large eddy simulation are used to compute $S(\mathbf{x},\omega)S(\mathbf{x}+\mathbf{s},\omega)$ and $S(\mathbf{x},\omega)$ in order to assess the simplification.

The approximation becomes worse as the space separation increases, but as the coherence decays with increasing separation the relevance of the error is reduced. So for a more significant assessment of the simplification, the values are compared for a separation where the coherence is still significant.

An axial separation of $s_1 = 0.5D_j$ and radial separation of $s_2 = 0.1875D_j$ are considered for a point on the lipline and $x_1 = 5D_j$. Figure 7.1 shows that the coherence of u_1 for these axial and radial separation is significant. The vertical line in Fig. 7.1 shows the maximum resolved frequency of the large eddy simulation at $St = 2$ (more information in Appendix A).

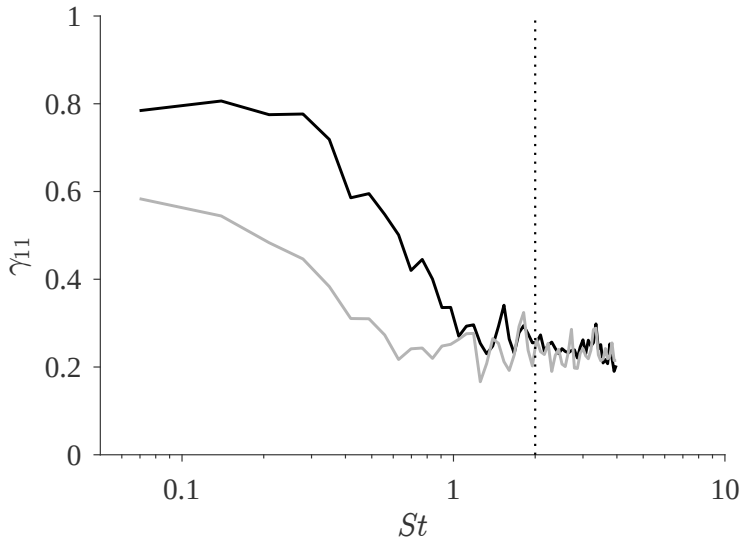

FIGURE 7.1: Coherence function of u_1 with axial (black line) and radial (grey line) separation. Axial separation is $s_1 = 0.5D_J$; radial separation is $s_2 = 0.1875D_J$. Results for the isothermal jet ($M = 0.88$, $T_R = 1$). Computed using a time series from LES data on the lipline and axial location of $x_1 = 5D_J$.

To asses the simplification, the autospectral density of u_1 is computed at three locations: $\mathbf{x}$, $\mathbf{x} + (s_1, 0, 0)$, and $\mathbf{x} + (0, s_2, 0)$. Figure 7.2 shows that the approximation is worse for radial separations, which is expected given the lower coherence for this radial separation. However, the errors are small enough to be neglected, given the simplification of the formulation enabled by the assumption.

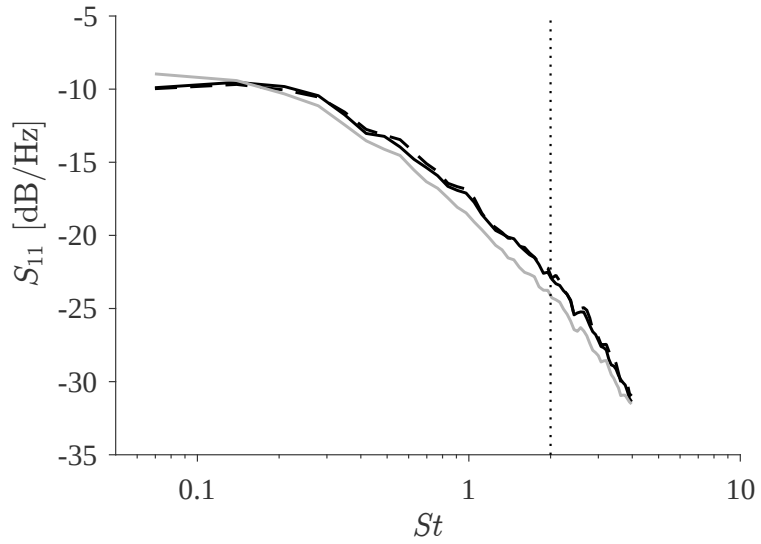

FIGURE 7.2: Autospectral density at reference location (dashed line), with axial separation of $s_1 = 0.5D_J$ (black continuous line), and radial separation separation of $s_2 = 0.1875D_J$ (grey line). Results for the isothermal jet ($M = 0.88$, $T_R = 1$). Computed using a time series from LES data on the lipline and axial location of $x_1 = 5D_J$.

7.1.2 Taylor's hypothesis

Taylor's hypothesis is assessed for the isothermal and hot jets in the lipline. The hypothesis assumes that a space separation of s_1 in the space-time correlation is equivalent to a time separation of $s_1/\overline{U}_1(\mathbf{x})$.

Figures 7.3 and 7.4 show the results for the isothermal and hot jets, respectively. The results are computed at locations before and after the potential core of each case, showing that the hypothesis is valid in the entire region of interest for jet noise (if assumed the sources are located on the lipline).

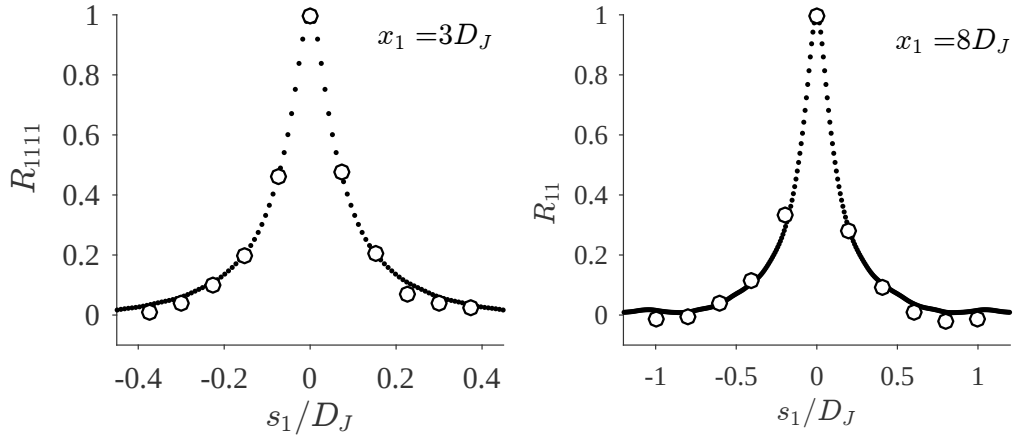

FIGURE 7.3: Space–time correlation of u_1^2 in the lipline of the isothermal jet ($M = 0.88$, $T_R = 1$) at different axial locations ($x_1 = 3D_J$ and $x_1 = 8D_j$). Dots, non-zero separation in time $R_{1111}(\mathbf{x}; s_1 = 0; \tau = s_1/\overline{U}_1(\mathbf{x}))$; white-filled circles, non-zero separation in space $R_{1111}(\mathbf{x}; s_1; \tau = 0)$. Computed using a time series from LES data.

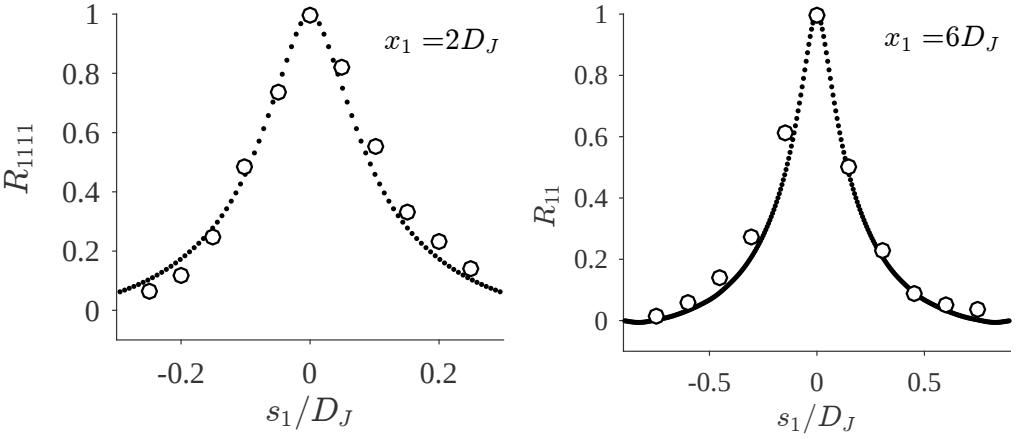

FIGURE 7.4: Same as Fig. 7.3 but for the hot jet ($M = 0.88$, $T_R = 2.5$).

By validating Taylor's hypothesis the integral length scale can be computed using the correlation with time separation and the model by von Kármán [47], which was proposed for the unidimensional wavenumber spectrum of turbulence, may be used to compute the frequency spectrum.

7.2 Integral length scale

The empirical model for the cross-spectral density uses the local integral length scale of turbulence to compute the autospectral density and the coherence function. In this

section the large eddy simulation is used to compute the integral length scale on the lipline of the isothermal and hot jets. The evolution with axial coordinate is compared between the isothermal and hot jets for the integral length scale of u_i and of u_i^2.

The integral length scale of turbulence, introduced in Section 2.2.2, is computed from the correlation function of axial and radial velocity components. With Taylor's hypothesis validated, the integral length scale is computed by integrating the correlation function in time with zero space separation.

Figure 7.5 shows the length scale for the axial velocity components. Results are shown for u_1 and u_1^2 for both isothermal and hot jets. It can be seen that the integral length scale grows approximately linearly with axial distance, and that the slope scales with the potential core length. The level, however, is slightly higher for the hot jet.

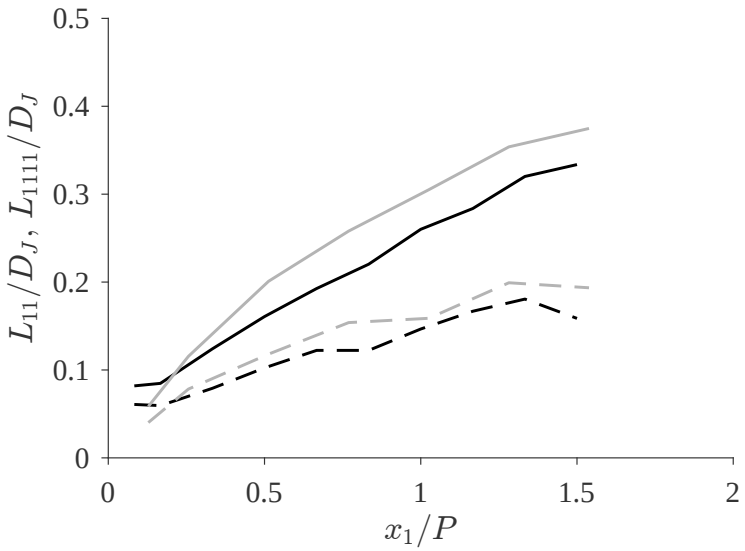

FIGURE 7.5: Integral length scales for u_1 (continuous lines) and u_1^2 (dashed lines). Computed using a time series from the LES data on the lipline. Black lines, isothermal jet ($M = 0.88$, $T_R = 1$); grey lines, hot jet ($M = 0.88$, $T_R = 2.5$).

Figure 7.6 compares the length scale for the radial and axial velocity components. The behaviour again is self-similar for the hot and isothermal jets if the axial coordinate is scaled by the potential core length. In the initial region of jet the ratio between radial and axial components does not follow a particular trend, but downstream the ratio approaches 0.5. It is shown that the ratio between the radial and axial components

for the squared velocity are slightly closer to unity as the squared velocity is more isotropic.

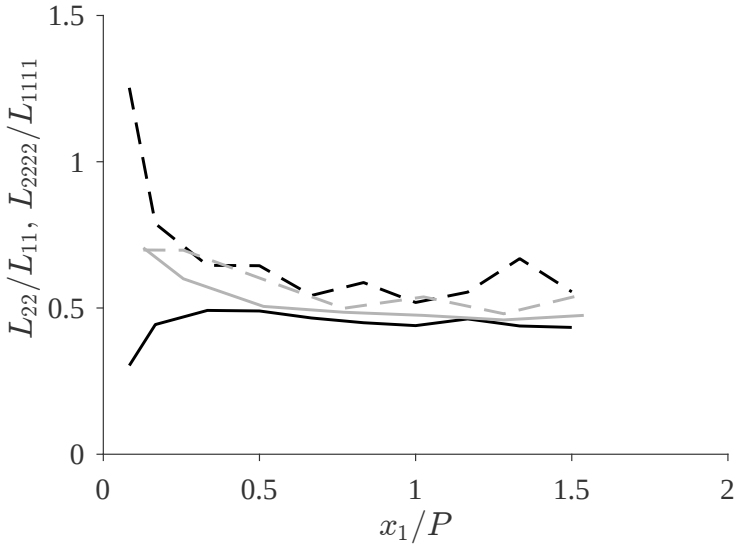

FIGURE 7.6: Ratio of integral length scales between radial and axial components of velocity. Computed using a time series from LES data on the lipline.. Continuous lines, L_{22}/L_{11}; dashed lines, L_{2222}/L_{1111}. Black lines, isothermal jet ($M = 0.88$, $T_R = 1$); grey lines, hot jet ($M = 0.88$, $T_R = 2.5$).

7.3 Autospectral density

Taylor's hypothesis enables the use of a model for the unidimensional wavenumber spectrum of turbulence to compute the autospectral density (or frequency spectrum). Thus the empirical function by von Kármán [47], written for the unidimensional wavenumber, k_1, can be used to compute the frequency spectrum by writing $k_1 = \omega/\overline{U}_1$. In this section the autospectral density of u_i and of u_i^2 is analysed on the lipline and compared with the von Kármán spectrum. The results are compared for the isothermal and hot jets.

Figure 7.7 shows the autospectral density of u_1 for different axial stations in the lipline. The arrow indicates that with growing axial location the behaviour is different at low and high frequencies. At low frequency, the level of the spectrum grows with axial coordinate. Owing to the approximately constant turbulent kinetic energy and mean axial velocity on the lipline, the growth in the low frequency is mostly due to

the growth of the integral length scale. The effect at high-frequency is also due to the growth in integral length scale, but with opposite effect. The growth in integral length scale reduces the time scale which defines the cut-off frequency where spectrum starts to decay; so the growth in the integral length scale reduces the autospectral density at high frequency.

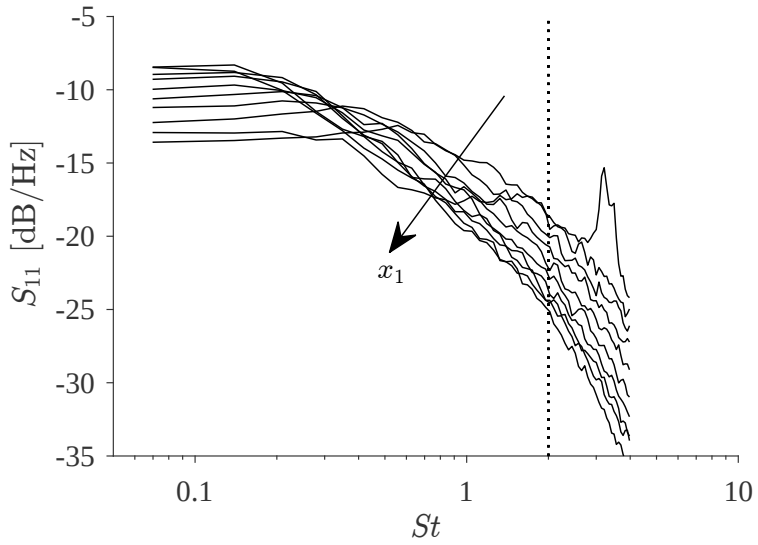

FIGURE 7.7: Autospectral density of u_1 on the lipline for axial locations $0.5D_J < x_1 < 9D_J$. Solid lines, autospectral density computed from the LES data of an isothermal jet ($M = 0.88$, $T_R = 1$); vertical dotted line, highest resolved-frequency of LES. The arrow indicates the effect of increasing the axial location.

The model for the autospectral density (Eqs. (5.13) and (5.15)) predicts the behaviour observed in Fig. 7.7. Figure 7.8 shows the results for the isothermal jet at different axial stations on the lipline. The agreement is optimum at intermediate frequencies, approximately in the range $0.2 < St < 1$. This is also the range of peak jet noise and where the numerical simulation is of higher accuracy. Results in Fig. 7.9 show that the model is also valid for the hot jet.

For the results shown in Figs. 7.8 and 7.9 the mean square value of turbulent fluctuations and the integral length scale of the source terms were computed locally from the numerical solution. In a RANS-based prediction scheme, these scales would be computed from the turbulent kinetic energy and turbulence dissipation rate.

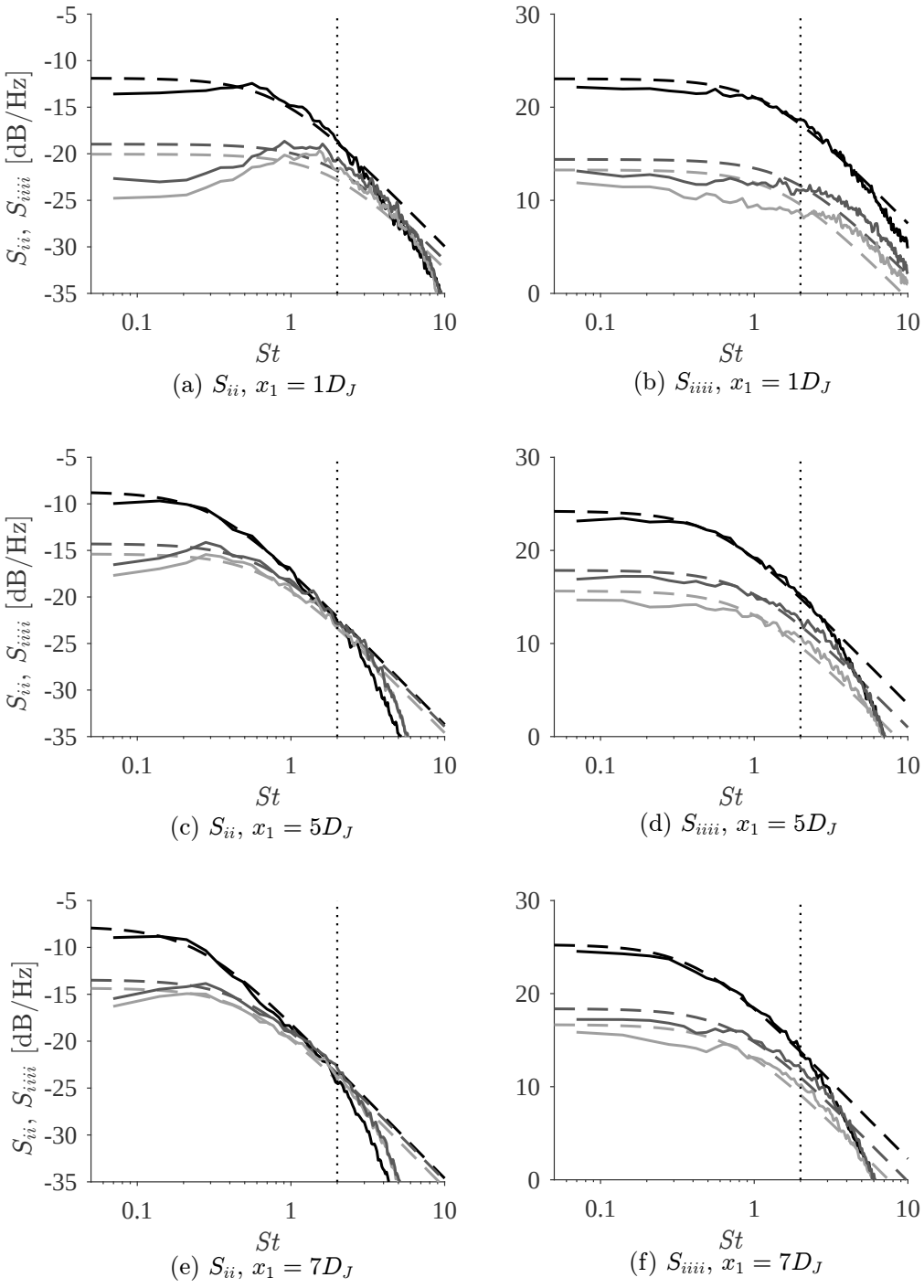

(a) S_{ii}, $x_1 = 1D_J$ (b) S_{iiii}, $x_1 = 1D_J$

(c) S_{ii}, $x_1 = 5D_J$ (d) S_{iiii}, $x_1 = 5D_J$

(e) S_{ii}, $x_1 = 7D_J$ (f) S_{iiii}, $x_1 = 7D_J$

FIGURE 7.8: Autospectral density of u_i (a, c, e) and of u_i^2 (b, d, f) of an isothermal jet ($M = 0.88$, $T_R = 1$). Continuous lines, computed from LES data divided by 5π; dashed lines, model fit; vertical dotted line, LES cut-off frequency. Black lines, axial component; dark-grey lines, azimuthal component; light-grey lines, radial component.

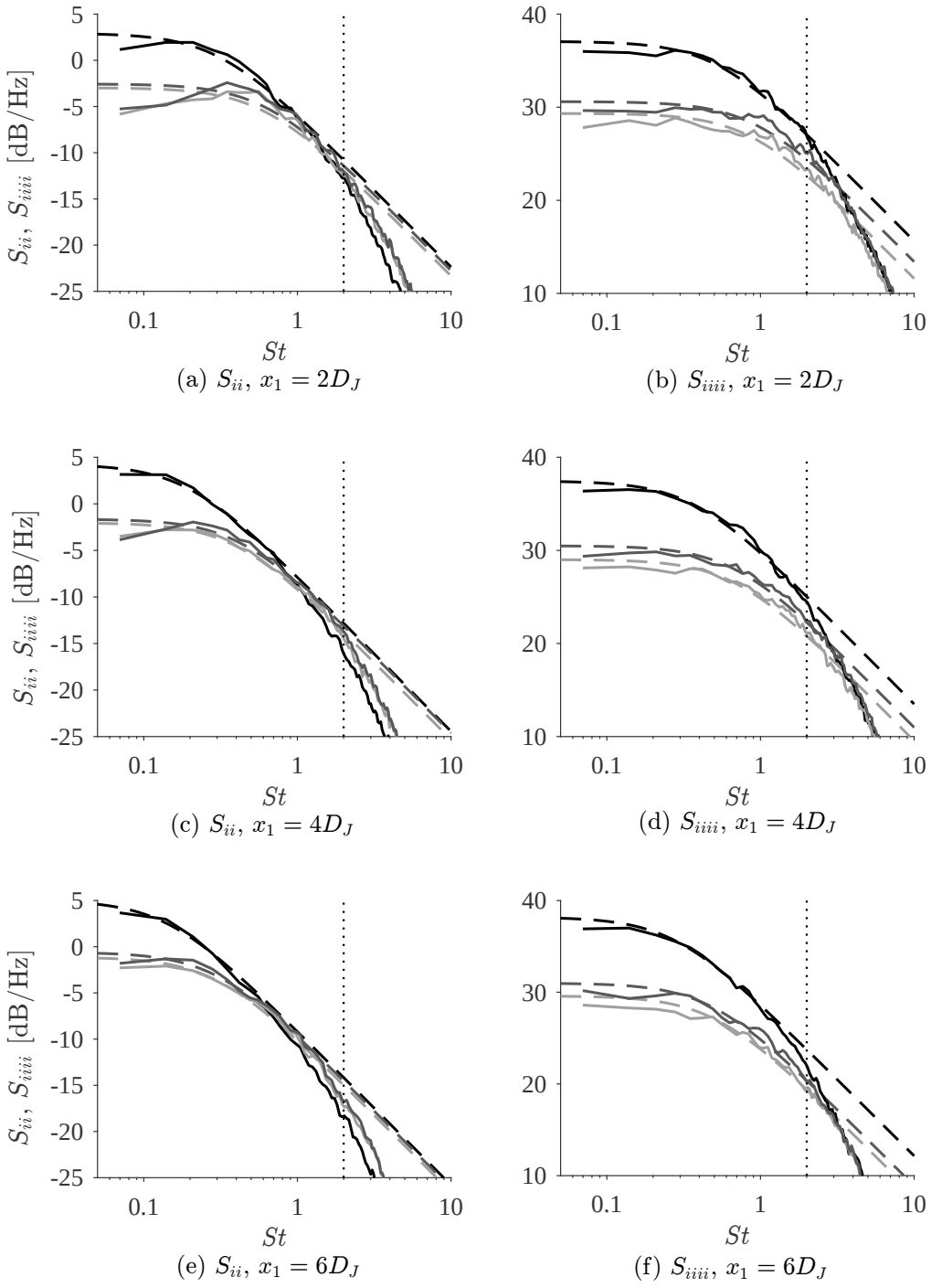

FIGURE 7.9: Same as Fig. 7.8, but for a hot jet ($M = 0.88$, $T_R = 2.5$).

7.4 Coherence length scale at low frequency

The large eddy simulation has a limited frequency resolution due to grid size and total running time. The coherence function combines separation in space and time, so the

short running time limits the computation of coherence to a more narrow range of frequencies than the autospectral density. Therefore, the large eddy simulation can be used only to compute the coherence length scales at low frequency.

In this section the coherence is studied in the frequency range $0.28 < St < 0.56$. Despite the limited range, this is the peak frequency of jet noise, so the analysis is relevant for jet noise prediction.

Figures 7.10 and 7.11 show the coherence decay with axial separation for the axial velocity component and for the radial velocity component, respectively. The figures present results for three frequencies in the range $0.28 < St < 0.56$ and 10 axial locations on the lipline. The separation distance for each axial location is scaled by the local integral length scale. The results show, therefore, that the evolution of the coherence is self-similar with the local integral length scale.

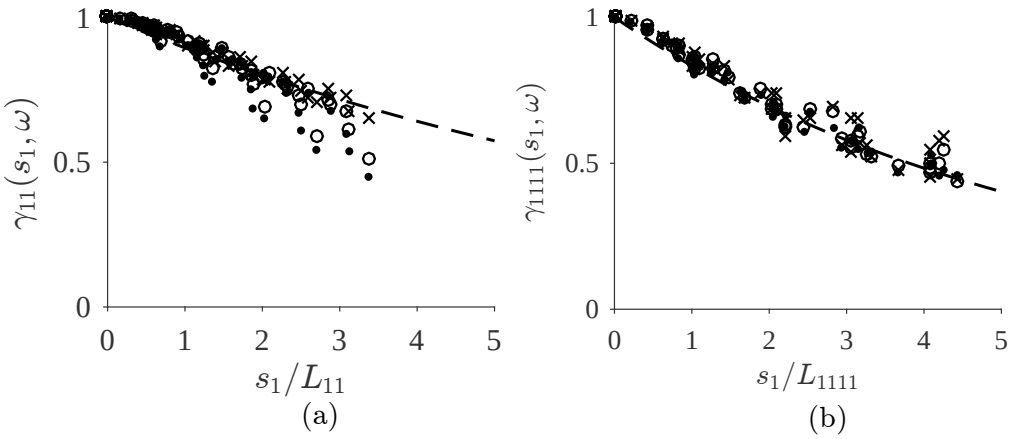

FIGURE 7.10: Coherence decay of (a) u_1 and (b) u_1^2 with axial separation on the lipline of the isothermal jet ($M = 0.88$, $T_R = 1$). Results for three frequencies: $St = 0.28$ (crosses), $St = 0.42$ (circles), and $St = 0.56$ (dots). Dashed lines: $\exp(-s_1/9L_{11})$ in (a), and $\exp(-s_1/5.5L_{1111})$ in (b). Axial locations are $D_J < x_1 < 9D_J$. Computed using a time series from LES data on the lipline.

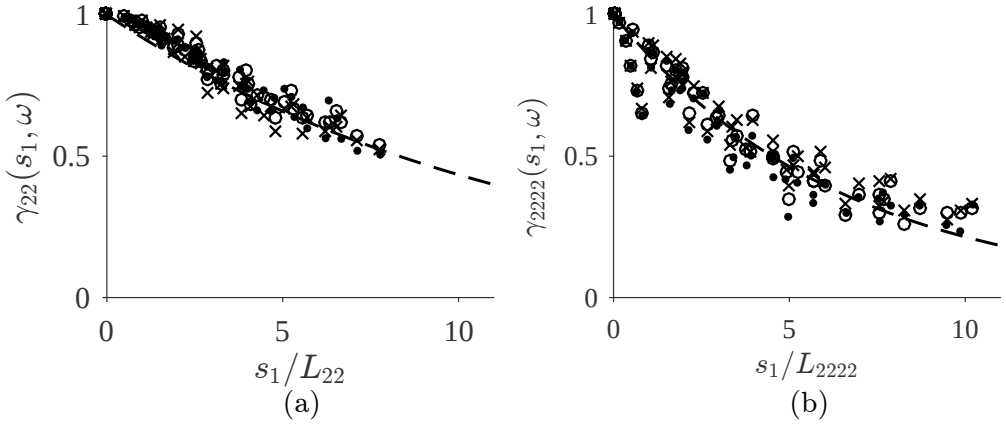

FIGURE 7.11: Coherence decay of (a) u_2 and (b) u_2^2 with axial separation on the lipline of the isothermal jet ($M = 0.88$, $T_R = 1$). The exponential decay of the dashed lines are: $\exp(-s_1/12L_{22})$ in (a), and $\exp(-s_1/6.5L_{2222})$ in (b). Computed using a time series from LES data on the lipline.

It was shown in Section 7.2 that the integral length scale is self-similar with potential core length for the isothermal and hot jets, and that it grows linearly with axial coordinate. So from the results of Fig. 7.10 and 7.11 it is concluded that the coherence length scale also grows linearly with axial coordinate and is self-similar with potential core length for hot jets.

The agreement of the exponential decay plotted in Figs. 7.10 with the data confirms the model for the coherence function proposed by Harper-Bourne [12]. The analysis by Harper-Bourne was, however, limited to the axial velocity fluctuation due to the limitations of the hotwire equipment. Figure 7.11 shows that the coherence of the radial velocity fluctuations has the same behaviour, thus validating Harper-Bourne's model for the radial velocity fluctuations.

The coherence decay in Figs. 7.10 and 7.11 is scaled by the local integral length scale of each velocity component. The ratio between the coherence decay and integral length scale is slightly higher for the radial velocity. For instance, the coherence length scale for u_2^2 is $6.5L_{2222}$, whereas for u_1^2 it is $5.5L_{1111}$. But as $L_{1111} > L_{2222}$, the coherence length scale of the radial velocity is smaller than the coherence length scale of the axial component.

7.5 Coherence length scale — model for the spectrum

A model for the coherence length scale spectrum was introduced in Section 5.1.3. Due to the limited range of the large eddy simulation, it cannot be assessed with numerical data. The assessment is performed, therefore, using the hotwire data published by Morris and Zaman [53].

The length scale spectrum was measured by Morris and Zaman for coherence of u_1 with axial, radial and azimuthal separations. The measurements were taken $x_1 = 5D_J$, which is approximately at the end of the potential core. The prediction with the new model is shown along measured data of the length scale spectrum in Fig. 7.12. It is observed that the length scaled with axial separation, $\ell_{11,1}$, is the largest; the length scale with azimuthal separation, $\ell_{11,3}$, is the second largest and the radial, $\ell_{11,2}$ is the smallest. The agreement of the new model is remarkable, so its application is suggested for a prediction scheme.

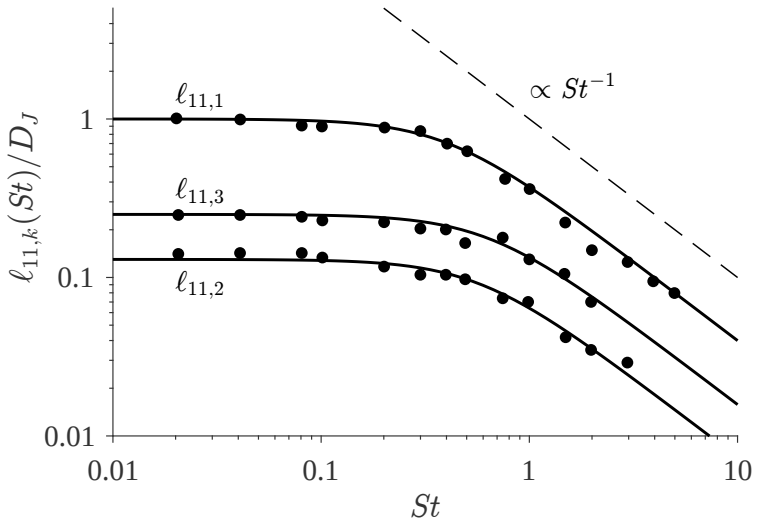

FIGURE 7.12: Spectrum of the coherence length scales for squared axial velocity on the lipline of unheated jet ($M = 0.25$, $T_R \approx 1$). Symbols, data from Morris and Zaman [53]; continuous lines, model fit; dashed line, slope at high frequency. $\ell_{11,1}$ is the length scale of u_1^2 with axial separation; $\ell_{11,2}$ with radial separation; and $\ell_{11,3}$ with azimuthal separation.

7.6 Effect of phase delay

Harper-Bourne [12] observed that the phase speed of turbulent fluctuations vary with frequency. Yet, it was considered in this thesis that the phase speed can be assumed independent of frequency and equal to the mean axial velocity, in the form:

$$\phi(x_1, s_1, \omega) = \frac{\omega s_1}{\overline{U}_1(x_1)}, \tag{7.2}$$

In this section this assumption is corroborated using data from a large eddy simulation.

Figure 7.13 shows the real part of the phase of radial squared velocity fluctuations (u_2^2). In Fig. 7.13 (b) it is shown that the phase scales well with $\omega s_1/\overline{U}_1(x_1)$, confirming an approximate phase speed of $\overline{U}_1$. The phase delay tends to zero at low frequency, so that errors in the phase speed are small when the cosine of the phase is taken.

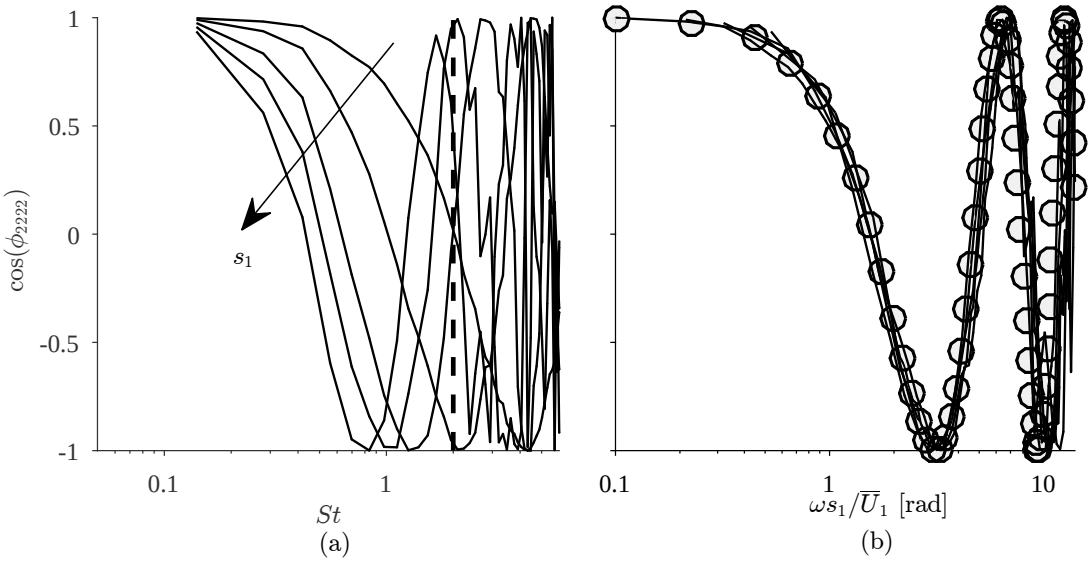

FIGURE 7.13: Effect of axial separation on the phase of u_2^2; results on the lipline and $x_1 = 3D_J$ of isothermal jet ($M = 0.88$, $T_R = 1$). In (a), the horizontal axis is the Strouhal number; in (b) it is $\omega s_1/\overline{U}_1$. Continuous lines, computed from LES; circles, $\cos(\omega s_1/\overline{U}_1)$. The vertical line at $St = 2$ denotes the LES cut-off frequency.

A similar behaviour is observed for the phase of velocity fluctuation, which is relevant to the enthalpy term. The comparison of the phase of u_2^2 and u_2 at $x_1 = 3D_J$ of the hot jet is shown in Fig. 7.14.

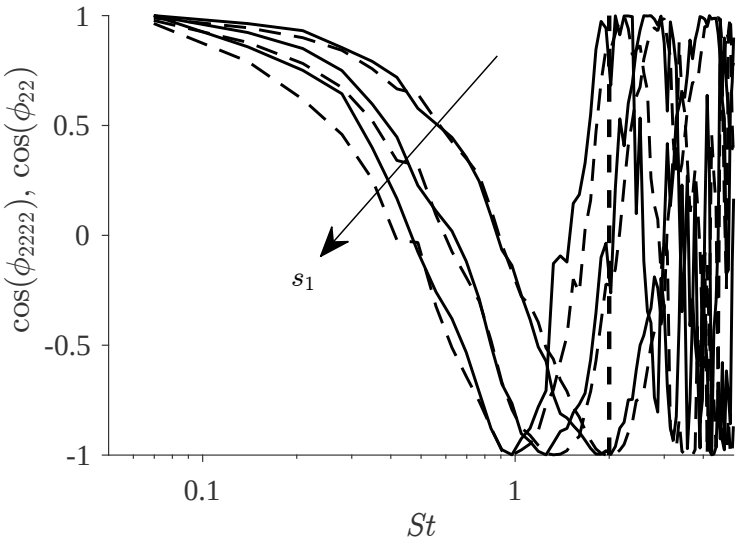

FIGURE 7.14: Phase of u_2^2 and u_2 show similar behaviour. Result from $x_1 = 3D_J$ of the hot jet ($M = 0.88$, $T_R = 2.5$) computed using a time series from LES data. Arrow indicate growing axial separation distance. The vertical line at $St = 2$ denotes LES cut-off frequency.

Chapter 8

Results — applications of the cross-spectral density model

The formulation based on a model for the cross-spectral density presented in Chapter 5 is applied in this chapter to predict the effects of turbulence anisotropy and of source non-compactness. In Section 8.1 turbulence anisotropy is computed from large eddy simulation and the farfield directivity due to anisotropy is predicted using the formulation of Chapter 5. Section 8.2 infers the length scale spectrum in different location on the lipline from the measurements by Morris and Zaman [53]; the new model for the length scale spectrum and the formulation based on the cross-spectral density are used to predict the effects of source non-compactness on the farfield autospectral density.

8.1 Effect of turbulence anisotropy on jet noise directivity

Jet noise directivity is a result of source anisotropy and the effects of flow–acoustic interaction. For moderate polar angles (θ) in the rear arc, say $90^\circ < \theta < 70^\circ$, the spectrum is amplified as the polar angle is reduced but its shape is not significantly changed (see, e.g., Michel and Ahuja [70]). Below a certain polar angle, however, the spectrum shape changes: at low to mid frequencies the spectrum continues to be amplified as θ is reduced, but at higher frequencies the spectrum is significantly attenuated.

The reduction at high frequency is caused by sound refraction due to the sheared mean flow. The effect of refraction gives rise to a cone of silence at lower polar angles: a region in the farfield where sound waves are almost completely attenuated. (See Spalart, Shur and Strelets [71] for a visualization of this effect with large eddy simulation and ray tracing; or Tam and Auriault [30] and Stone, Self and Howls [72] for solutions of propagation into the cone of silence.) As effects of flow-acoustic interaction are ignored, the directivity is analysed only for frequencies in which the spectrum shape does not change with polar angle. To use the entire range of available experimental data ($30^\circ < \theta < 90^\circ$) the frequency is limited at $St < 1$, for which all available polar angles are outside the cone of silence and the effect of flow–acoustic interaction is secondary to the directivity [36].

Directivity factors of the momentum and enthalpy sources are defined as the ratio between the contribution of each source to the farfield at θ and the contribution to $\theta = 90^\circ$:

$$D^m(\mathbf{x};\theta;\omega) = \frac{\delta S^m_{pp}(\mathbf{x};r;\theta;\omega)}{\delta S^m_{pp}(\mathbf{x};r;90^\circ;\omega)}, \tag{8.1}$$

and

$$D^h(\mathbf{x};\theta;\omega) = \frac{\delta S^h_{pp}(\mathbf{x};r;\theta;\omega;)}{\delta S^h_{pp}(\mathbf{x};r;90^\circ;\omega)}. \tag{8.2}$$

The contribution from an elementary volume of turbulence are introduced as δS^m_{pp} and δS^h_{pp}. They are computed by taking the formulations for S^m_{pp} and S^h_{pp} without performing the integral over the jet plume.

With the limitation that $0.1 < St < 1$, the dependence with frequency can be ignored because at this range of frequency the autospectral density and length scale spectrum are approximately independent of frequency. By also assuming axisymmetry turbulence—i.e. $\overline{u_2^2} = \overline{u_3^2}$, $\overline{u_2 u_3} = 0$, $\overline{(u_2^2)^2} = \overline{(u_3^2)^2}$, and $\overline{u_2^2 u_3^2} = 0$—the contribution to $\theta = 90^\circ$ can be related to the radial velocity component.

Using the formulation based on the cross-spectral density was used for S^m_{pp} and S^h_{pp} (Eqs. (5.33) and (5.34), the directivity factors may be written as:

$$D^m(\mathbf{x},\theta) = \frac{S_{rrrr}(\mathbf{x})V_{rrrr}(\mathbf{x})N_{rrrr}(\mathbf{x})}{S_{2222}(\mathbf{x})V_{2222}(\mathbf{x})N_{2222}(\mathbf{x})}, \tag{8.3}$$

and

$$D^h(\mathbf{x},\theta) = \frac{S_{rr}(\mathbf{x})V_{rr}(\mathbf{x})N_{rr}(\mathbf{x})}{S_{22}(\mathbf{x})V_{22}(\mathbf{x})N_{22}(\mathbf{x})}, \tag{8.4}$$

The dependence of the directivity with θ is due to the component r of velocity, which may be written (after assumption of axisymmetry), as

$$u_r(\mathbf{x},t) = u_1(\mathbf{x},t)\cos\theta + u_2(\mathbf{x},t)\sin\theta. \tag{8.5}$$

It can be shown that the directivity of the non-compactness factor is secondary [36], so the analysis in this section considers only the anisotropy of the source autospectral density and source volume. Using the models introduced in Section 5.1.2 for the autospectral density and in Section 5.2.1 for the source volume, the directivity factors may be written in terms of the integral length scale and mean square value of velocity:

$$D^m(\mathbf{x},\theta) = \frac{\sigma_{rrrr}(\mathbf{x})L^4_{rrrr}(\mathbf{x})}{\sigma_{2222}(\mathbf{x})L^4_{2222}(\mathbf{x})}, \tag{8.6}$$

and

$$D^h(\mathbf{x},\theta) = \frac{\sigma_{rr}(\mathbf{x})L^4_{rr}(\mathbf{x})}{\sigma_{22}(\mathbf{x})L^4_{22}(\mathbf{x})}. \tag{8.7}$$

8.1.1 Comparison with farfield data

The turbulence anisotropy is computed from large eddy simulation using Eq. (8.5) for u_r. So the mean square value of u_r and u_r^2, σ_{rrrr} and σ_{rr}, are computed. The integral length scale is also computed as a function of θ using Eq. (8.5) for u_r. The directivity of the mean square value and integral length scale are computed for a few axial locations and compared to the farfield directivity of the isothermal and hot jets.

Fig. 8.1 shows that the directivity due to the anisotropy of autospectral density and source volume follows the same trend as the measured directivity for the isothermal jet. An exact match is not expected because these results are for only a few locations on the lipline. The neglect of flow–acoustic interaction effects and the assumption of axisymmetric turbulence may also explain the mismatch with the experimental directivity.

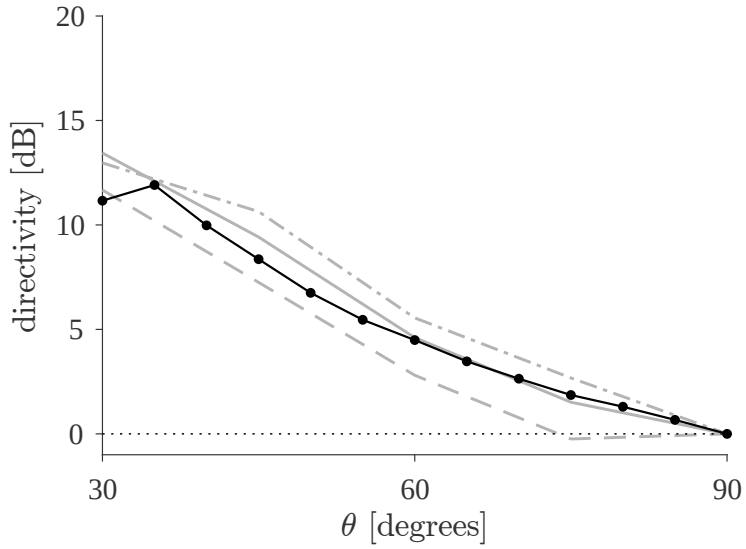

FIGURE 8.1: Directivity at mid frequency ($0.1 < St < 1$) for isothermal jet ($M = 0.88$, $T_R = 1$). Black line with symbols, measured farfield data; grey lines, predicted using turbulence anisotropy from LES data on the lipline. Dash-dot line, $x_1 = D_J$; dashed line, $x_1 = 5D_J$; continuous line, $x_1 = 9D_J$.

The results in Fig. 8.2 for the hot jet are worse. The causes of mismatch may be the same for the isothermal jet; but for the hot jet the flow–acoustic interaction becomes more significant due to sound speed gradients. Additionally, the neglect of thermodynamic fluctuations from the enthalpy source causes more error than the same simplification on the momentum term, which may add to the error due to the assumption about axisymmetry.

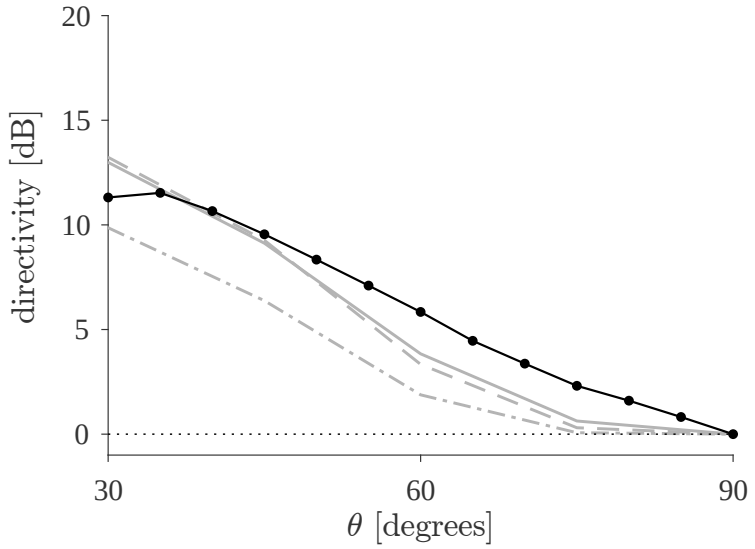

FIGURE 8.2: Directivity at mid frequency ($0.1 < St < 1$) for hot jet ($M = 0.88$, $T_R = 2.5$). Black line with symbols, measured farfield data; grey lines, predicted using turbulence anisotropy from LES data on the lipline. Continuous line, $x_1 = D_J$; dashed line, $x_1 = 3D_J$; dash-dot line, $x_1 = 6D_J$.

Despite the mismatches with the farfield directivity, this analysis shows that the effect of turbulence anisotropy is significant and must be accounted for the prediction of jet noise.

8.2 Effect of source non-compactness on farfield spectrum

The non-compactness is related to differences in retarded time and phase of turbulent fluctuations within a volume of coherent turbulence. The non-compactness factor of the momentum source was introduced in Section 5.2.1. For a farfield polar angle of $\theta = 90^\circ$ the non-compactness factor of the momentum source is

$$N_{2222}(\mathbf{x},\omega) = \left\{ 1 + \left[\frac{\omega \ell_{2222,1}(\mathbf{x},\omega)}{\overline{U}_1(\mathbf{x})} \right]^2 \right\}^{-3/2}, \tag{8.8}$$

in which $\ell_{2222,1}$ is the coherence length scale of u_2^2 with axial separation.

Figure 8.3 shows that the momentum source becomes more compact at low frequency, as expected. At high-frequency the non-compactness effect is significant but constant with frequency because the length scale spectrum decays linearly at high-frequency.

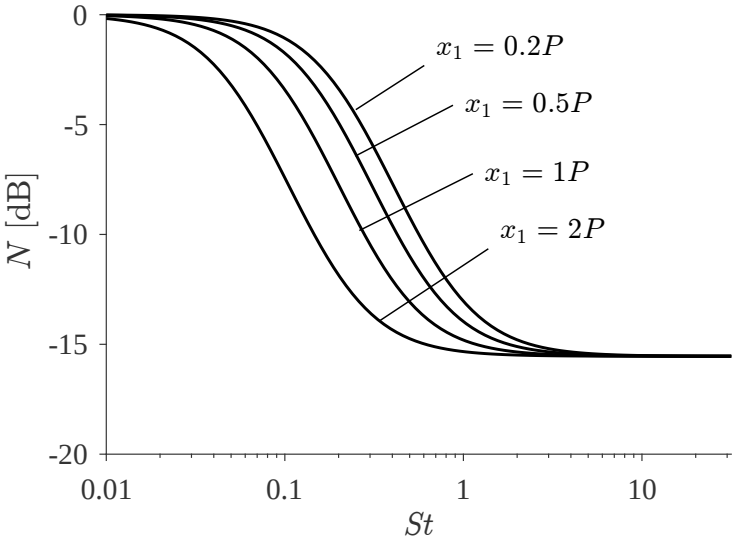

FIGURE 8.3: Effect of non-compactness factor on farfield autospectral density at $\theta = 90^\circ$ of the sound emitted from four source locations in the isothermal $M = 0.88$ jet. Four different axial locations are considered, ranging 1/5 of the potential core length ($0.2P$) to twice the potential core length ($2P$); the four locations are on the jet lipline.

The length scale spectrum of u_2^2 was computed with the model introduced in Section 5.1.3. The spectrum was not measured, but inferred from the measured data by Morris and Zaman [53] for the length scale spectrum of u_1^2. So, there is a certain inaccuracy on the levels of the non-compactness factor. The behaviour of the non-compactness factor, however, is more reliable. That is: at low frequency the non-compactness is small; at high it is frequency constant; and with a transition region at mid-frequencies.

The mid-frequency range, in which the non-compactness factor transitions from low to high frequency behaviour, coincides with the frequency range where the farfield autospectral density is relatively flat. It could be argued, therefore, that the source non-compactness is a significant factor defining the farfield behaviour in this frequency range.

Chapter 9

Conclusion

This thesis contributes to a reduction in the empiricism of RANS-based prediction of jet noise. The kind of RANS-based scheme considered in the thesis uses an empirical model of two-point turbulence statistics to compute the sound sources described by an acoustic analogy. A no-flow acoustic analogy derived from the equations of continuity, momentum, and energy was applied to model the sources of jet noise. The thesis extended a method that uses a time-domain model for turbulence statistics, and described a formulation that uses a frequency-domain model of turbulence statistics.

The thesis presented a scaling law for the farfield mean square pressure, a method to predict the farfield spectrum, an analysis of turbulence statistics in the jet plume, and computed the effects of source non-compactness and turbulence anisotropy on the farfield spectrum. These analyses sketch an overall view of the sources of jet noise in subsonic jets that can be summarised as follows:

1. The sources of jet noise may be modelled as fluctuations of momentum and enthalpy fluxes.

2. Fluctuations of enthalpy flux becomes relevant in hot jets (or more generally in jets with density different from the ambient medium).

3. The fluctuations of momentum and enthalpy fluxes may be simplified to fluctuations of velocity.

4. The contribution from the enthalpy source to the farfield mean square pressure

scales with the sixth power of jet-exit velocity. The contribution from the momentum source scales with the eighth power of jet-exit velocity.

5. The empirical model for turbulence spectrum by von Kármán [47] may be used to model the autospectral density of velocity fluctuations in the lipline of turbulent jets.

6. A modified form of the von Kármán spectrum may be applied to model the length scale spectrum of the coherence function in the lipline of turbulent jets.

7. The coherence function of transverse velocity fluctuation has an exponential decay with axial separation.

8. The anisotropy of the integral length scale is the most important effect of turbulence anisotropy on jet noise directivity.

9. Source non-compactness is a major factor for the relative flatness of the farfield spectrum near peak frequency.

Some of the conclusions listed above corroborate past work, and the ones more related to the novelties of this thesis are further discussed in Section 9.1. The known limitations of the thesis are discussed in Section 9.2, and suggestions to overcome the limitations are presented. Suggestions to extend the scope of the thesis are presented in Section 9.3.

9.1 Contributions

The starting point of this thesis was the model by Ilário et al. [10]. The extensions to the model presented in the thesis reduces the empiricism of the method and can be summarised by the following four aspects:

1. Model the enthalpy source term to predict noise from hot jets.

2. Model the turbulence statistics in frequency domain.

3. Account for source non-compactness.

4. Account for turbulence anisotropy.

In the remaining paragraphs of this section these contributions are compared to the model in Ilário et al. [10] and to the literature in general.

Enthalpy source. The model for the enthalpy source removed the need of temperature-dependent calibration used by Ilário et al. [10]. The strength of the source was shown to scale with the sixth power of jet-exit velocity, agreeing with the analysis by Morfey [17]. This trend agreed with experimental data taken in the QinetiQ Noise Test Facility [62].

The statistics of the enthalpy source term was analysed via a large eddy simulation of a subsonic hot jet ($M = 0.88$, $T_R = 2.5$). It was shown that the enthalpy source term—in exact form a combination of velocity, density, and enthalpy fluctuations—may be simplified to mean enthalpy and density, and fluctuating velocity. The simplification enables the use of empirical and theoretical analyses of statistics for velocity fluctuations to model the enthalpy source. So models for the autospectral density and length scale spectrum of velocity could be used for the enthalpy source. Moreover, a standard RANS k–ε solution could be applied as it gives information about the scales of velocity. Compare with the model by Khavaran, Kenzakowski and Mielke–Fagan [26], which needs a specialized RANS solver to compute the mean square value of temperature fluctuation.

Turbulence statistics in frequency domain. Modelling the two-points turbulence statistics is an important aspect of the RANS-based models studied in this thesis. Most models in the literature compute the source statistics with empirical models of space–time correlation (e.g., those used in references [10, 26, 29, 42]). In this thesis the empirical model of cross-spectral density by Harper-Bourne [12] was analysed and extended.

Modelling turbulence statistics in frequency domain makes straightforward to consider the frequency-dependence of turbulence scales measured by Harper-Bourne [12],

Kerhérvé, Fitzpatrick and Jordan [52], and Morris and Zaman [53]. The frequency-dependence of length scales is not necessary to model the noise at intermediate frequencies (say, $0.1 < St < 1$), because at this frequency range the length scales are rather constant with frequency. But at higher frequency the length scales start to decay, so to predict the high-frequency spectrum of jet noise the frequency-dependence of the length scales is necessary.

By analysing the source statistics in frequency domain, it was possible to distinguish between the effects of the turbulence autospectral density, coherence decay, and phase. The use of the semi-empirical spectrum by von Kármán [47] to compute the turbulence autospectral density in jets was introduced. The von Kármán spectrum better fits the data than the Lorentzian or Gaussian functions that result from the Fourier transform of the usual models for the space–time correlation. Besides the improved accuracy of the fit, using the von Kármán spectrum brings modelling the sources of jet noise closer to more general models of turbulence.

Source non-compactness. The effect of source non-compactness is related to the spectrum of coherence length scales. It was shown that the source non-compactness contributes to the relative flatness of the farfield spectrum at $\theta = 90°$. The conclusion that the source non-compactness is so significant for jet noise corroborates previous work by, e.g., Michalke [73] and Michel [74, 75]. It also supplements these previous work, for they were more focused on the effect of non-compactness in the directivity, whereas in this thesis the effect on the spectrum was shown explicitly.

Turbulence anisotropy. Turbulence anisotropy was computed by writing the source term with the velocity fluctuations in the direction of the observer (as Proudman [21]). Using data from large eddy simulations, it was shown that the largest effect of anisotropy is of the integral length scale.

The effect of change in mean square value of velocity fluctuations is secondary to the length scales, notably because the length scale is taken to the third power to compute the volume of the elementary sound sources. This analysis of anisotropy may

be compared with the analysis by Khavaran [25], in which turbulence anisotropy is mostly related to the differences in transverse–axial length scales and of mean square value between transverse and the axial velocity components.

9.2 Limitations

The work of this thesis is split in two parts: extensions of a prediction method based on a time-domain model of turbulence statistics, and a formulation based on a frequency-domain model of turbulence statistics. The former was applied to predict the farfield spectrum, whereas the latter was presented as a preliminary formulation. A first suggestion is, therefore, to finish the implementation of the prediction method based on the frequency-domain model of turbulence statistics. Further suggestions are presented in the remaining paragraphs of this section.

Flow–acoustic interaction. The models in this thesis are based on a no-flow acoustic analogy that ignores effects of flow–acoustic interaction. To present a complete prediction scheme for jet noise, it is imperative to account for these effects. They are significant in isothermal and hot jet for lower polar angles, and for hot jets even at a polar angle of 90°.

The theory to compute the interaction between sound and flow is well established, but solving the resulting equations are not straightforward if necessary to couple to a model for the sources of sound. Options to solve for propagation in jet are, for instance, via high-frequency approximations and ray tracing such as by Ilário et al. [10] or Stone, Self and Howls [72]; by low- and high-frequency solutions of Lilley's equation such as by Tester and Morfey [68, 69], Morfey, Szewczyk and Tester [48], Bassetti and Morfey [76], and Bassetti [77]; or by the solution of the adjoint form of the linearised Euler equations as by Tam and Auriault [30], Raizada and Morris [36], and Karabasov et al. [42].

Some of these different approaches to compute the propagation have been compared by Raizada and Morris [36] and Tester and Morfey [69]. It was shown that

accounting for propagation effects is necessary to predict jet noise. And that for hot jets, due to changes in local sound speed and density, flow–acoustic interactions must be considered for all polar angles.

Analysis of turbulence limited to the lipline. It is usual to assume that the lipline is the most important region for sound generation because of the higher turbulence kinetic energy. After the end of the potential core, however, the region of maximum turbulent kinetic energy tends towards the centreline of the jet. So for a more complete view of turbulence relevant for jet noise generation it will be necessary to assess the radial location of maximum turbulent kinetic energy in each axial location and analyse turbulence statistics on this location.

Limited frequency range. The large eddy simulation has a limited range of resolved frequencies. The low frequency limit of $St \approx 0.1$ is related to the total simulation time, whereas the highest resolved frequency of $St \approx 2$ is due to grid resolution. This frequency range is enough to compute the anisotropy factors, length scales at mid-frequencies and the turbulence spectrum at mid-frequencies. The frequency range, however, is not enough to analyse the autospectral density and length scale spectrum at high frequency.

A large eddy simulation with higher resolved frequency would enable the spectral analysis for other velocity components. That would extend the conclusions of Harper-Bourne [12] and Morris and Zaman [53] that were limited to the axial velocity component.

Additionally, a large eddy simulation for a hot jet with wider frequency range would enable an analysis of thermodynamic variables. For instance, Lilley [18, 19] and Khavaran et al. [26] assumed that the velocity–enthalpy correlation in the enthalpy source term can be split in a correlation of velocity and a correlation of enthalpy. In this thesis the error of this simplification was computed using large eddy simulation, but it was not possible to analyse in more detail the spectrum of the enthalpy fluctuations.

Few studies on the two-point statistics of thermodynamic fluctuations exist due to the difficulties in measuring thermodynamic fluctuations, so large eddy simulations of hot jets could greatly advance our understanding of thermodynamic fluctuation in turbulent jets.

9.3 Extensions

This section presents suggestions for work that was out of the scope of this thesis. They are related to applications of the prediction method for more realistic cases and to the empirical models of turbulence statistics.

Dual-stream nozzles. This thesis studied the turbulence and noise of single-stream circular nozzles. The engines of civil aircraft, however, consist of dual-stream nozzles, so that the findings of this thesis cannot be directly applied to predict the noise from aircraft engines.

At first, the prediction method could be applied as it is for dual-stream nozzles. That would consist of using a RANS k–ε solution of the dual-stream flow and computing the emitted noise. It is expected that new calibration of the coefficients would be necessary due to the break of self-similarity in the flow.

For a more complete analysis for dual-stream jets, it would be necessary to re-assess the structure of turbulence in the jet plume using hotwire data or large eddy simulations. A challenge in dual-stream jets is the presence of two shear layers and hence two distinct regions of high turbulent kinetic energy. The balance between these two regions will depend on the area ratio of the streams, the velocity ratio, and the temperature, all of which will add to the complexity of the analysis.

Installation effects. This thesis focused on the prediction of the farfield noise due to turbulence mixing in the jet plume. The jet was considered isolated, without any solid boundaries nearby. For the jet of aircraft engines, however, elements of the aircraft will affect the jet flow. For instance, for under-the-wing configurations the jet is affected by

the presence of the wing. The wing creates asymmetries in the jet that may modify the emitted noise. The model of this thesis could be used along an experimental campaign to check which aspects of turbulence should be assessed (e.g., Proença, Lawrence and Self [56]).

Moreover, solid surfaces near the jet add noise sources due to the interaction with the jet near-field (see, e.g., Lawrence [78]). Part of this thesis was focused on an analysis of turbulence statistics, independent of the noise source model. This analysis could also be applied to relate the fluctuations in the jet near-field to the turbulent fluctuations in the jet plume.

Length scale spectrum. Amiet [54] modelled the spectrum of length scale from the von Kármán spectrum of turbulence. Instead of an ad hoc modification of the spectrum function used in this thesis, Amiet related the autospectral density and the length scale spectrum theoretically. It is suggested that this is also assessed to model the length scale spectrum in jets.

Model for wavenumber–frequency spectrum. Modelling the cross-spectral density instead of the space–time correlation improved the modelling of turbulence statistics and enabled an easiser understanding of the process of sound generation. However, the wavenumber–frequency spectrum of turbulence is more specifically the link between turbulence and the farfield noise.

Modelling the wavenumber–frequency spectrum in non-homogeneous turbulence is not straightforward because of difficulties to measure it. But with the current computational infrastructure, computing the wavenumber–frequency spectrum in jets is viable. For instance, Sinayoko [79] used direct numerical simulation to analyse the sources of sound in transitional jets. It is suggested that his work is extended by using a large eddy simulation of a jet with higher Reynolds number (ideally, $> 10^5$) and that an empirical model for the wavenumber–frequency spectrum be developed.

Appendix A

Assessment of large eddy simulation

The large eddy simulation for two jets were available for analysis in this thesis. Both jets use the same nozzle geometry as the one used by the QINETIQ2009 test campaign. The jets have the same jet-exit velocity of 297.7m/s (acoustic Mach number of 088), but differ in temperature. One of the jets is isothermal, and the other is hot with a temperature ratio of 2.5. Table A.1 presents the operating conditions and information about the grid.

TABLE A.1: Operating conditions.

	U_J	U_J/a_J	U_J/a_0	T_R	Re_J	D_J	Grid size
Isothermal	297.7	0.88	0.88	1	2×10^5	0.1016	47M
Hot	297.7	0.55	0.88	2.7	4×10^5	0.1016	34M

In this appendix the available data is assessed in three aspects: (1) accuracy of results for mean quantities and variances by comparison with experimental data by Bridges and Wernet [58], (2) resolution in frequency and statistical relevance of the time series, (3) axisymmetry of the results, and (4) physical models of the solution. More details about the simulation and further analysis of aeroacoustics results have been presented by Naqavi et al. [14].

A.1 Physical models

For the solution a mean flow profile is imposed on the internal boundary of the nozzle—the boundary layer is laminar. Therefore, the development of turbulence takes place entirely in the shear layer. The Reynolds number being high, this does not impose a huge limitation on the development of the jet as a whole. But care must be taken on the analysis of the results for small axial coordinates (the results for $x_1 < 2D_J$, notably).

The boundary layer inside the nozzle is not resolved, but modelled by a mean flow profile. That puts in question the development of turbulence in the initial region of the shear layer, where the flow is in a non-physical state: it is the initial shear layer of a high-Reynolds number jet, but it is related to a mean boundary layer profile. The direct prediction of the acoustic farfield [14] shows that this effect is not much significant for the prediction near the peak, but it is shown to be significant for the analysis of the turbulence structure in the first few diameters of the jet (say, first two diameters).

The simulation does not use a subgrid model, relying only on numerical dissipation. So the solution for the higher wavenumbers (and higher frequency) of turbulence should be ignored.

A.2 Available data points

The data is available in blocks of 61 data points. They are so distributed in order to compute two-point statistics with separation in the axial, radial, and azimuthal directions. For each block, there are 10 points with axial separation, 40 with radial, and 10 with azimuthal spacing—half of the points are with positive spacing, half with negative. Figure A.1 depicts a block of points with centre point at $\mathbf{x} = \{3D_J, 0.5D_J, 0\}$.

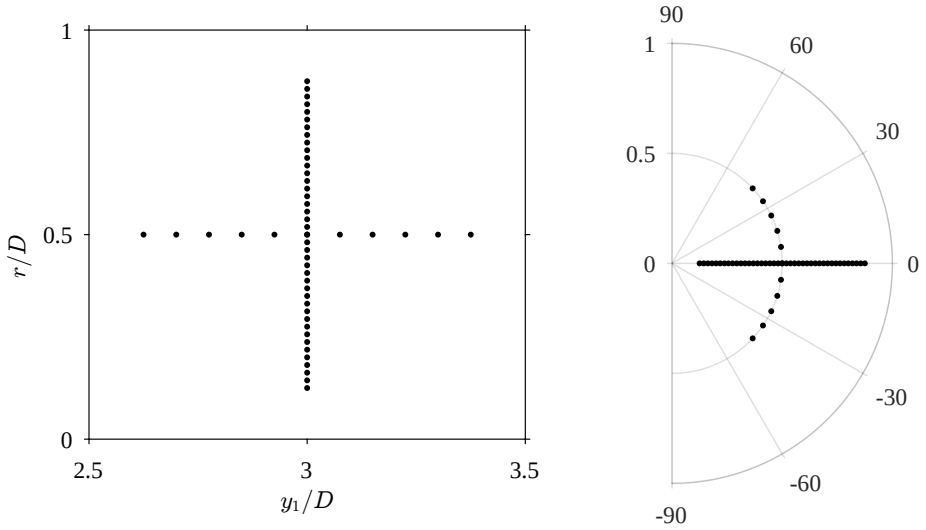

FIGURE A.1: Block of points used for computation of two-point statistics. For each block, 61 points are available: a centre-point, 10 points with different axial separations, 10 points with different azimuthal separations, and 40 points with different radial separations.

The blocks are available on the centreline and lipline of the jet. On the lipline, blocks are available with centre points in 16 different azimuthal locations (equally spaced in azimuthal angle). Table A.2 shows the axial location of the block centre point for the isothermal and hot jets. The em-dashes in Table A.2 denote locations for which no data is available. For the hot jets, data is available for shorter axial locations to follow the shortening of the potential core length. On the centreline, no data is available close to the nozzle exit.

TABLE A.2: Axial coordinate scaled by nozzle diameter of block centre points.

isothermal jet										
centreline	—	—	2	3	4	5	6	7	8	9
lipline	0.5	1	2	3	4	5	6	7	8	9
hot jet										
centreline	—	—	2	3	4	5	6	—	—	—
lipline	0.5	1	2	3	4	5	6	—	—	—

A.3 Axial profiles on the lipline

Profiles of mean axial velocity and variance of velocity fluctuations on the lipline are plotted in Figs. A.2 and A.3. The axial coordinate is normalised the potential core length (P) of each case (see Table 6.1 for the potential core length of the cases). The hot jet has a lower mean axial velocity, but higher variance value of axial velocity. That is a result of additional kinetic energy being drawn from temperature gradients, instead of just from mean flow gradient as in the isothermal jet.

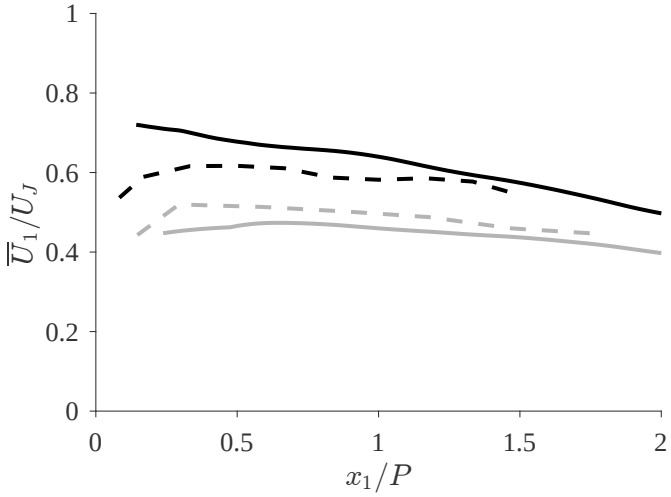

FIGURE A.2: Axial profile of mean axial velocity on the lipline. Continuous lines, data from Bridges and Wernet [58] (their setpoints 7 and 46); dashed lines, LES data. Black lines, isothermal jets; grey lines, hot jets ($T_R \approx 2.5$). All results for $M \approx 0.9$.

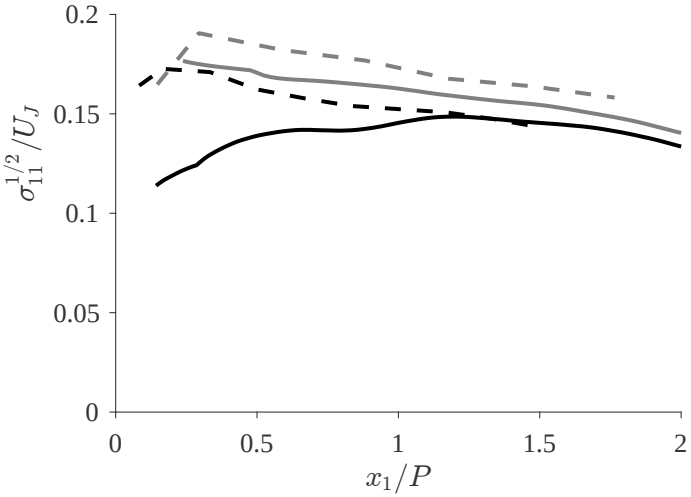

FIGURE A.3: Axial profile of variance axial velocity on the lipline. Continuous lines, data from Bridges and Wernet [58] (their setpoints 7 and 46); dashed lines, LES data. Black lines, isothermal jets; grey lines, hot jets ($T_R \approx 2.5$). All results for $M \approx 0.9$.

Radial profiles at the end of the potential core. The results for the isothermal jet are taken at $x_1 = 6D_J$, and for the hot jet at $x_1 = 3D_J$; therefore both approximately at the end of the potential core for each jet. Analogously, the results from Bridges and Wernet [58] are taken at $x_1 = 7D_J$ for the isothermal jet and at $x_1 = 4D_J$ for the hot jet.

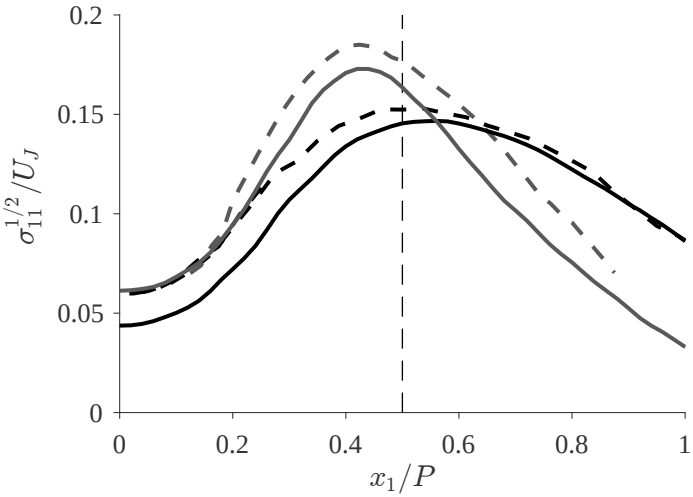

FIGURE A.4: Radial profile of variance of axial velocity at the end of the potential core. Continuous lines, data from Bridges and Wernet [58] (their setpoints 7 and 46); dashed lines, LES data. Black lines, isothermal jets; grey lines, hot jets ($T_R \approx 2.5$). All results for $M \approx 0.9$.. Vertical dashed line denotes lipline.

A.4 Axisymmetry

Both large eddy simulation are for the same axisymmetric nozzle. Yet, Figs. A.5–A.11 show that there is a significant departure from axisymmetric in the results. The thick lines in these figure indicates the azimuthal average of the results. The same azimuthal averaging was performed for all the analysis in this thesis. For instance, the autospectral density was the azimuthal average of the autospectral density in the 16 different azimuthal stations. The departure from axisymmetry in the results can be due to a short simulation time. So that the simulation did not fully achieved a stationary state.

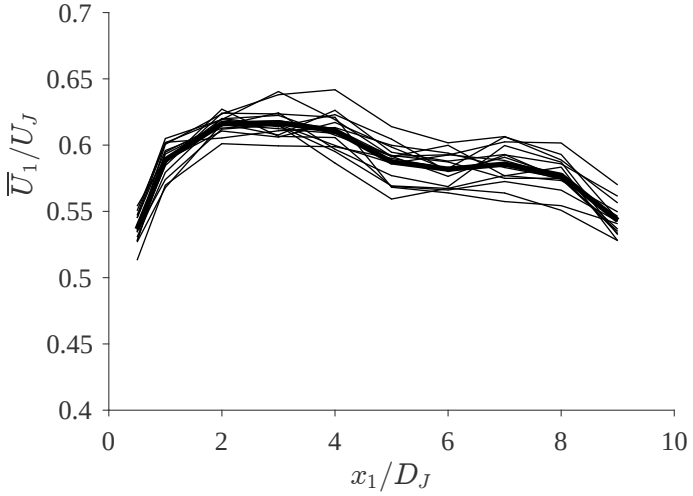

FIGURE A.5: Mean axial velocity for the isothermal jet ($M = 0.88$, $T_R = 1$). Thin lines, computed values for each azimuthal location; thick line, average at each axial location.

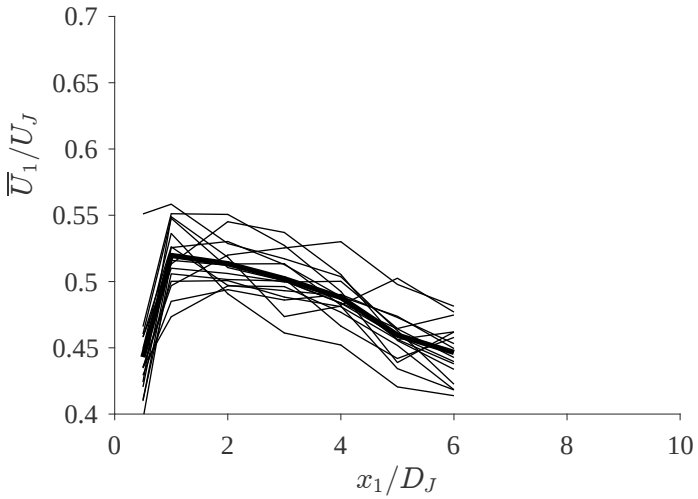

FIGURE A.6: Mean axial velocity for the hot jet ($M = 0.88$, $T_R = 2.5$). Thin lines, computed values for each azimuthal location; thick line, average at each axial location.

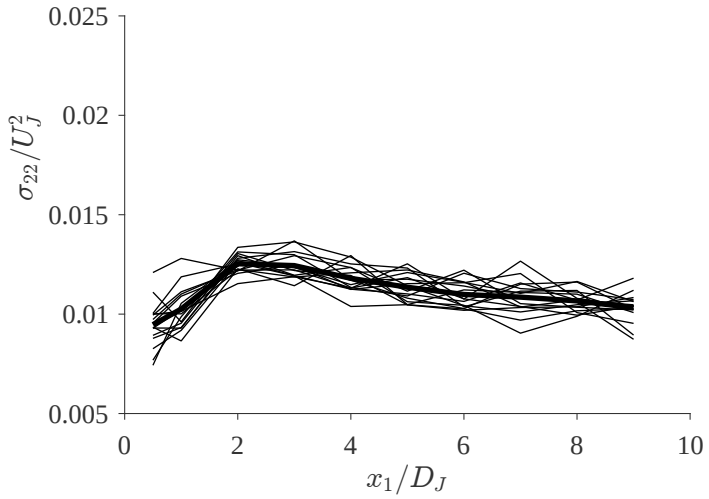

FIGURE A.7: Variance of radial velocity fluctuation in the isothermal jet ($M = 0.88$, $T_R = 1$). Thin lines, computed values for each azimuthal location; thick line, average at each axial location.

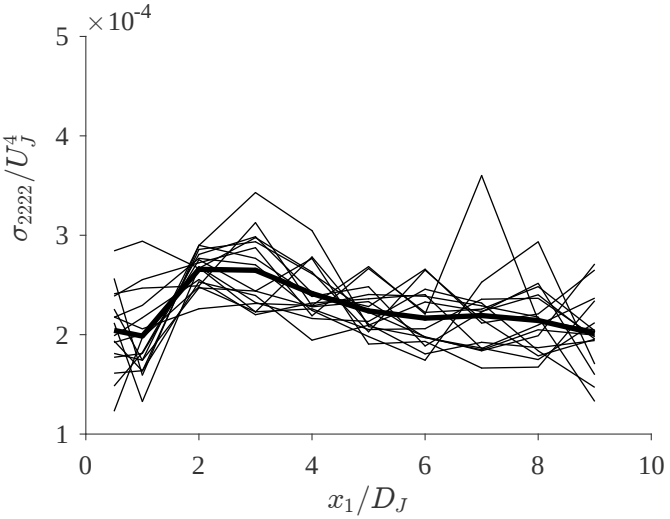

FIGURE A.8: Variance of squared radial velocity fluctuation in the isothermal jet ($M = 0.88$, $T_R = 1$). Thin lines, computed values for each azimuthal location; thick line, average at each axial location.

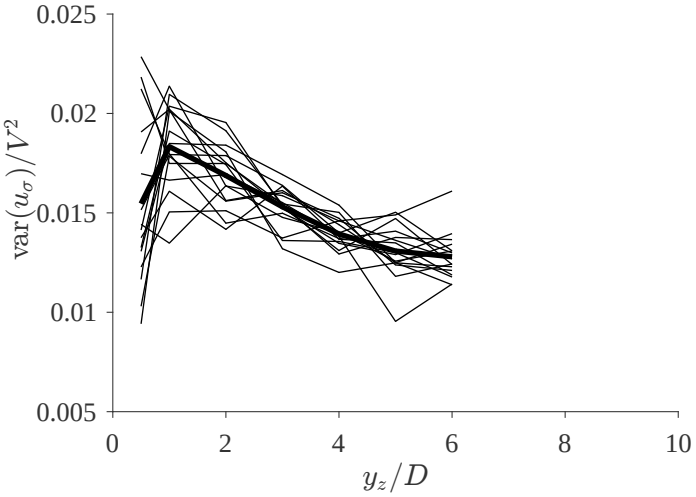

FIGURE A.9: Variance of radial velocity fluctuation in the hot jet ($M = 0.88$, $T_R = 2.5$). Thin lines, computed values for each azimuthal location; thick line, average at each axial location.

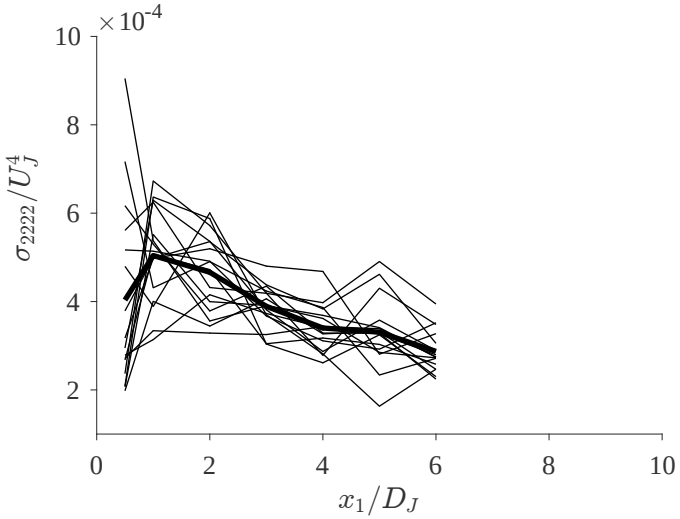

FIGURE A.10: Variance of squared radial velocity fluctuation in the hot jet ($M = 0.88$, $T_R = 2.5$). Thin lines, computed values for each azimuthal location; thick line, average at each axial location.

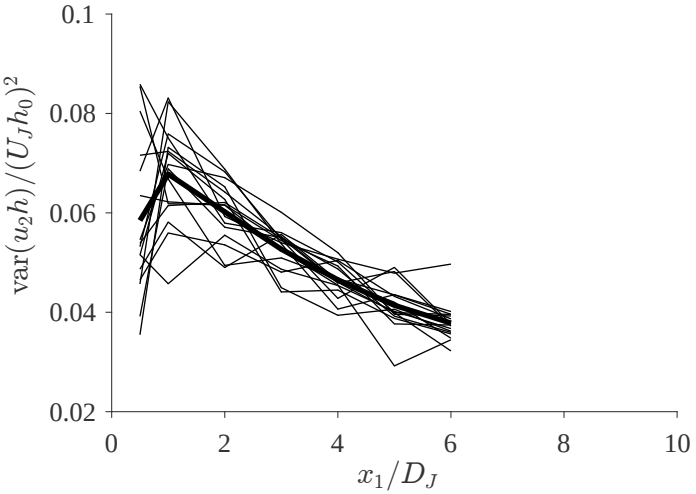

FIGURE A.11: Variance of radial velocity fluctuation multiplied by enthalpy in the hot jet ($M = 0.88$, $T_R = 2.5$). Thin lines, computed values for each azimuthal location; thick line, average at each axial location.

A.5 Frequency resolution

The frequency resolution ($\mathrm{d}f$) is related to the size of the time step ($\mathrm{d}t$) and total number of data points (N) via $\mathrm{d}f = 1/(N\mathrm{d}t)$. The time step of the available data is $\mathrm{d}t = 0.014 D_J/U_J$ for both jets; and the number of points in the time series is $N =$

8400 for the isothermal jet and $N = 8700$ for the hot jet. The frequency resolution is $\mathrm{d}f \approx 0.008 U_J/D_J$.

The minimum resolved frequency is zero; and the first non-zero value is approximately $0.008 D_J/U_J$. The maximum resolvable frequency is $f_{\max} = (1/\mathrm{d}t)/2$, which leads to a maximum resolved Strouhal number of approximately 36. The first non-zero resolvable Strouhal number is lower than necessary for the analysis of sound from turbulent jets, but it does not follow that the result is of enough statistical significance at this low frequency range. The statistical significant is related to the running time of the simulation. To improve that aspect, the signal is analysed in windows of 512 points, which gives a minimum frequency for each window of $\approx 0.14 D_J/U_J$. This Strouhal number is small enough for the analysis in this thesis, and performing the windowing improves the statistical significance at this low-frequency range [80].

The maximum resolved Strouhal of 36 is also misleading. This result is computed from the Fourier-transform of the time series, but it does not follow that the result at such high frequency is physical. The major limitation is due to the grid resolution and numerical dissipation in the modelling. It is observed in the statistical analysis of the thesis that the maximum physical Strouhal number is ≈ 2. These ranges agree with the analysis by Naqavi et al. [14].

The Fourier transforms to compute the autospectral density or the cross-spectral density are taken with Welch's method as implemented in MATLAB. A Hanning windowing and a overlap of 50% are applied to the 512-points windows. The commands to compute the autospectral density of signal `a` or the cross-spectral density and coherence between signals `a` and `b` are shown in Table A.3; `dt` is the size of the time step. Both `a` and `b` are vectors with the 8700 points for the isothermal jet and 8400 points for the hot jet.

TABLE A.3: MATLAB commands for spectral analysis.

Autospectral density	`pwelch(a,hann(512),512/2,512,1/dt)`
Cross-spectral density	`cpsd(a,b,hann(512),512/2,512,1/dt)`
Coherence	`sqrt(mscohere(a,b,hann(512),512/2,512,1/dt))`

A.6 Conclusions

The data has limitations and precludes definite conclusions about the turbulence structure and the radiated sound in high Reynolds number jets. Nevertheless, the data provided a starting point to set up a framework of analysis of turbulence. Further analysis with higher quality data can be used in the future to reassess the properties analysed in this thesis.

Though the acoustic farfield prediction is valid for the range $0.1 < St < 2$, the range of confidence for spectral analysis in the jet plume seems more limited. It varies with location, so it is not certain the quality of the spectral analysis in the jet plume. Therefore, the shape of the autospectral density and of the "spectrum" of length scales are based on hot-wire measurements [12, 53, 56]. The LES is hence used only to get the overall levels of these quantities, which is related to the most energetic range of frequencies, say $0.2 < St < 1$. Important here, and not available from hot-wire, is the possibility to get the statistics of radial and azimuthal velocity fluctuations—this is crucial, for the theory predicts that the acoustic farfield at 90 degrees to the jet axis is related to these transverse velocity fluctuations.

The analysis of axisymmetric jet enables the use of the azimuthal average of the results, which improves statistical significance.

If more definite conclusions about the structure of turbulence and its relation with the emitted sound are to be sought, it would be necessary to use a numerical solution with a wider range of confidence in terms of frequency, and possibly with matching experimental data for the same nozzle and operating conditions. Nevertheless, a consideration of these limitations of the LES data motivated the use of information inferred from hot-wire measurements, so that a prediction of the acoustic farfield could be presented.

The large eddy simulation resolves well the frequencies in the range of the most energetic scales for sound emission. It stops short (at $St \approx 2$) to be able to compute the frequency-dependence of the coherence length scales and the decay of the autospectral density at high frequency. Therefore, the large eddy simulation data data is used with

more confidence to compute the mean square value of properties, which gives the level of the autospectral density at low frequency and the length scale at low frequency (low frequency here is the region where the spectrum is flat). In terms of length scales, very important here is the possibility to compute the ratio between the statistics for the axial velocity component and for the transverse velocity components.

Appendix B

RANS k–ε data

A description of the RANS data used in this thesis is presented in this appendix. The simulations were previously used by Ilário [40] and made available for this thesis.

The RANS solution was computed used the standard RANS k–ε from ANSYS Fluent. A 2D axisymmetric grid with 60×10^3 cells was used. Compressibility was considered via a equation of state for a real gas and the energy equation was solved for the hot jets. The same nozzle of the LES solution and acoustic measurements of QinetiQ2009 data was considered (a circular $D = 0.1016$m nozzle).

Remarks:

1. The RANS solution of the hot jet overpredicts the length of the potential core.
2. RANS captures well the mean velocity on the lipline.
3. RANS underpredicts the increase in k levels on the hot jet.

B.1 Grid details

The numerical grid is bi-dimensional and axisymmetric. It consists of 59849 cells. ANSYS Fluent is used as a solver. Compressibility effects are accounted by equation of state for a real gas, and the energy equation was solved for the hot jets.

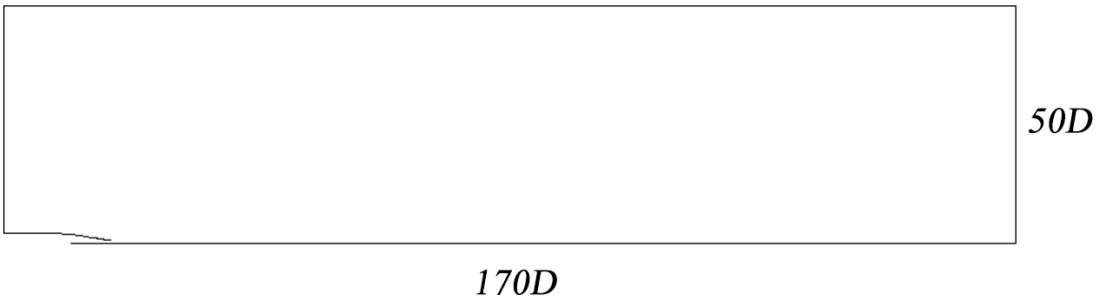

FIGURE B.1: Domain size for RANS grid.

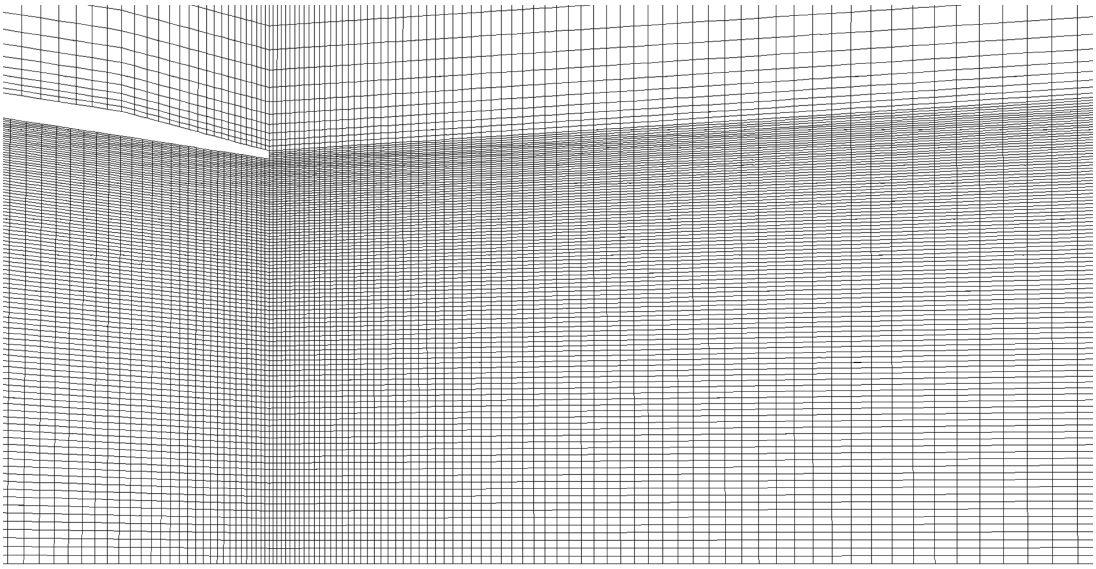

FIGURE B.2: Detail of the grid near nozzle lip.

B.2 Comparison with LES

The RANS solution is compared with the large eddy simulation by comparing mean values on the centreline and lipline. Figures B.3 and B.3 show results for the mean axial velocity on the centreline and on the lipline, respectively. Levels of turbulent kinetic energy are shown in Figs. B.5 and B.6 on the centreline and lipline, respectively.

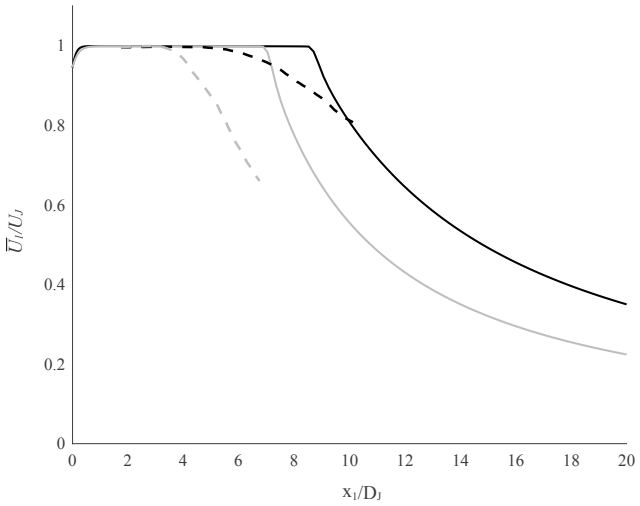

FIGURE B.3: Mean axial velocity on centreline. Black lines, isothermal jet ($M = 0.88$, $T_R = 1$); grey lines, hot jet ($M = 0.88$, $T_R = 2.5$). Continuous lines, RANS; dashed lines, LES.

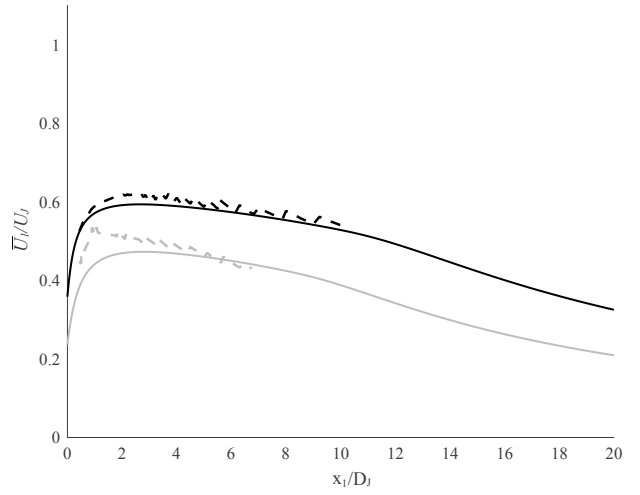

FIGURE B.4: Mean axial velocity on lipline. Black lines, isothermal jet ($M = 0.88$, $T_R = 1$); grey lines, hot jet ($M = 0.88$, $T_R = 2.5$). Continuous lines, RANS; dashed lines, LES.

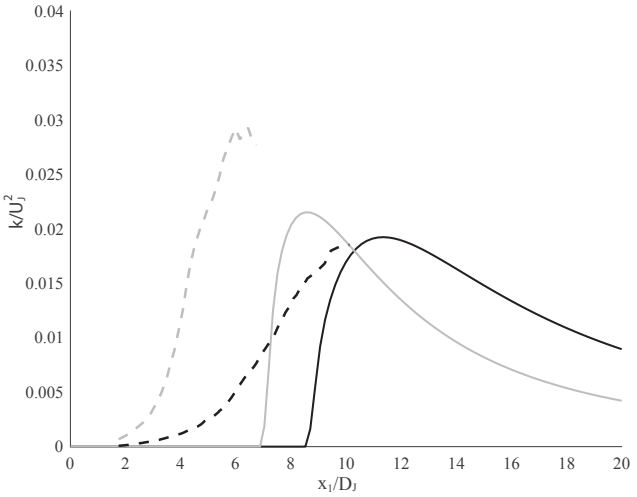

FIGURE B.5: Turbulent kinetic energy on centreline. Black lines, isothermal jet ($M = 0.88$, $T_R = 1$); grey lines, hot jet ($M = 0.88$, $T_R = 2.5$). Continuous lines, RANS; dashed lines, LES.

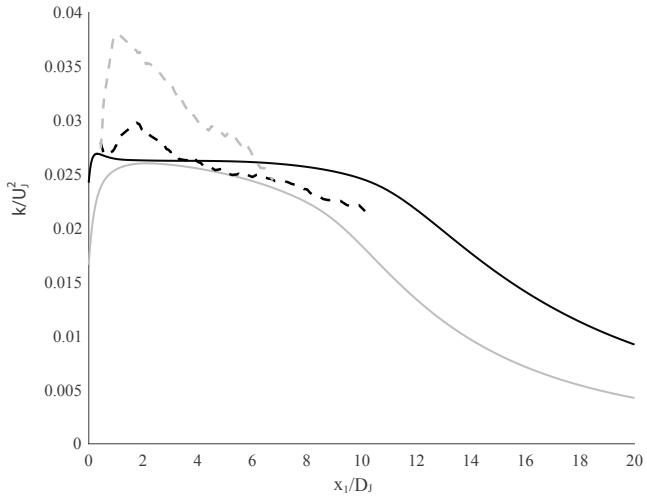

FIGURE B.6: Turbulent kinetic energy on lipline. Black lines, isothermal jet ($M = 0.88$, $T_R = 1$); grey lines, hot jet ($M = 0.88$, $T_R = 2.5$). Continuous lines, RANS; dashed lines, LES.

B.3 Problem for solution of isothermal jet

To compute an isothermal jet it is necessary to set a temperature at the inlet boundary condition higher than the external ambient temperature (T_0). Near the centre of the nozzle the air expands because of acceleration and the temperature drops to match

the desired external ambient temperature—hence an isothermal jet. However, in the boundary layer inside the nozzle there is no acceleration, and the temperature of the fluid stays the same as in the inlet condition (the wall is considered adiabatic). Thus the fluid leaves the nozzle at a slightly higher temperature than the ambient air near the nozzle wall.

B.4 Operating conditions – isentropic relations for compressible nozzle flows

Consider p_r and T_r the reservoir pressure and temperature used as boundary conditions in the simulation. Then the isentropic relations for a constant ratio of specific heats, are

$$\frac{p_r}{p_J} = \left(1 + \frac{\kappa - 1}{2} M_J^2\right)^{\kappa/(\kappa-1)}, \tag{B.1}$$

$$\frac{T_R}{T_J} = 1 + \frac{\kappa - 1}{2} M_J^2, \tag{B.2}$$

in which $M_J = U_J/a_J$ is the aerodynamic Mach number, and κ is the ratio of specific heats.

The operating conditions are usually written in terms of acoustic Mach number, M, and temperature ratio $T_R = T_J/T_0$. The nozzle-exit Mach number can be written as

$$M_J = M T_R^{-1/2}.$$

Then the isentropic relations are use to write the reservoir pressure and temperature in terms of acoustic Mach number and temperature ratio as

$$\frac{p_r}{p_0} = \left(1 + \frac{\kappa - 1}{2} M^2 T_R^{-1}\right)^{\kappa/(\kappa-1)}, \tag{B.3}$$

$$\frac{T_R}{T_0} = \left(1 + \frac{\kappa - 1}{2} M^2 T_R^{-1}\right) T_R, \tag{B.4}$$

in which p_0 and T_0 are the ambient pressure and temperature.

Bibliography

[1] M. J. T. Smith. *Aircraft Noise*. Cambridge University Press, Cambridge, 1989.

[2] R. J. Astley, A. Agarwal, K. R. Holland, P. F. Joseph, R. H. Self, M. G. Smith, R. Sugimoto, and B. J. Tester. Predicting and reducing aircraft noise. In *14th International Congress on Sound and Vibration*, Cairn, Australia, 9–12 July 2007.

[3] ICAO. On board – a sustainable future. ICAO environmental report. Technical report, ICAO, 2016.

[4] J. B. Freund. Noise sources in a low-Reynolds-number turbulent jet at Mach 0.9. *J. Fluid Mech.*, 438:277–305, 2001.

[5] Z.-N. Wang, I. Naqavi, and P. G. Tucker. Large-eddy simulation of the flight stream effects on single stream heated jets. In *55th AIAA Aerospace Sciences Meeting*, Grapevine, Texas, 9–13 January 2017.

[6] J. C. Tyacke, Z.-N. Wang, and P. G. Tucker. LES-RANS of installed ultra-high bypass-ratio coaxial jet aeroacoustics with a finite span wing-flap geometry and flight stream — part 1: round nozzle. In *23rd AIAA/CEAS Aeroacoustics Conference*, Denver, Colorado, 5–9 June 2017.

[7] M. J. Lighthill. On sound generated aerodynamically. I. General theory. *Proc. R. Soc. A*, 211(1107):564–587, 1952.

[8] A. Khavaran, E. A. Krejsa, and C. M. Kim. Computation of supersonic jet mixing noise for an axisymmetric convergent-divergent nozzle. *J. Aircr.*, 31(3):603–609, 1994.

[9] G. M. Lilley. The generation and radiation of supersonic jet noise. IV. Theory of turbulence generated jet noise, noise radiation from upstream sources and

combustion noise. Technical Report TR-72-53, United States Air Force Aero Propulsion Laboratory, 1972.

[10] C. R. S. Ilário, M. Azarpeyvand, V. Rosa, R. Self, and J. R. Meneghini. Prediction of jet mixing noise with Lighthill's acoustic analogy and geometrical acoustics. *J. Acoust. Soc. Am.*, 141(2):1203–1213, 2017.

[11] R. H. Self. Jet noise prediction using the Lighthill acoustic analogy. *J. Sound Vib.*, 275(3–5):757–768, 2004.

[12] M. Harper-Bourne. Jet near-field noise prediction. In *5th AIAA/CEAS Aeroacoustics Conference and Exhibit*, Bellevue, Washington, 10–12 May 1999.

[13] R. H. Self and M. Azarpeyvand. Utilization of turbulent energy transfer rate time-scale in aeroacoustics with application to heated jets. *Int. J. Aeroacoust.*, 7(2):83–102, 2008.

[14] I. Z. Naqavi, Z.-N. Wang, P. G. Tucker, M. Mahak, and P. Strange. Far-field noise prediction for jets using large-eddy simulation and Ffowcs Williams–Hawkings method. *Int. J. Aeroacoust.*, 2016.

[15] C. R. S. Ilário. *Development of a novel RANS-based method for the computational aeroacoustics of high speed jets*. PhD thesis, Universidade de São Paulo, São Paulo, 2011.

[16] M. E. Goldstein. An exact form of Lilley's equation with a velocity quadrupole/temperature dipole source term. *J. Fluid Mech.*, 443:231–236, 2001.

[17] C. L. Morfey. Amplification of aerodynamic noise by convected flow inhomogeneities. *J. Sound Vib.*, 31(4):391–397, 1973.

[18] G. M. Lilley. On the noise from jets. Technical Report 131, AGARD-CP, 1974.

[19] G. M. Lilley. The radiated noise from isotropic turbulence with applications to the theory of jet noise. *J. Sound Vib.*, 190(3):463–476, 1996.

[20] M. S. Howe. *Theory of vortex sound*. Cambridge University Press, Cambridge, 2003.

[21] I. Proudman. The generation of noise by isotropic turbulence. *Proc. R. Soc. A*, 214(1116):119–132, 1952.

[22] S. Sarkar and M. Y. Hussaini. Computation of the sound generated by isotropic turbulence. Technical Report Report 93-74, ICASE, 1993.

[23] J. E. Ffowcs Williams. The noise from turbulence convected at high speed. *Phil. Trans. Soc. A*, 255(1061):469–503, 1963.

[24] G. K. Batchelor. *The Theory of Homogeneous Turbulence*. Cambridge University Press, Cambridge, 1953.

[25] A. Khavaran. Role of anisotropy in turbulent mixing noise. *AIAA J.*, 37(7):832–841, 1999.

[26] A. Khavaran, D. C. Kenzakowski, and A. F. Mielke–Fagan. Hot jets and sources of jet noise. *Int. J. Aeroacoust.*, 9(4–5):491–532, 2010.

[27] M. E. Goldstein. A generalized acoustic analogy. *J. Fluid Mech.*, 488:315–333, 2003.

[28] J. Bridges and M. P. Wernet. Turbulence measurements of separate flow nozzles with mixing enhancement features. In *8th AIAA/CEAS Aeroacoustics Conference and Exhibit*, Breckenridge, Colorado, 17–19 June 2002.

[29] C. K. W. Tam and L. Auriault. Jet mixing noise from fine-scale turbulence. *AIAA J.*, 37(2):145–153, 1999.

[30] C. K. W. Tam and L. Auriault. Mean flow refraction effects on sound radiated from localized sources in a jet. *J. Fluid Mech.*, 370:149–174, 1998.

[31] P. O. A. L. Davies, M. J. Fisher, and M. J. Barrat. The characteristics of the turbulence in the mixing region of a round jet. *J. Fluid Mech.*, 15, 1963.

[32] C. K. W. Tam, N. N. Pastouchenko, and K. Viswanathan. Fine-scale turbulence noise from hot jets. *AIAA J.*, 43(8), 2005.

[33] M. Doty and D. K. McLaughlin. Two-point correlations of density gradient fluctuations in high speed jets using optical deflectometry. In *40th AIAA Aerospace Sciences Meeting & Exhibit*, Reno, Nevada, 14–17 January 2002.

[34] P. J. Morris and F. Farassat. Acoustic analogy and alternative theories for jet noise prediction. *AIAA J.*, 40(4):671–680, 2002.

[35] P. J. Morris and S. Boluriaan. The prediction of jet noise from CFD data. In *10th AIAA/CEAS Aeroacoustics Conference*, Manchester, UK, 10–12 May 2004.

[36] N. Raizada and P. J. Morris. Prediction of noise from high speed subsonic jets using an acoustic analogy. In *12th AIAA/CEAS Aeroacoustics Conference*, Cambridge, Massachusetts, 8–10 May 2006.

[37] R. H. Self. A RANS CFD coupled model for predicting coaxial jet noise. Technical report, Institute of Sound and Vibration Research, 2005.

[38] M. Azarpeyvand and R. Self. Improved jet noise modeling using a new timescale. *J. Acoust. Soc. Am.*, 126(3), 2009.

[39] V. Rosa, C. J. Deschamps, J. P. L. C. Salazar, and C. R. S. Ilário. Comparison of RANS-based methods for the prediction of noise emitted by subsonic turbulent jets. In *19th AIAA/CEAS Aeroacoustics Conference*, Berlin, Germany, 27–29 May 2013.

[40] C. R. S. Ilário, J. R. Meneghini, M. Azarpeyvand, and R. H. Self. A ray-tracing method applied to the propagation of jet noise. In *17th International Congress on Sound and Vibration*, Cairo, Egypt, 18–22 July 2010.

[41] M. Azarpeyvand. *Some aspects of RANS based jet noise prediction*. PhD thesis, University of Southampton, 2008.

[42] S. A. Karabasov, M. Z. Afsar, T. P. Hynes, A. P. Dowling, W. A. McMullan, C. D. Pokora, G. J. Page, and J. J. McGuirk. Jet noise: acoustic analogy informed by Large Eddy Simulation. *AIAA J.*, 48(7), 2010.

[43] C. K. W. Tam, M. Golebiowski, and J. M. Seiner. On the two components of

turbulent mixing noise from supersonic jets. In *2nd AIAA/CEAS Aeroacoustics Conference*, State College, Pennsylvania, 6–8 May 1996.

[44] P. Jordan and T. Colonius. Wave packets and turbulent jet noise. *Annu. Rev. Fluid Mech.*, 45:173–95, 2013.

[45] N. K. Depuru Mohan, A. P. Dowling, S. A. Karabasov, H. Xia, O. Graham, T. P. Hynes, and P. G. Tucker. Acoustic sources and far-field noise of chevron and round jets. *AIAA J.*, 53(9), 2015.

[46] V. A. Semiletov and S. A. Karabasov. On the properties of fluctuating turbulent stress sources for high-speed jet noise. In *22nd AIAA/CEAS Aeroacoustics Conference*, Lyon, France, 30 May – 1 June 2016.

[47] Th. von Kármán. Progress in the statistical theory of turbulence. *Proc. Natl. Acad. Sci. USA*, 34(11):530–539, 1948.

[48] C. L. Morfey, V. M. Szewczyk, and B. J. Tester. New scaling laws for hot and cold jet mixing noise on a geometric acoustics model. *J. Sound Vib.*, 61(2):255–292, 1978.

[49] D. C. Pridmore-Brown. Sound propagation in a fluid flowing through an attenuating duct. *J. Fluid Mech.*, 4(4):393–406, 1958.

[50] H. K. Tanna, P. D. Dean, and M. J. Fisher. The influence of temperature on shock-free supersonic jet noise. *J. Sound Vib.*, 39(4):429–460, 1975.

[51] H. S. Ribner. Quadrupole correlations governing the pattern of jet noise. *J. Fluid Mech.*, 38(1):1–24, 1969.

[52] F. Kerhervé, J. Fitzpatrick, and P. Jordan. The frequency dependence of jet turbulence for noise source modelling. *J. Sound Vib.*, 296, 2006.

[53] P. J. Morris and K. B. M. Q. Zaman. Velocity measurements in jets with application to noise source modeling. *J. Sound Vib.*, 329:394–414, 2010.

[54] R. K. Amiet. Acoustic radiation from an airfoil in a turbulent stream. *J. Sound Vib.*, 41(4):407–420, 1975.

[55] S. Glegg and W. Devenport. *Aeroacoustics of Low Mach Number Flows - Fundamentals, Analysis, and Measurement*. Academic Press, London, 2017.

[56] A. R. Proenca, J. L. T. Lawrence, and R. H. Self. A survey of the turbulence statistics of a model-scale installed jet at low and moderate mach numbers. In *23rd AIAA/CEAS Aeroacoustics Conference*, Denver, Colorado, 5–9 June 2017.

[57] M. Harper-Bourne. Jet noise turbulence measurements. In *9th AIAA/CEAS Aeroacoustics Conference and Exhibit*, Hilton Head, South Carolina, 12–14 May 2003.

[58] J. Bridges and M. P. Wernet. Establishing consensus turbulence statistics for hot subsonic jets. In *16th AIAA/CEAS Aeroacoustics Conference*, Stockholm, Sweden, 7–9 June 2010.

[59] D. L. Martlew, J. M. Hawkins, R. L. Brooking, and A. S. Kennedy. The design, construction and operation of the noise test facility at the national gas turbine establishment. *Aeronaut. J.*, 80(781):1–19, 1976.

[60] R. A. Pinker. Results from an experimental programme on static single-stream jet noise. Technical Report QinetiQ/FST/TN026455, QinetiQ, 2003.

[61] M. Harper-Bourne. Some observations on the noise of heated jets. In *13th AIAA/CEAS Aeroacoustics Conference*, Rome, Italy, 2007.

[62] S. Nauri. Test definition document for SYMPHONY WP3.3 source location test. Technical Report QINETIQ/CON/ACP/TPN0901575, QinetiQ, 2009.

[63] K. Viswanathan. Distributions of noise sources in heated and cold jets: Are they different? In *16th AIAA/CEAS Aeroacoustics Conference*, Stockholm, Sweden, 7–9 June 2010.

[64] A. Z. Karon and K.K. Ahuja. Reynolds number and jet noise scaling relationships. In *23rd AIAA/CEAS Aeroacoustics Conference*, Denver, Colorado, 5–9 June 2017.

[65] K. Viswanathan. Aeroacoustics of hot jets. *J. Fluid Mech.*, 516:39–82, 2004.

[66] K. K. Ahuja and K. W. Bushell. An experimental study of subsonic jet noise and comparison with theory. *J. Sound Vib.*, 30(3):317–341, 1973.

[67] M. Harper-Bourne. Jet noise measurements: past and present. *Int. J. Aeroacoust.*, 9(4 & 5):559–588, 2010.

[68] B. J. Tester and C. L. Morfey. Development in jet noise modelling—theoretical predictions and comparisons with measured data. *J. Sound Vib.*, 46(1):79–103, 1976.

[69] B. J. Tester and C. L. Morfey. Solving the Lilley equation with quadrupole and dipole sources. *Int. J. Aeroacoust.*, 9(4 & 5):419–460, 2010.

[70] U. Michel and K. K. Ahuja. On the scaling of jet noise with Helmholtz number close to the jet axis. In *20th AIAA/CEAS Aeroacoustics Conference*, Atlanta, Georgia, 16–20 June 2014.

[71] P. R. Spalart, M. L. Shur, and M. Kh. Strelets. Identification of sound sources in large-eddy simulations of jets. In *13th AIAA/CEAS Aeroacoustics Conference*, Rome, Italy, 21–23 May 2007.

[72] J. T. Stone, R. H. Self, and C. J. Howls. Aeroacoustic catastrophes: upstream cusp beaming in Lilley's equation. *Proc. R. Soc. A*, 473(2201):1–28, 2017.

[73] A. Michalke. A wave model for sound generation in circular jets. Technical Report FB 70-57, DLR, 1970.

[74] U. Michel. Influence of source interference on the directivity of jet mixing noise. In *13th AIAA/CEAS Aeroacoustics Conference*, Rome, Italy, 21–23 May 2007.

[75] U. Michel. The role of source interference in jet noise. In *15th AIAA/CEAS Aeroacoustics Conference*, Miami, Florida, 11–13 May 2009.

[76] A. Bassetti and C. L. Morfey. An acoustic-analogy model for jet-noise prediction. In *13th AIAA/CEAS Aeroacoustics Conference*, Rome, Italy, 21–23 May 2007.

[77] A. Bassetti. *A statistical jet-noise model based on the acoustic analogy and a*

RANS solution. PhD thesis, University of Southampton, 2009.

[78] J. L. T. Lawrence. *Aeroacoustic interactions of installed subsonic jets*. PhD thesis, University of Southampton, 2014.

[79] S. Sinayoko. *Numerical investigation of the true sources of jet noise*. PhD thesis, University of Southampton, 2010.

[80] K. Shin and J. K. Hammond. *Fundamentals of signal processing for sound and vibration engineers*. Wiley, Chichester, 2008.